



NON-SPECULAR RADAR CROSS SECTION STUDY

Eugene F. Knott, Valdis V. Liepa and Thomas B. A. Senior

The University of Michigan
College of Engineering
Department of Electrical and Computer Engineering
The Radiation Laboratory
Ann Arbor, Michigan

TECHNICAL REPORT AFAL-TR-73-70

April 1973

Distribution limited to U. S. Government Agencies only;
Test and Evaluation Data; April 1973.
Other requests for this document must be referred to
AFAL/WRP.

11062-1-F = RL-2203

**Air Force Avionics Laboratory
Air Force Systems Command
Wright-Patterson Air Force Base, Ohio**

NON-SPECULAR RADAR CROSS SECTION STUDY

**Eugene F. Knott
Valdis V. Liepa
Thomas B. A. Senior**

**Distribution limited to U. S. Government Agencies only;
Test and Evaluation Data; April 1973.
Other requests for this document must be referred to
AFAL/WRP.**

NOTICE

When Government drawings, specifications, or other data are used for any purpose other than in connection with a definitely related Government procurement operation, the United States Government thereby incurs no responsibility nor any obligation whatsoever; and the fact that the government may have formulated, furnished, or in any way supplied the said drawings, specifications, or other data, is not to be regarded by implication or otherwise as in any manner licensing the holder or any other person or corporation, or conveying any rights or permission to manufacture, use, or sell any patented invention that may in any way be related thereto.

Copies of this report should not be returned unless return is required by security considerations, contractual obligations, or notice on a specific document.

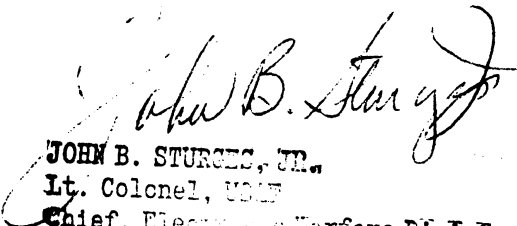
FOREWORD

This Final Report describes research performed by The University of Michigan Radiation Laboratory, 2455 Hayward, Ann Arbor, Michigan 48105, under USAF Contract F33615-72-C-1439, Project 7633, "Non-Specular Radar Cross Section Study". The research was sponsored by the Electromagnetic Division, Air Force Avionics Laboratory and the technical Monitor was Dr. Charles H. Krueger, AFAL/WRP.

This report covers the time period 15 April 1972 through 16 January 1973 and was prepared by Eugene F. Knott, Valdis V. Liepa and Thomas B. A. Senior; Mr. Knott and Professor Senior shared the duties of Principal Investigator. The authors gratefully acknowledge the participation of Mr. Gerard A. Desjardins in the preparation of computer programs necessary in the research. The report has been assigned Radiation Laboratory Report Number 011062-1-F for internal control purposes. It was submitted for sponsor approval on 12 February 1973.

23 MAR 1973

This Technical Report has been reviewed and is approved for publication.



JOHN B. STURGES, JR.
Lt. Colonel, USAF
Chief, Electronic Warfare Division

ABSTRACT

The research described in this document is directed toward the reduction of non-specular radar cross sections and the optimization of specific surface impedance treatments for shapes characterized by such scattering. The optimization is carried out by means of a computer program which digitally solves the surface field integral equations for an impedance boundary condition. The original program was furnished by the Air Force Avionics Laboratory and was later modified by the Radiation Laboratory in order to meet the specific requirements of the task.

Salient results of the investigation show that maximum performance is obtained with maximum surface coverage and that performance is generally traded off for less extensive surface treatment. An impedance variation that increases linearly with increasing distance toward the rear of a body is preferable to any other, provided the rate of change at the commencement and termination of the loading is not too great. Because of the dual nature of the integral equations for E- and H-polarizations, the impedance in the vicinity of the edge itself is critical, since a favorable result for one polarization can be detrimental for the other.

Because the specification of a desirable surface impedance variation does not necessarily lead directly to the specification of material properties, other studies were carried out to provide more information. A theoretical study of a coated sphere showed that if the coating meets certain specifications, the surface impedance can be predicted by means of a simple layer formula. Actual measurements of both surface fields and far scattered fields were performed and although some variance was noted, the data tend to confirm the dual nature of the E- and H-polarized integral equations.

TABLE OF CONTENTS

	page
I INTRODUCTION	1
II THE WEDGE CYLINDER	7
2.1 Review of Previous Results	7
2.2 Other Loading Variations	10
III E-POLARIZATION	24
3.1 GTD as a Gauge	24
3.2 Early Results of RAM1B	27
3.3 Program RAMC	39
IV EXPERIMENTAL WORK	42
4.1 Experimental Models	43
4.2 Backscatter Measurements	45
4.3 Surface Field Measurements	52
V SURFACE IMPEDANCE STUDIES	65
APPENDIX A	76
APPENDIX B	89
APPENDIX C	100
REFERENCES	103

LIST OF ILLUSTRATIONS

		page
2-1	Computed surface currents for a wedge-cylinder at axial incidence.	9
2-2	Surface impedance profiles.	11
2-3	Bistatic cross section patterns for completely covered wedge-cylinder at H-polarization.	13
2-4	Bistatic cross section patterns for partially covered wedge-cylinder at H-polarization.	14
2-5	Bistatic cross section patterns for partially covered wedge-cylinder at H-polarization.	15
2-6	Bistatic cross section patterns of completely coated wedge-cylinder having square law variation over the wedge face.	16
2-7	Bistatic cross section pattern of wedge-cylinder with bare wedge faces and linear load in the rear.	18
2-8	Bistatic cross section patterns of wedge-cylinder with bare wedge faces and square law load in the rear.	19
2-9	Edge-on cross section of wedge-cylinder with constant load in the rear.	20
2-10	Values of the peak cross section in the edge-on region of a wedge-cylinder as a function of the maximum impedance.	21
2-11	Edge-on cross section of the wedge-cylinder with bare wedge faces and loading over the cylindrical surface.	23
3-1	Comparison of measured ogival cylinder patterns (—) with those predicted by first order GTD (-----).	26
3-2	Comparison of E-polarization bistatic scattering predictions for ogival cylinder.	28
3-3	The surface current distribution that produced the RAM1B scattering pattern of Fig. 3-2.	30
3-4	Four radii of curvature were used to relieve the sharp edges of the ogival cylinder. This is a plot of the upper profile near one edge.	31

LIST OF ILLUSTRATIONS (continued)

		page
3-5	Surface current distribution over blunted 25-degree ogival cylinder, edge radii of 0.04λ .	32
3-6	Peak values of front and rear edge currents as functions of the edge radius for 25-degree angle of incidence.	33
3-7	Comparison of bistatic scattering for rounded edges with that given by GTD for a sharp edge.	35
3-8	Influence of sampling rate on peak edge currents.	36
3-9	Comparison of bistatic scattered field from ogival cylinder with dense sampling at the edges.	38
4-1	Dimensions of the experimental ogival-cylinder are given in inches; the lower diagram shows a finite edge radius and the overlapping of the coating beyond the edge.	44
4-2	Backscattering from bare ogival cylinder, E-polarization.	48
4-3	Backscattering from bare ogival cylinder, H-polarization.	49
4-4	Backscattering from coated ogival cylinder, E-polarization.	50
4-5	Backscattering from coated ogival cylinder, H-polarization.	51
4-6	Block diagram of equipment and facility used for surface field measurements.	53
4-7	Measured current and phase on bare ogival cylinder, H-polarization.	56
4-8	Measured current and phase on the bare ogival cylinder, E-polarization.	58
4-9	Measured magnetic field and its phase on coated ogival cylinder, H-polarization.	59
4-10	Measured electric field and its phase on the coated ogival cylinder, H-polarization.	60

LIST OF ILLUSTRATIONS (continued)

	page
4-11 Measured magnetic field and its phase on the coated ogival cylinder, E-polarization.	62
4-12 Measured electric field and its phase on the coated ogival cylinder, E-polarization.	63
5-1 Deduced amplitude and phase of surface impedance for E-polarization. The phase is relative to an arbitrary value of ϕ'_0 .	66
5-2 Deduced amplitude and phase of surface impedance for H-polarization. The phase is relative to an arbitrary value ϕ_0 .	67
5-3 Surface impedance of a coated sphere at a function of position for two types of coatings.	70

I. INTRODUCTION

This is the final report required under USAF Contract F33615-72-C-1439 and, along with an interim report submitted earlier in the contract (Knott and Senior, 1973), it represents a summary of the total work performed and results obtained. The objectives of the contract were given in the first two paragraphs of the previous report and, for the benefit of readers who have not had access to that document, we repeat them below.

"The objective of the research reported herein is to investigate non-specular scattering and to develop techniques for suppressing it, with the expectation that absorbing materials will be the most likely means of doing so. To carry out the investigation, three simple scattering obstacles are used that embody the features of non-specular scattering to be treated. The primary tool used to accomplish the work is a digital computer program based on the integral equation solution of a two-dimensional obstacle over which a surface impedance boundary condition is imposed.

"The suppression of scattering is a camouflage problem, but over the years the development of techniques for the reduction of specular contributions has received more attention. This is in part because specular echoes tend to dominate the net return whenever they are present, and though they tend to be restricted in the aspect angles for which they occur, they are amenable to suppression using radar absorbents. In contrast, non-specular scattering is more pervasive and even if all specular echoes are suppressed, we are still faced with this other form of scattering which can generate returns of an unacceptable magnitude and do so over a wide range of aspects. Indeed, modern aerospace vehicles are seldom seen at specular aspects in a tactical environment, yet their radar cross sections can attain levels that increase the probability of detection. It is therefore important to address the problem of reducing non-specular returns."

The non-specular types of scattering of interest in this contract are edge diffraction, traveling waves and creeping waves, the first occurring primarily for E-polarization and the remainder for H-polarization. Three simple geometries were selected as test obstacles and, as we shall see later, a laboratory model of one of them was constructed for experimental work. The three shapes studied were the ogival cylinder, the wedge-cylinder and the prism, and these may be thought of as the two-dimensional counterparts of the true ogive (a spindle), the cone-sphere and the right circular cone. While three shapes had been selected, the bulk of the research has been directed toward the first two.

Although edge diffraction occurs for all three geometries, it is the leading edge that is, by far, the strongest contributor for E-polarization. Since most of our efforts have been devoted to H-polarization, however, leading edge diffraction will become one of the important considerations in any future work. Non-specular scattering due to traveling waves occurs at H-polarization and it is now the trailing edge, if any, that becomes the dominant source of scattering; the ogival cylinder and the prism are two test obstacles with which the traveling wave returns can be studied. If the body is smooth and without a trailing edge, as is the wedge-cylinder, there is no sharp discontinuity to reflect a traveling wave and the wave continues into the shadow region and becomes a creeping wave. Although the creeping wave is attenuated by the curvature of the surface, it can emerge on the opposite side of the body with sufficient strength remaining to become an important contributor to the non-specular scattering.

The only hope of suppressing these non-specular sources of scattering over a wide range of frequencies is to reduce the strength of each over the frequency range. This implies that the scatterers must act independently so that the suppression or modification of any one of them has no influence on the treatment of those that remain. Such independence is characteristic of high frequency scattering and the bodies studied in the research are, in the main, large enough to fit in the high frequency category.

A computer program named RAM1B, a modified version of one supplied us by AFAL, was the tool by which we studied ways of suppressing non-specular

scattering contributions. The program invokes an impedance boundary condition over the entire profile of a two-dimensional obstacle, thereby permitting the user to simulate the presence of absorbing materials. The impedance boundary condition itself is not dependent upon frequency so that, once an effective impedance has been established for a given class of non-specular contributor, the same impedance should work for all higher frequencies. The problem then becomes one of finding or specifying materials such that this impedance behavior can be synthesized over the frequency range of interest.

In the previous report we showed that maximum cross section reduction for the ogival cylinder at H-polarization is obtainable only by coating an appreciable portion of the rear half of the body. The optimum impedance variation seemed to be a linear one (impedance increasing linearly with increasing distance toward the trailing edge), with better performance occurring as the impedance is taken to ever higher values at the trailing edge. The benefit of the loading is lost, however, if the linear rate is too steep, and our results suggested that a sharp rise creates a new source of scattering at the point on the body where the loading is commenced.

In Chapter II of this, the final report, we discuss the effect of loading the wedge-cylinder for H-polarization. Incidence is taken to be along the longitudinal plane of symmetry and the non-specular scattering is due to three contributors: the edge diffraction, a pair of join returns and a creeping wave contribution. As with the ogival cylinder, we show that maximum cross-section reduction is obtained with maximum surface coverage and that both the creeping wave and the join contributions, the two largest contributors, must be attacked in order to achieve the desired reduction; reducing only one of them is not sufficient.

Our studies of both bodies for H-polarization show that although maximum cross section reduction of the returns from these edged structures is obtained when most of the body is covered, one must be careful not to coat the leading edge itself. The reason, as discussed in the previous report, lies in the dual nature of the E- and H-polarization integral equations under the surface impedance boundary condition. Increasing the impedance at a leading edge for H-polarization tends to increase the scattering from it, and the nominally low H-polarized return tends

to take on the characteristics of a stronger E-polarized return. And, although we do not yet have computer results to show it, increasing the impedance at a trailing edge tends to convert a nominally low E-polarized contribution into a stronger return characteristic of H-polarization.

These important conclusions are based on the data provided by RAM1B, the impedance boundary condition program, and there remains the critical task of converting the abstraction of surface impedance to the reality of physically realizable materials that can be applied to actual surfaces. In our last report we pointed out that, in the general case, the surface impedance depends not only upon the electrical properties of a coating but also upon the surface to which it is applied and the nature of the fields illuminating it. In certain simplifying cases a slab-model approximation may be useful, and in Chapter V we compare this approximation with the exact results for a coated sphere. (The method by which the exact results are obtained is detailed in Appendix A). In one instance, for relatively high loss, the approximation is very good, but in others it is not quite as accurate as we would like.

If the conditions of the slab-model approximation cannot be met, then we must find something else to bridge the gap between abstraction and reality. Such a bridge could again be a numerical solution of the integral equations, but instead of using the surface impedance boundary condition, it should be based on the specifiable electrical properties of permittivity, permeability and conductivity. A generalized program to do this does not exist at the moment (although a program called TWOD does handle a specifiable permittivity for E-polarization) and future work should be aimed at satisfying this need. In the absence of a numerical or other theoretical tool, we initiated a series of laboratory experiments using a 35-inch long segment of an ogival cylinder built to the electrical size of that studied with the use of RAM1B. Surface field and far field measurements were made of the bare and coated cylinder and the far field measurements support our previous

contention that a coating may enhance a non-specular contribution. The experimental results are discussed in Chapter IV.

Our experience with RAM1B has shown that the leading edge of a body should not have a high impedance for H-polarization, because this leads to an enhancement, yet something must be done to reduce the strong E-polarized return originating there. An alternative scheme may be to shield the edge and in this instance a pertinent program (named RAMC) does exist. Although RAMC handles only E-polarization, it provides for the placement of thin resistive sheets near a body. Because of this feature, RAMC is one step closer to physical reality than RAM1B, since an electrical parameter (sheet resistance) can be specified. Moreover, resistive sheets are currently being produced (for other purposes) by U.S. manufacturers and can be tailored to specific needs. The original program was far too rigid to be applied to the case at hand and had to be modified, and is now called program REST. As mentioned in Chapter III, the modified program duplicated the original program in a test performed on a small cylinder but failed to give the correct values for a larger one. The source of trouble has been isolated and repaired, but REST has not yet been used to study the effects of specific placement and resistance variations on the three obstacles of interest. A program listing and description of REST is given in Appendix B.

Thus far in the contract we have been able to use RAM1B only for H-polarization because of troubles discovered in the results produced for E-polarization. Although RAM1B handles blunt obstacles equally well for either polarization, edged structures require some care for E-polarization. Apparently the surface sampling density must be increased in the vicinity of the edge in such a way that adjacent sampling points on one surface, say the upper one, are closer together than the nearest sampling point on the lower surface. To satisfy this heuristic criterion

requires that the surface be sampled at increasingly finer intervals as the edge is approached. Since the upper and lower surfaces come infinitesimally close together at a true knife edge, we would have to allocate an infinite number of points for the job. This impossible condition can be circumvented by giving the edge a small but finite radius and, as discussed in Chapter III, such a procedure comes as close as any tested thus far to producing the true scattered field.

II. THE WEDGE CYLINDER

The wedge-cylinder is the two-dimensional analog of the cone-sphere and is formed by smoothly mating a segment of a circular cylinder to a wedge. We have consistently used a total internal wedge angle of 25 degrees and a cylinder radius, a , such that $ka = 3.0$, and we have studied primarily the case when incidence is in the plane of symmetry and impinging on the edge. Edge-on incidence was chosen because the radar cross section is higher there than for other angles in the end-on region and the electrical size $ka = 3.0$ places the body near a peak in the oscillatory curve of H-polarized cross section versus frequency. For these conditions of size and direction of incidence, there are but three scattering contributors: the edge, a creeping wave, and a pair of joins. The join contribution is the largest of the three and the edge the smallest, so that any treatment that suppresses the join and creeping wave will produce a net cross section reduction.

2.1 Review of Previous Results

In our previous report (Knott and Senior, 1973) we pointed out that the creeping wave and diffraction from the join and the edge all affect the surface currents induced on the bare body. The join diffraction and the launching of the creeping wave back in the direction of incidence produces a standing wave pattern on the wedge face currents whose periodicity is very nearly $\lambda/2$. Diffraction from the edge propagates along the wedge face in almost the same direction as the incident wave and the resulting interference pattern has a long period that far exceeds the length of the wedge face. The net pattern produced by all three mechanisms is a surface current distribution whose mean value is substantially less than the physical optics value and upon which is superposed a gentle

oscillatory structure with a period of about $\lambda/2$. The currents are shown in the uppermost trace in Fig. 2-1, taken from the previous report.

When the body is given a constant surface impedance, which is to say, an impedance having the same value at all points on the profile, the surface currents become smaller, as shown in the two lowermost traces of Fig. 2-1. Although such impedances tend to wipe out the creeping wave and join contributions, and suppress the surface currents as well, they can increase the edge diffraction component if the edge itself is included in the impedance specification. The result is that constant loading at first reduces the scattering but as the impedance is increased beyond a value lying somewhere between 188 and 377 ohms, the scattering is increased. Thus, at least for H-polarization, it is best to keep the surface impedance below, say, 188 ohms within 0.2 or 0.3λ of the edge.

Since the join and creeping wave contributions dominate the H-polarized wedge-cylinder non-specular scattering, we sought to place centralized loads at the join and antipode. These load profiles had a Gaussian shape with the peak value of impedance centered at either the join or the antipode. The Gaussian shape was chosen to avoid the cusps that might be generated when, for example, linear or square law loading profiles are placed back-to-back, since we had previously discovered that discontinuities in the impedance profile generate spurious sources of scattering. The Gaussian loads were not effective and, worse, some of the specific forms we used actually increased the scattering. The cross sections could be reduced only if the loads were spread over a considerable length of surface and, for more condensed loads, we attributed the cross section enhancement to an excessively steep rate of impedance change.

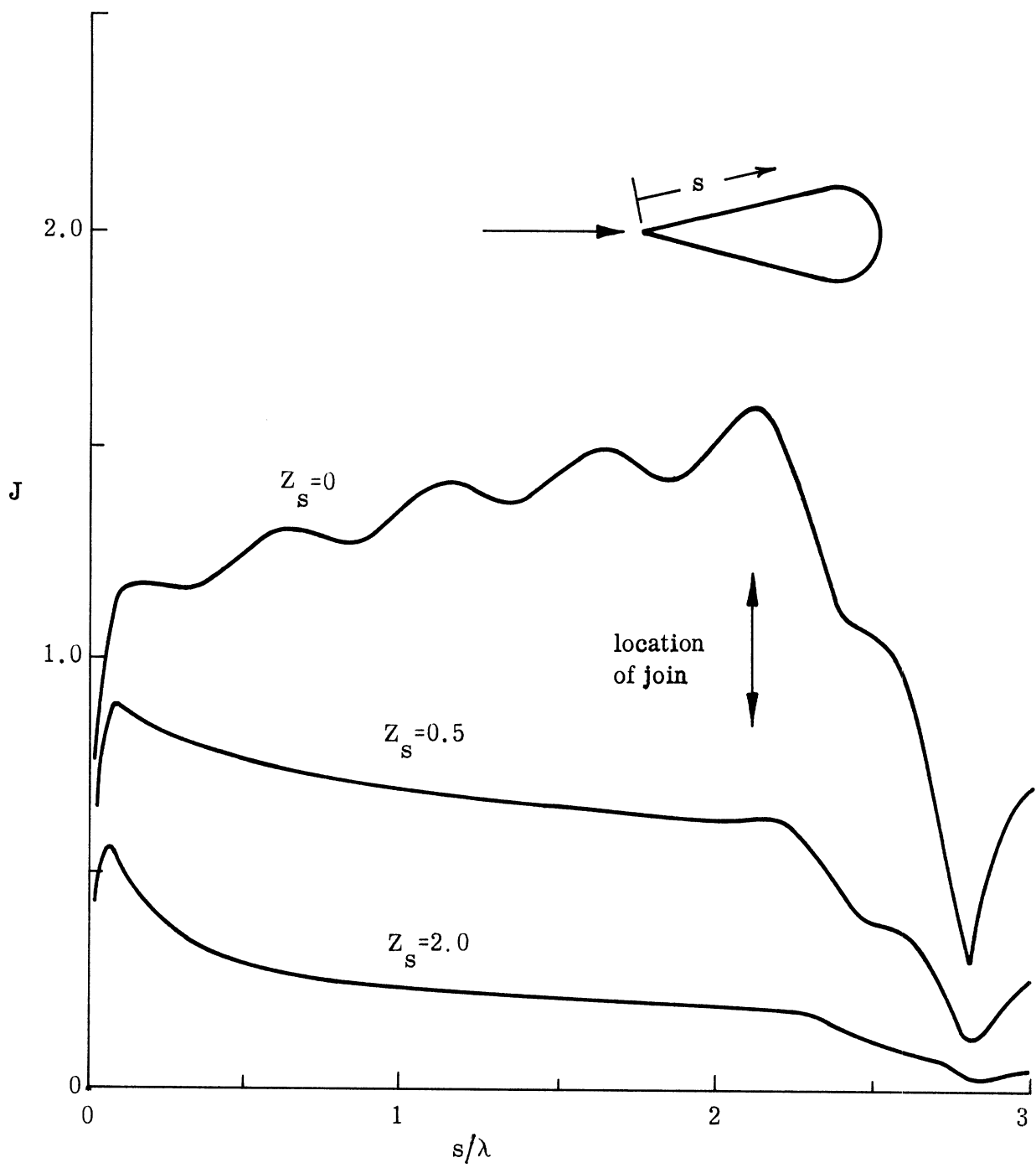


Fig. 2-1: Computed surface currents for a wedge-cylinder at axial incidence.

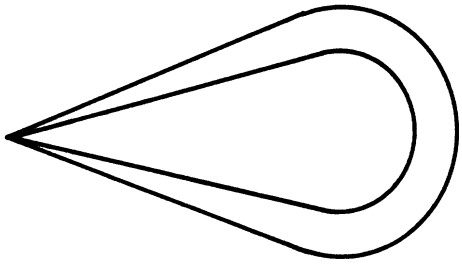
2.2 Other Loading Variations

During the time that has elapsed since the last report was written we have tested six kinds of impedance variations. The six are sketched schematically in Fig. 2-2, in which the relative surface impedance is indicated by the radial stand-off distance between the bare body and the impedance profile. The most extensive coverage we used was provided by a linear rate of change over the wedge faces and matched to a constant level around the rear of the body, as indicated in the upper left diagram. This scheme has the virtue of maintaining a small impedance in the vicinity of the edge, thus minimizing any edge enhancement, while at the same time greatly suppressing the join and creeping wave contributions. We obtained our best scattering suppression with this particular coverage.

The next two sketches on the left side of Fig. 2-2 illustrate a relaxation of the best coverage, in that the leading $1/3$ and $2/3$ of the wedge faces, respectively, have been bared in an effort to reduce surface coverage. The impedance change is still linear, but it commences at a point $1/3$ or $2/3$ of the distance between edge and join, aft of the edge. Note that both of these relaxed coverages produce stronger impedance discontinuities at the join than occurs in the maximum coverage case.

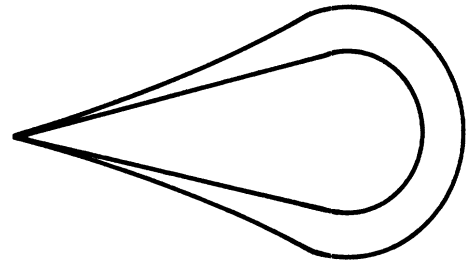
A fourth type of load is obtained by restoring complete coverage to the wedge face, but by now imposing a square law impedance variation instead of a linear one. This produces the profile shown at the upper right, and note that, even though the entire wedge face is covered, the square law variation presents a sharper discontinuity at the join than does the linear one. Two final variations are obtained, as illustrated by the remaining sketches on the right side of Fig. 2-2, by completely baring the wedge face and installing either

linear change on wedge,
constant on the rear

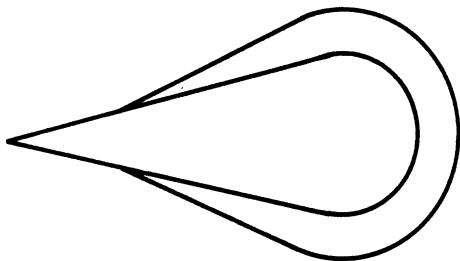


entire wedge covered

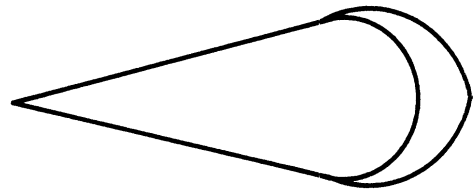
other combinations



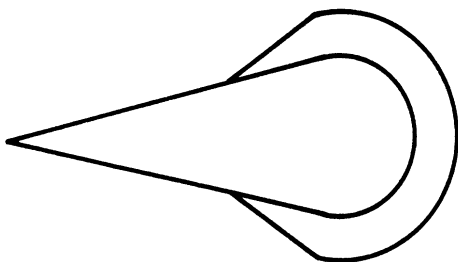
square law rate on wedge,
constant on the rear



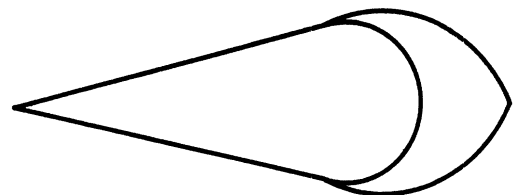
1/3 of wedge bared



wedge bare, linear change
on the rear



2/3 of wedge bared



wedge bare, square law
rate on the rear

FIG. 2-2: Surface impedance profiles.

a linear or square law loading on the cylinder. Since the cylinder loading commences at the join, there is some coverage of the shadow boundary, but this will be of little value in reducing the strength of the creeping wave launched there. Instead, creeping wave suppression occurs because of the surface impedance carried into the shadow boundary.

Bistatic cross section patterns of the best case studied (linear load on the entire wedge, constant load over the rear) are plotted in Fig. 2-3. The best edge-on performance available with this loading scheme is obtained with a maximum impedance (on the cylindrical portion) of 2.0 or 3.0 and amounts to a 17.7 dB reduction of the bare body return. Using a different gauge, namely the first off-axis peak, the reduction is somewhat less, amounting to only 13.9 dB and obtained for $R_{\max} = 2.0$.

Similar bistatic patterns are shown in Figures 2-4 and 2-5 for the wedge cylinder with a partially coated wedge face. Expectedly, as the amount of coverage becomes less, the radar cross section rises. With 1/3 of the wedge face exposed (Fig. 2-4) the best reduction is now only 9.4 dB and for the 2/3 exposure, 8.2 dB. This is obtained in the first case with $R_{\max} = 1.9$, and in the second with $R_{\max} = 1.0$ or 2.0. Note that, for several loadings, there is a possibility of cross section enhancement in the region of the null of the bare body at 26 degrees. An examination of the ripples in surface field distributions that produced these patterns shows that as R_{\max} is increased beyond a value of about 1.0, the discontinuity in impedance at the commencement of loading is responsible for the poorer performance than obtained with the fully loaded wedge face of Fig. 2-3.

When the entire body is fully covered and the wedge faces given a square law surface impedance variation, the results of Fig. 2-6 are obtained. The cross sections plotted there are not quite as low as those in Fig. 2-3 for the linear variation over the wedge face, again because of the discontinuity in the rate of change of the impedance at the join. We shall return to these data in a moment.

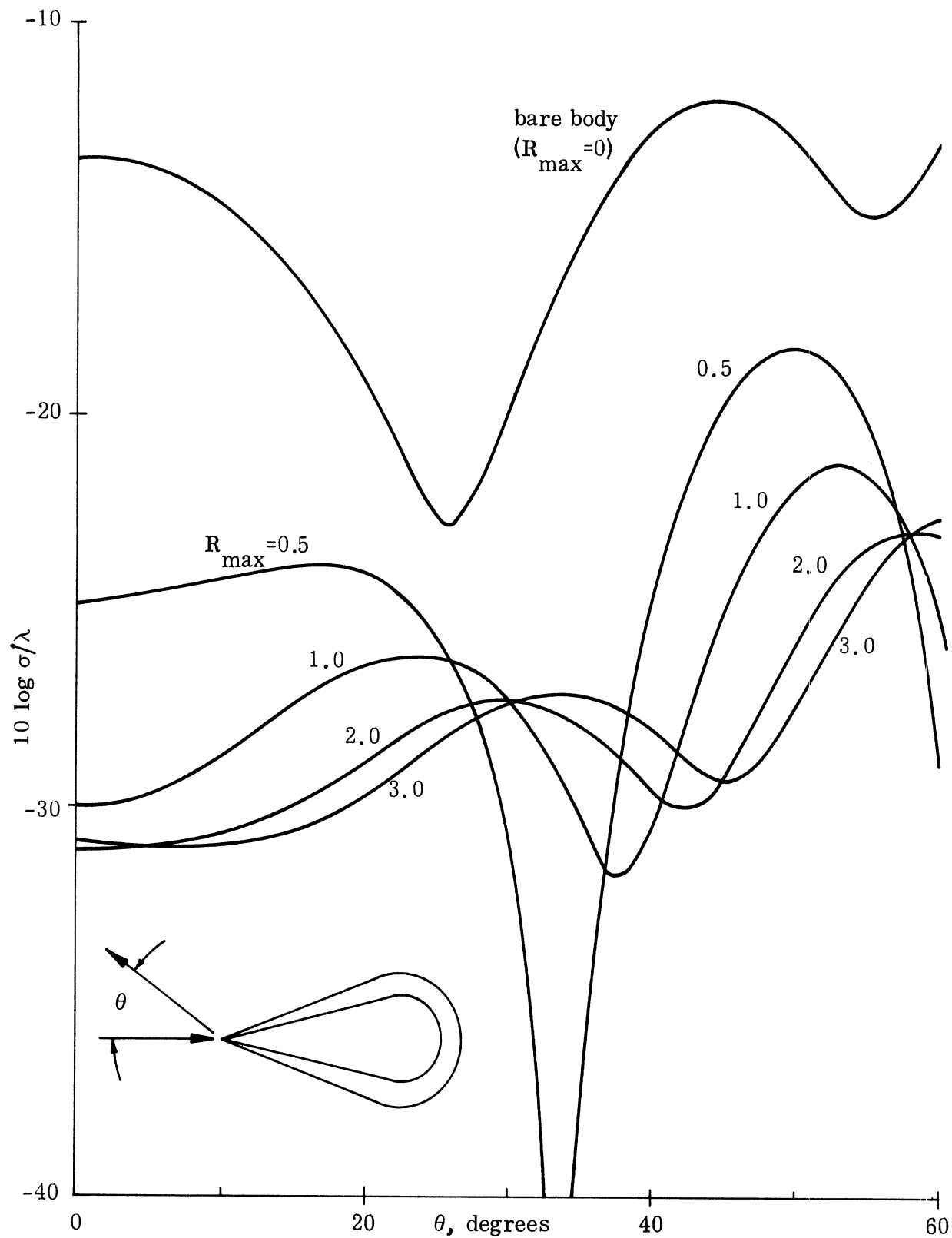


FIG. 2-3: Bistatic cross section patterns for completely covered wedge-cylinder at H-polarization.

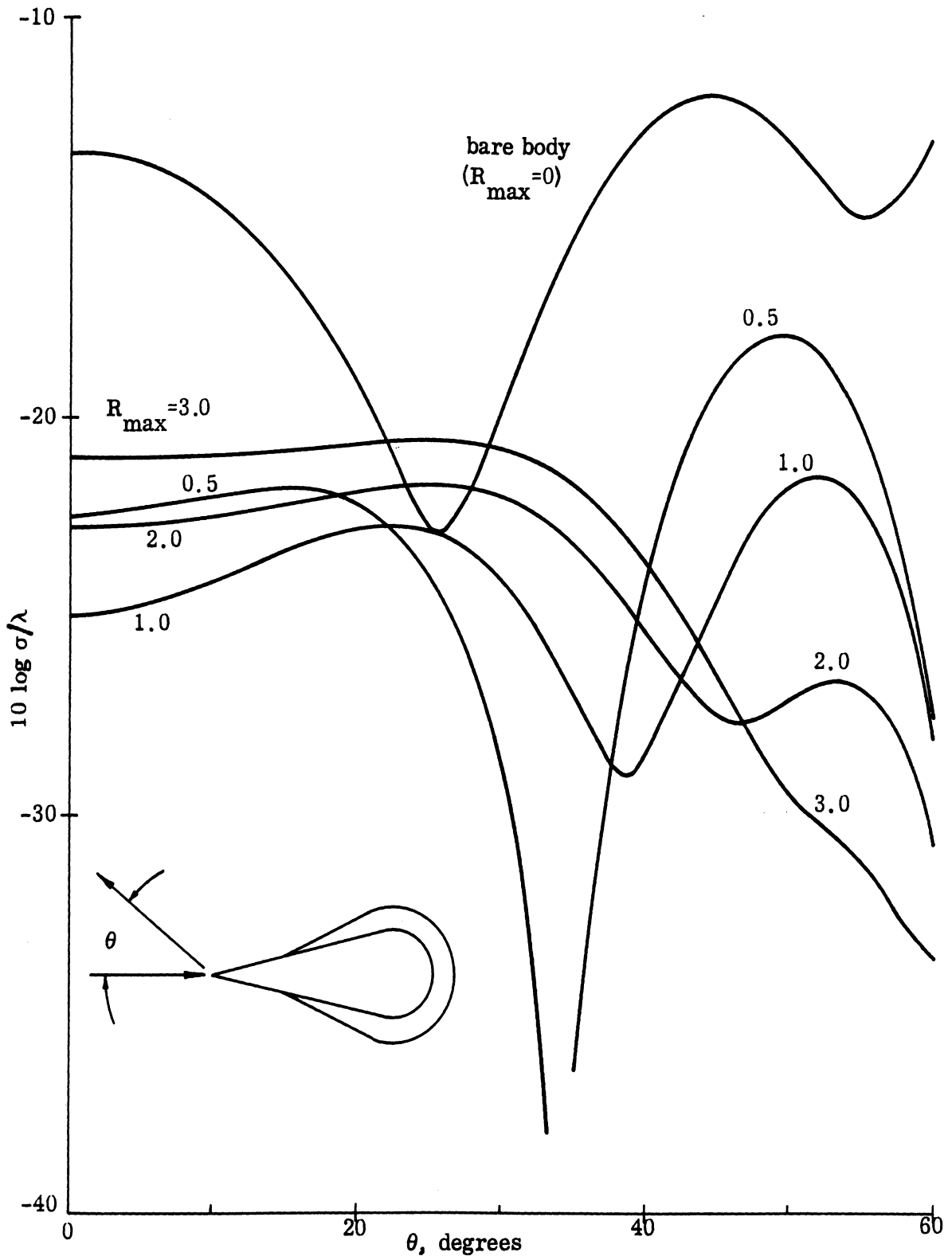


FIG. 2-4: Bistatic cross section patterns for partially covered wedge-cylinder at H-polarization.

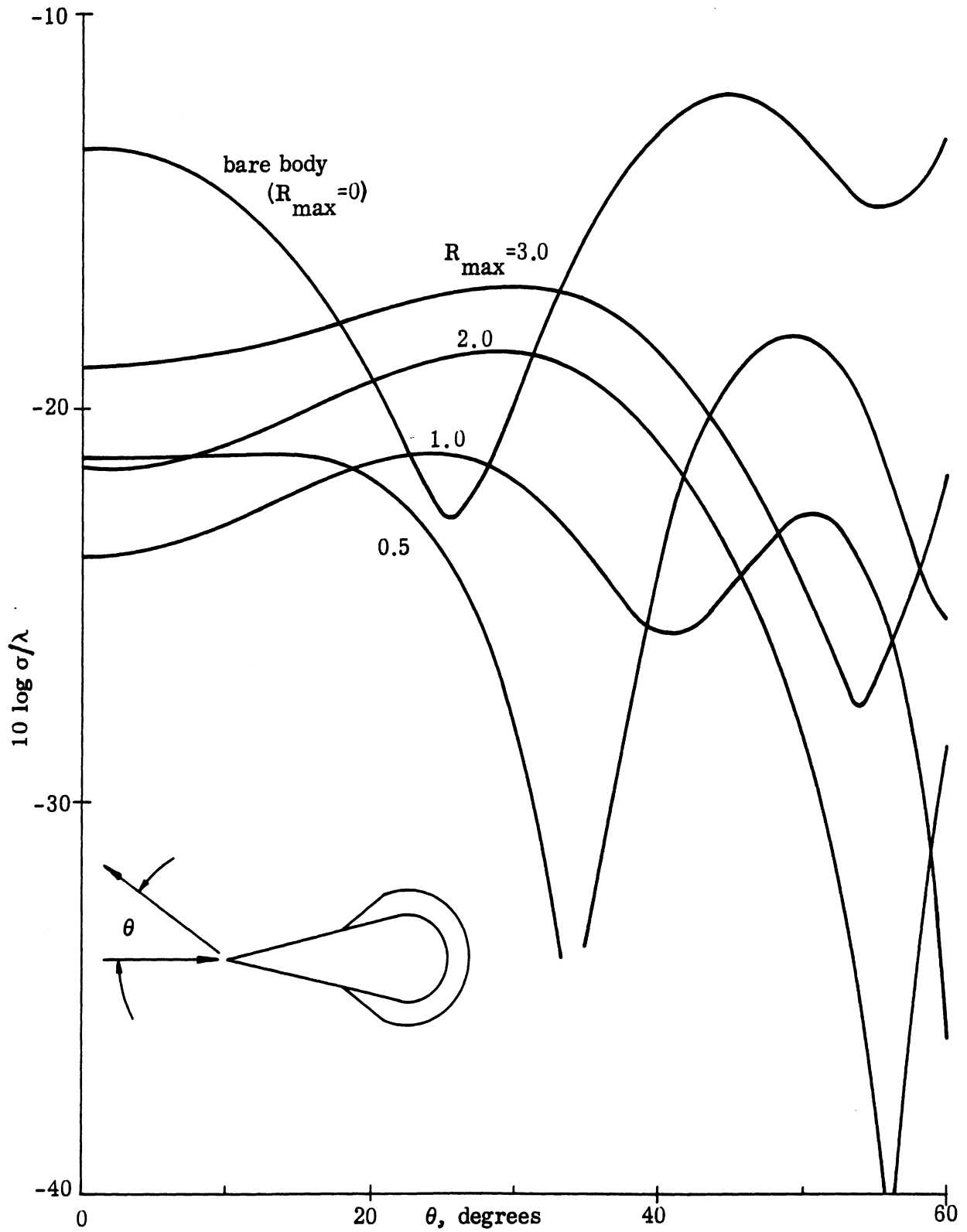


FIG. 2-5: Bistatic cross section patterns for partially covered wedge-cylinder at H-polarization.

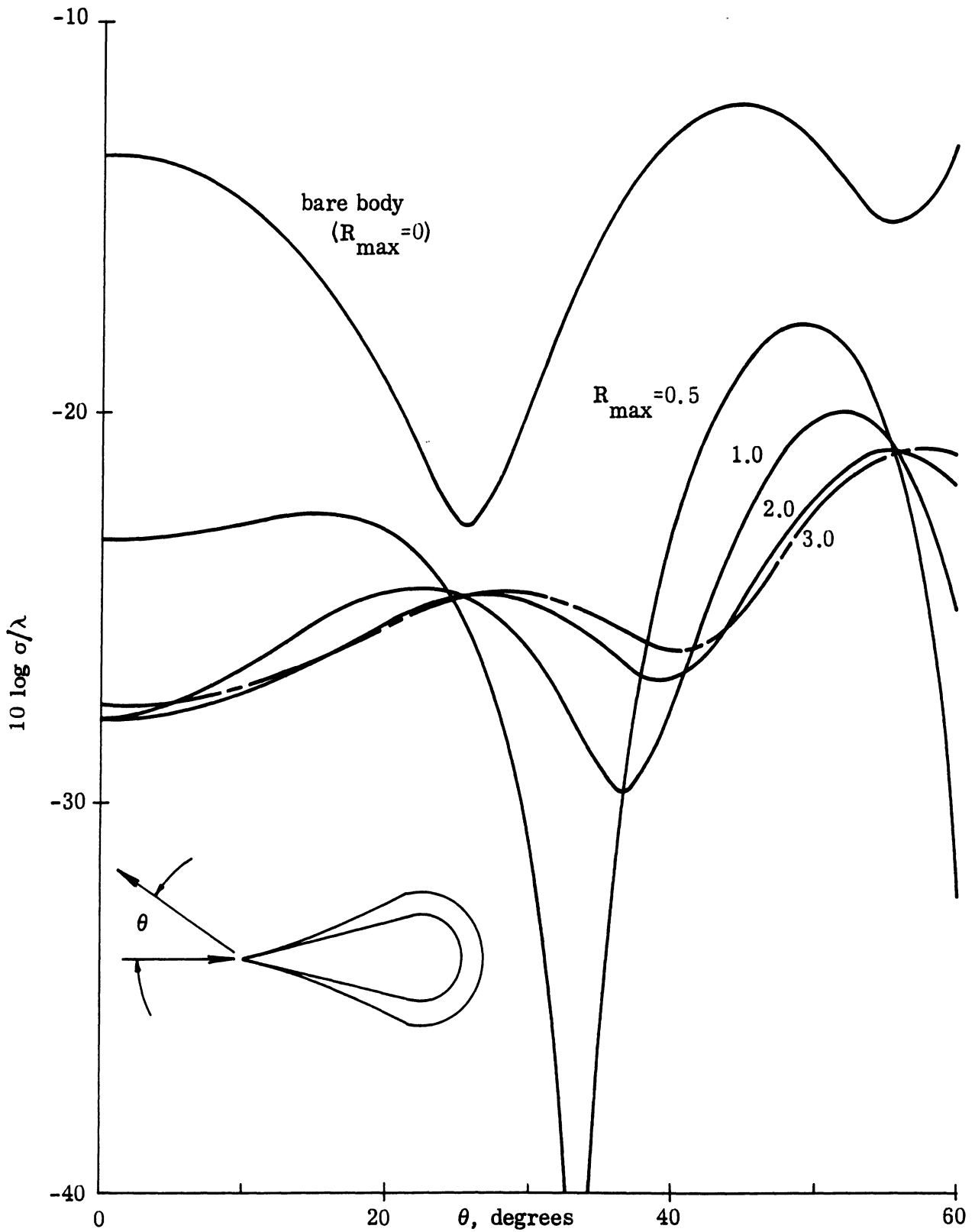


FIG. 2-6: Bistatic cross section patterns of completely coated wedge-cylinder having square law variation over the wedge face.

If the wedge is completely exposed with the surface impedance specified only over the circular cylindrical portion of the body, we obtain the plots shown in Figures 2-7 and 2-8. The first (Fig. 2-7) is for a linear load variation and the second is for the square law variation, but note that neither performs as well as when some impedance is placed on the wedge. Note also that the cross section patterns are very similar to that of the bare body, with the first off-axis null occurring persistently in the same aspect angle region. The loading serves only to suppress the creeping wave and, since this contributor is not as strong as the join, the reduction is modest. These results are consistent with those reported in the previous report involving Gaussian loads placed at the rear of the body.

Summaries of the effects of loading the wedge faces while maintaining a constant load over the rear of the cylinder are plotted in Figures 2-9 and 2-10. Figure 2-9 is based on the strength of the edge on cross section while Fig. 2-10 is based on the largest return in the bistatic patterns out to the first null. Figure 2-9 gives a more optimistic picture than Fig. 2-10 because the cross section patterns of the loaded body tend to rise as the scattering direction moves away from the edge-on aspect angle. Both figures lead to the same qualitative conclusion, however, with the difference between them being only the quantitative values that can be read from the plots.

If the entire surface of the body is available for loading, then a linear load variation should be chosen over a square law variation, as suggested by the 2 to 3 dB difference between the two lowermost curves. The two uppermost traces show that performance falls off as less wedge surface is used and, although we have no data to support it, it is our belief that linear load variations should also be used (instead of square law) over a partially coated wedge face. Note that each trace has a minimum level, which suggests that a further increase of R_{\max} is of no value and, indeed, in several cases R_{\max} should not be permitted to increase beyond certain values lest the benefit of the loading scheme be lost. An optimum value seems to be near $R_{\max} = 1.0$, but this conclusion might be subject to change if the discontinuities in impedance slope can be removed.

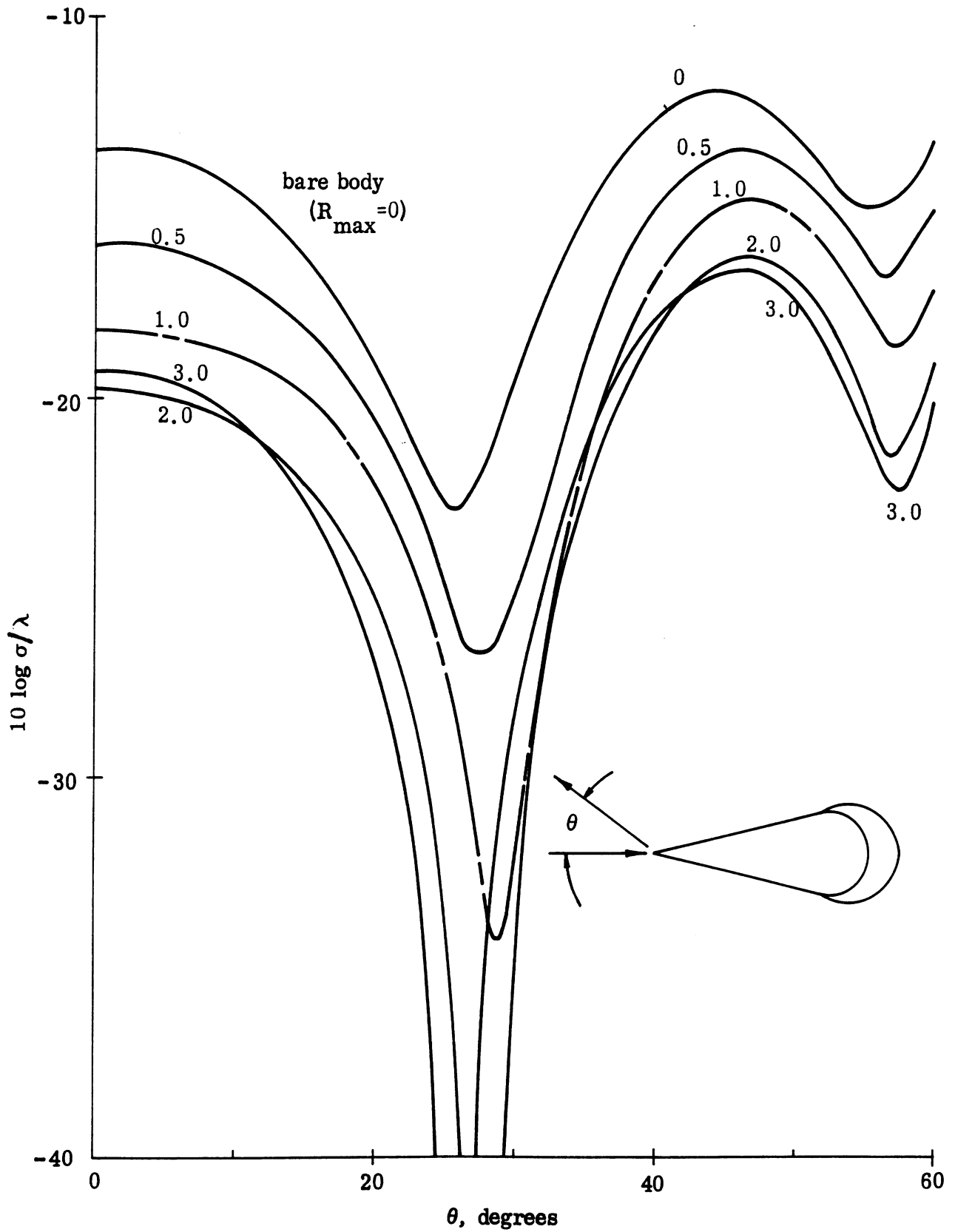


FIG. 2-7: Bistatic cross section pattern of wedge-cylinder with bare wedge faces and linear load in the rear.

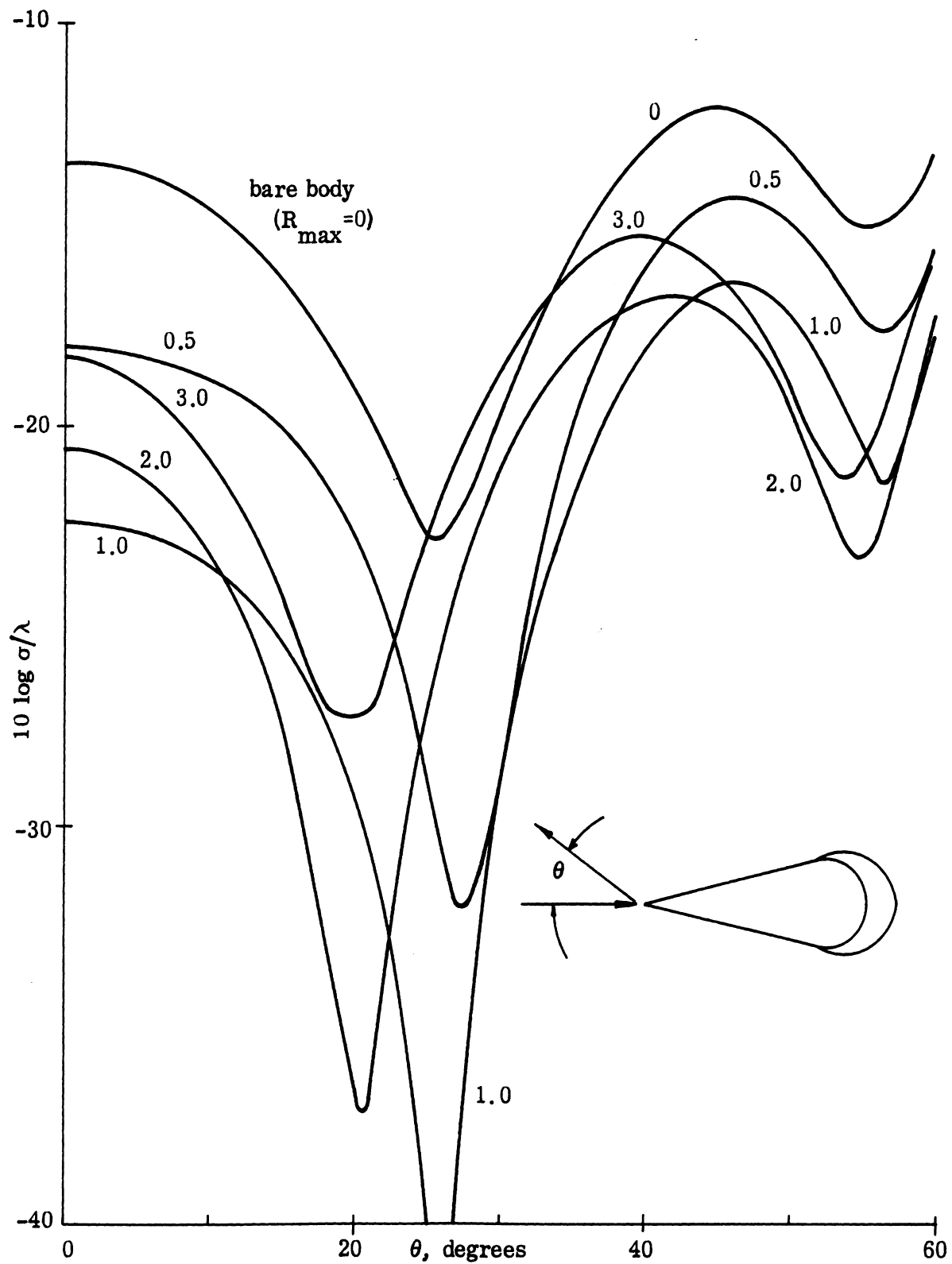


FIG. 2-8: Bistatic cross section patterns of wedge-cylinder with bare wedge faces and square law load in the rear.

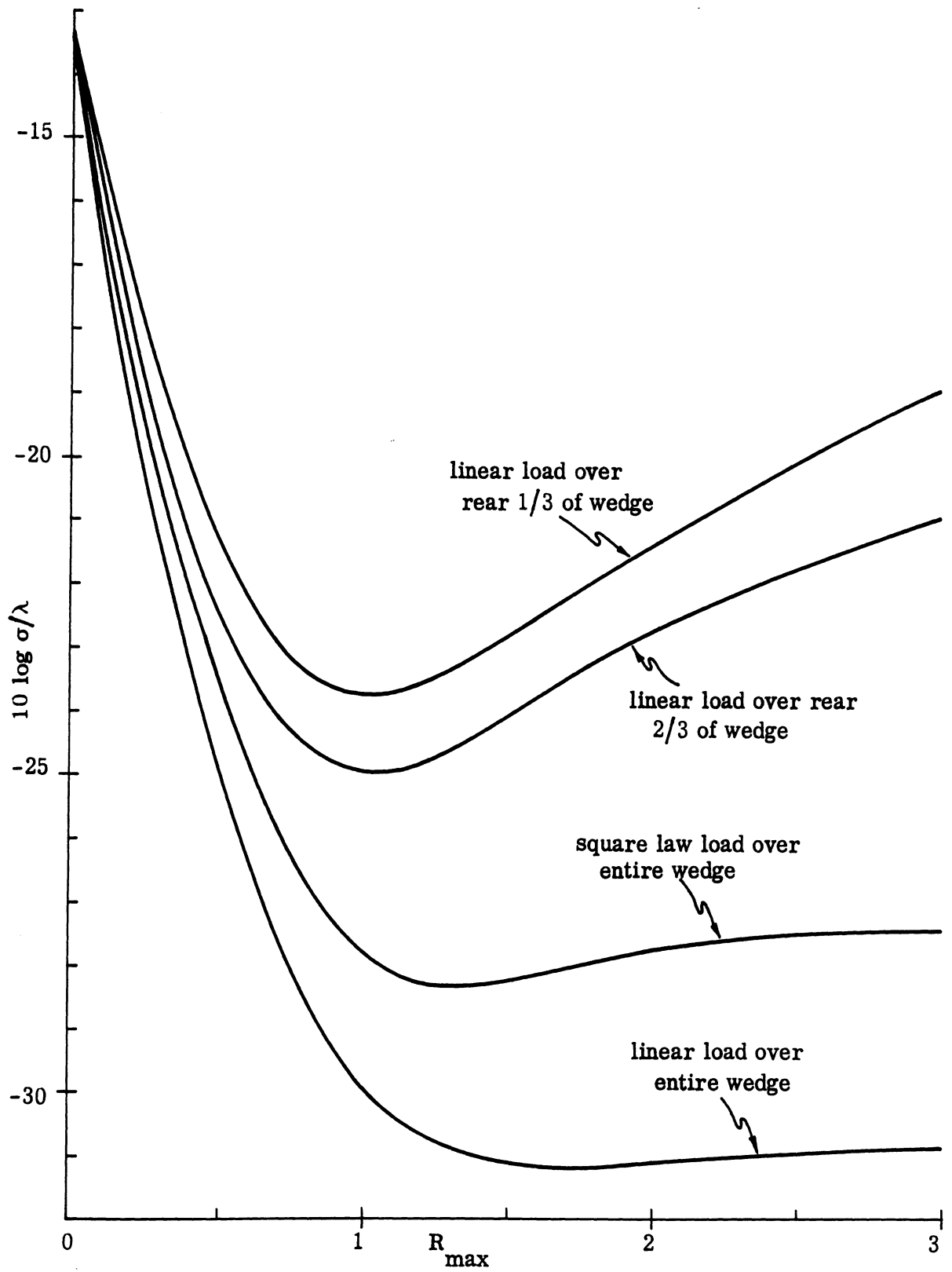


FIG. 2-9: Edge-on cross section of wedge-cylinder with constant load in the rear.

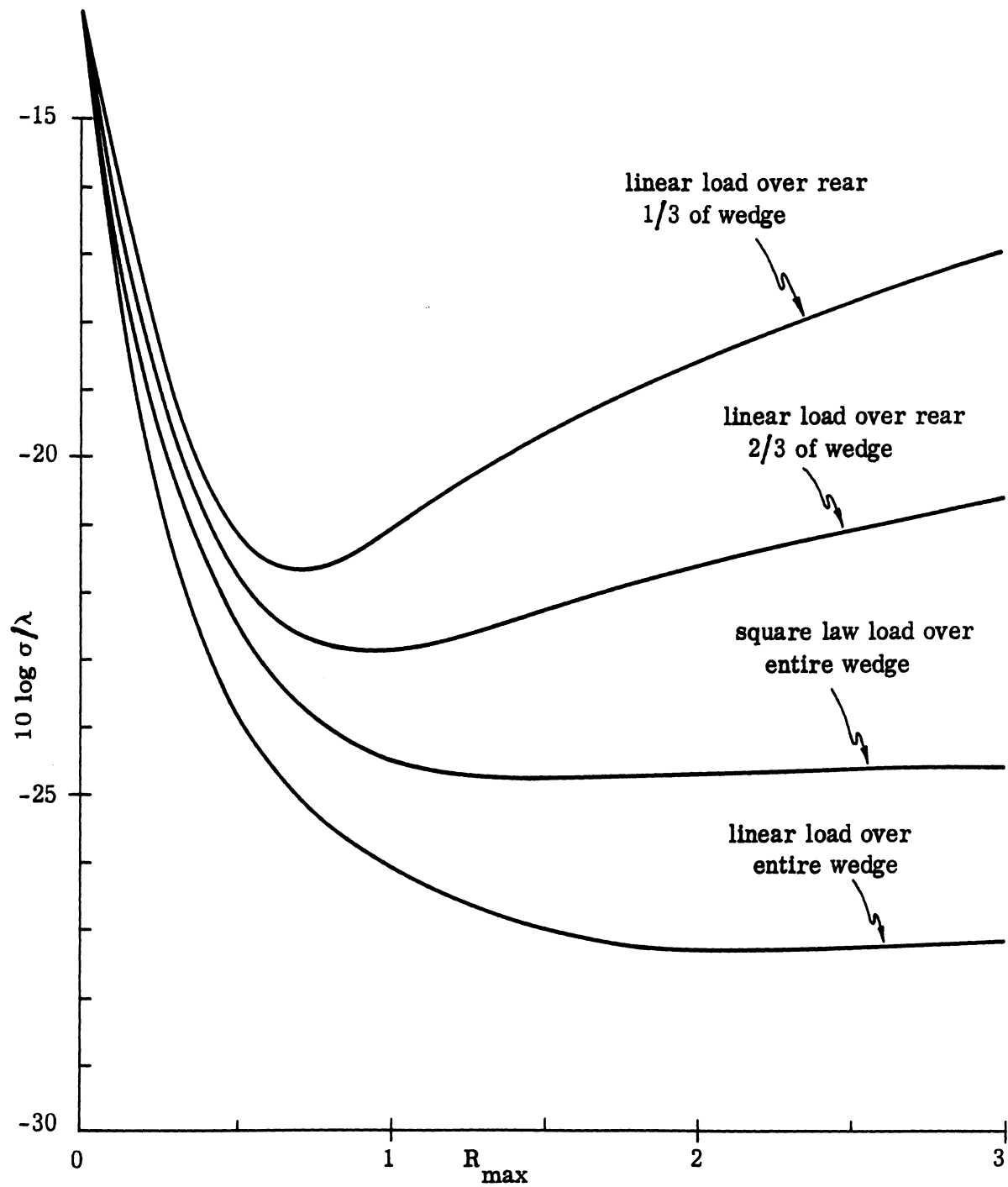


FIG. 2-10: Values of the peak cross section in the edge-on region of a wedge-cylinder as a function of the maximum impedance.

If the entire wedge face is left bare and the loading placed only over the cylindrical portion of the body, we obtain the plot shown in Fig. 2-11. The cross section reduction obtainable is much less than if the wedge faces are also available for coverage. Note that a linear loading variation is more effective than the square law and that the optimum value for this case is about $R_{\max} \approx 1.3$.

As pointed out in our previous report, both the join and creeping wave contributions decrease with increasing frequency so that, provided favorable impedance profiles can be maintained with changing frequency, performance will improve as the wavelength becomes shorter relative to the dimensions of the body. Moreover, less of the physical surface is then required to build up the desired impedance function and this could lead to a reduction in the amount of surface to be treated. Because of the limited number of sampling points in program RAM1B, however, these expectations could not be checked via the program itself and are based upon our previous knowledge of the nature of the scattering. Indeed, because of the relatively small size of the bodies actually considered, we could not suppress creeping wave and join returns individually. The amount of surface required to treat one of them alone was extensive enough that the other was also affected.

In summary, maximum reduction of the bistatic scattering from the wedge cylinder in the edge-on region takes place only when all of the surface is utilized for the loading. A single exception is the apex of the wedge, which should be left bare, lest the scattering be enhanced by the gradual conversion from an H-type edge scatter to an E-type. In all cases a linear impedance variation increasing from front to back proves better than a square law variation. Exposing leading portions of the wedge faces in an attempt to minimize the amount of surface to be treated generally leads to a loss of performance which cannot always be recovered by carrying the impedance to a higher terminating value. Indeed, if the impedance rise must take place in too short a distance, there is a distinct hazard of generating new sources of scattering at points where the variation starts and ends. It would be prudent to smooth out these discontinuities and, if given the opportunity, we plan to do so to see if any improvement in performance can be obtained.

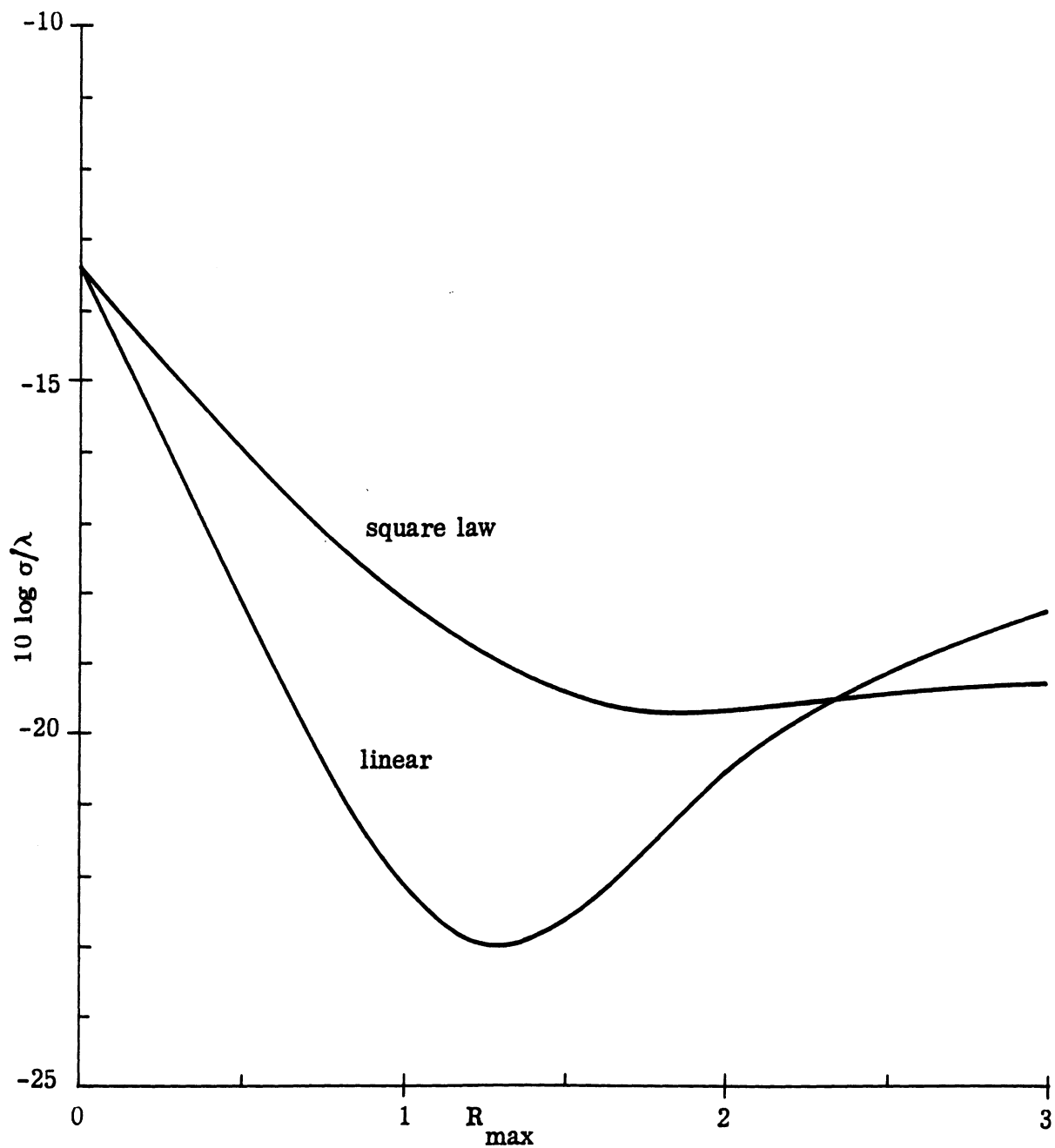


FIG. 2-11: Edge-on cross section of the wedge-cylinder with bare wedge faces and loading over the cylindrical surface.

III. E-POLARIZATION

As mentioned in our previous report (Knott and Senior, 1973), program RAM1B was used extensively to study the effects of surface impedance loading for H-polarization and many of our conclusions are based on the analysis of data generated by RAM1B. When we turned our attention to E-polarization, however, we immediately discovered what were felt to be anomalous results for both the ogival cylinder and the wedge-cylinder. A close scrutiny of the RAM1B uncovered an error in a subroutine which computes the incident field strength at each point on the surface profile, but even after the program was corrected, we still obtained results that did not agree with those of theoretical standards we had long ago accepted.

The difficulty appears to be not in the program itself, but rather a fundamental limitation of the integral equation approach when applied to bodies having sharp edges. We believe that the method has never received such critical tests as we have imposed and the intent of this chapter is to establish the limitations of the concept for the benefit of others who may consider using it, as well as to show the results of our explorations of ways to circumvent potential troubles. Although it appears that some measure of inaccuracy is likely to persist, the integral equation approach remains a useful one if the user of it is willing to strike a compromise and tolerate some error for edged structures.

3.1 GTD as a Gauge

The reader must appreciate that we undertook this contract using the numerical solution of the integral equation for a two-dimensional obstacle over whose surface an impedance boundary condition is imposed. Naturally we wanted to be sure that the tool (in the form of program RAM1B) was sufficient for our needs and we initially tested it against a circular cylinder and an ogival cylinder for

H-polarization but, unfortunately, only against the circular cylinder for E-polarization. Thus it was some weeks before the E-polarization problem was discovered.

An exact solution exists for the circular conducting cylinder and when RAM1B was tested on this shape for H-polarization, the agreement was good. On the other hand there is no exact solution for the ogival cylinder, but a good high-frequency technique is available in the form of the geometrical theory of diffraction. The elements of the theory were discussed in the previous report and suffice to say that when the results of GTD were compared against those of RAM1B, we obtained acceptable agreement for H-polarization but poor agreement for E-polarization.

We have been using GTD for other purposes for many years and, although we felt it to be fairly reliable, small errors had always been noted. The errors can be reduced if second-order interactions are included in the calculations, but GTD can still be in error by as much as 1 or 2dB. Thus, although the discrepancy between RAM1B and GTD exceeded this amount, we still needed a verification of one or the other. Fortunately an experiment had been planned whose results would reveal the correctness of the theory and they are shown in Fig. 3-1.

Figure 3-1 contains segments of backscattering patterns measured in our experimental facility. The measurements are described in more detail in Chapter IV, and the complete patterns are also presented there, but for our purposes the partial patterns are sufficient. In both graphs (one for E-polarization, the other for H) the aspect angle is measured from edge-on incidence with the final 30 degrees of the pattern leading up to the specular return being omitted. The solid traces represent the measured values, and the dashed traces GTD, and the correction factor discussed in Chapter IV has been applied to convert the three-dimensional cross sections to their corresponding two-dimensional values.

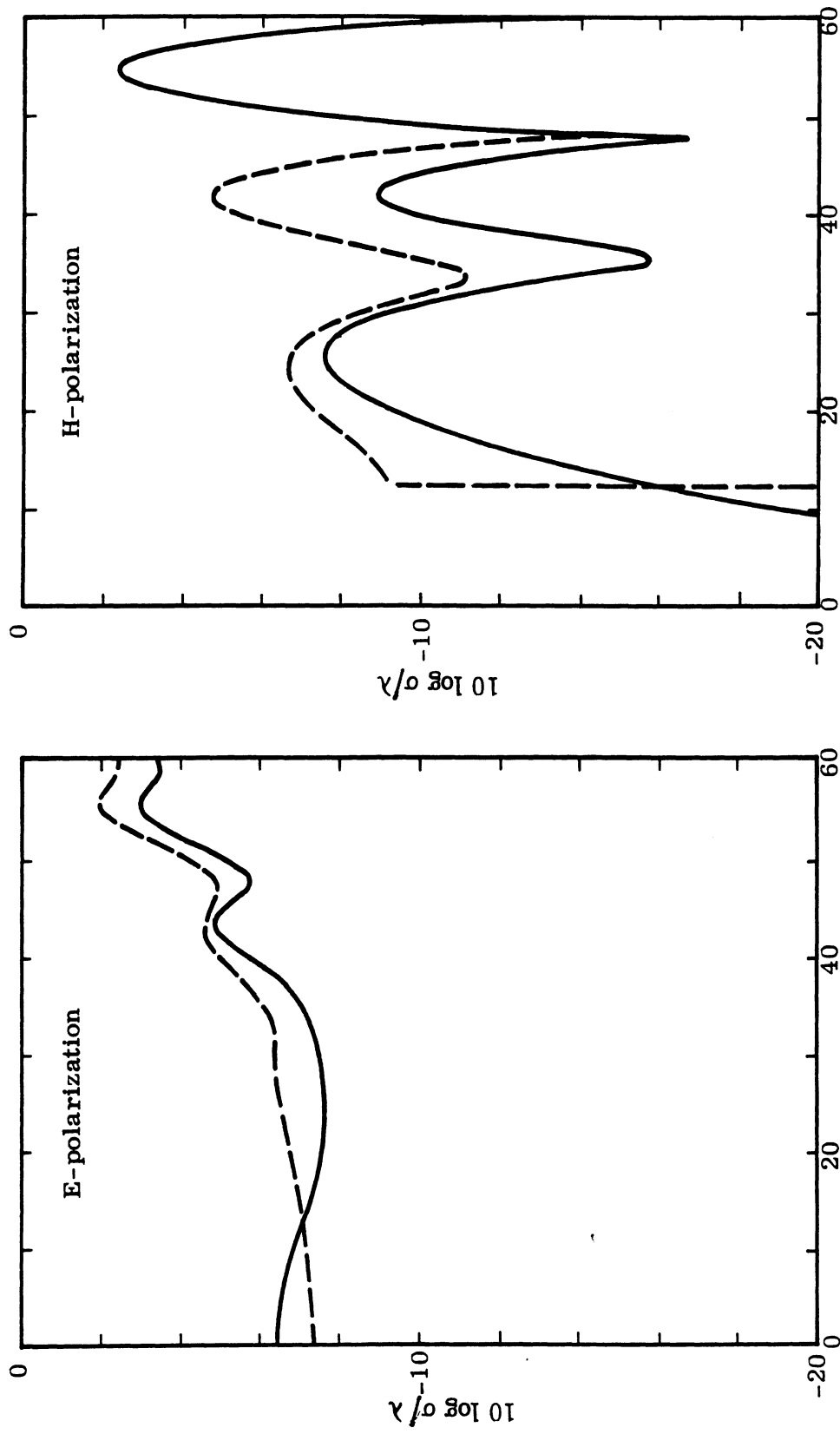


FIG. 3-1: Comparison of measured ogival cylinder patterns (————) with those predicted by first order GTD (-----).

The left hand patterns (E-polarization) are of immediate interest, and note that the disagreement throughout the entire 60-degree range is less than 2dB. Of equal importance is the relative flatness of the pattern, which is altogether consistent with GTD's prediction that the scattering is dominated by the front edge return. Surprisingly enough, the agreement for H-polarization is not as good as for E-polarization amounting to a 4dB error in the strength of the second lobe. Another flaw in this pattern is the sharp jump in the GTD prediction at 12.5 degrees, at which point the rear edge of the ogival cylinder suddenly pops into view.

In spite of these discrepancies, we feel the experiment has justified our reliance on GTD as a gauge, particularly for E-polarization. Since GTD and experimental patterns confirm each other, we now have the means by which to judge the results of RAM1B.

3.2 Early Results of RAM1B

Our first test of RAM1B for E-polarization (after the incident field computation had been corrected) was based on the ogival cylinder with 96 uniformly spaced sampling points. We exercised a subdivision option in the program and specified that each of the profile zones shall be broken down further into 3 sub-zones, the purpose of which was an attempt to obtain more accuracy. The resulting bistatic scattering prediction is compared in Fig. 3-2 against that of GTD* and not only is the disagreement a whopping 10dB, but RAM1B predicts a deep null when there should be, in fact, no null at all.

* We could not use experimental patterns because our measurements are of monostatic, not bistatic, cross sections.

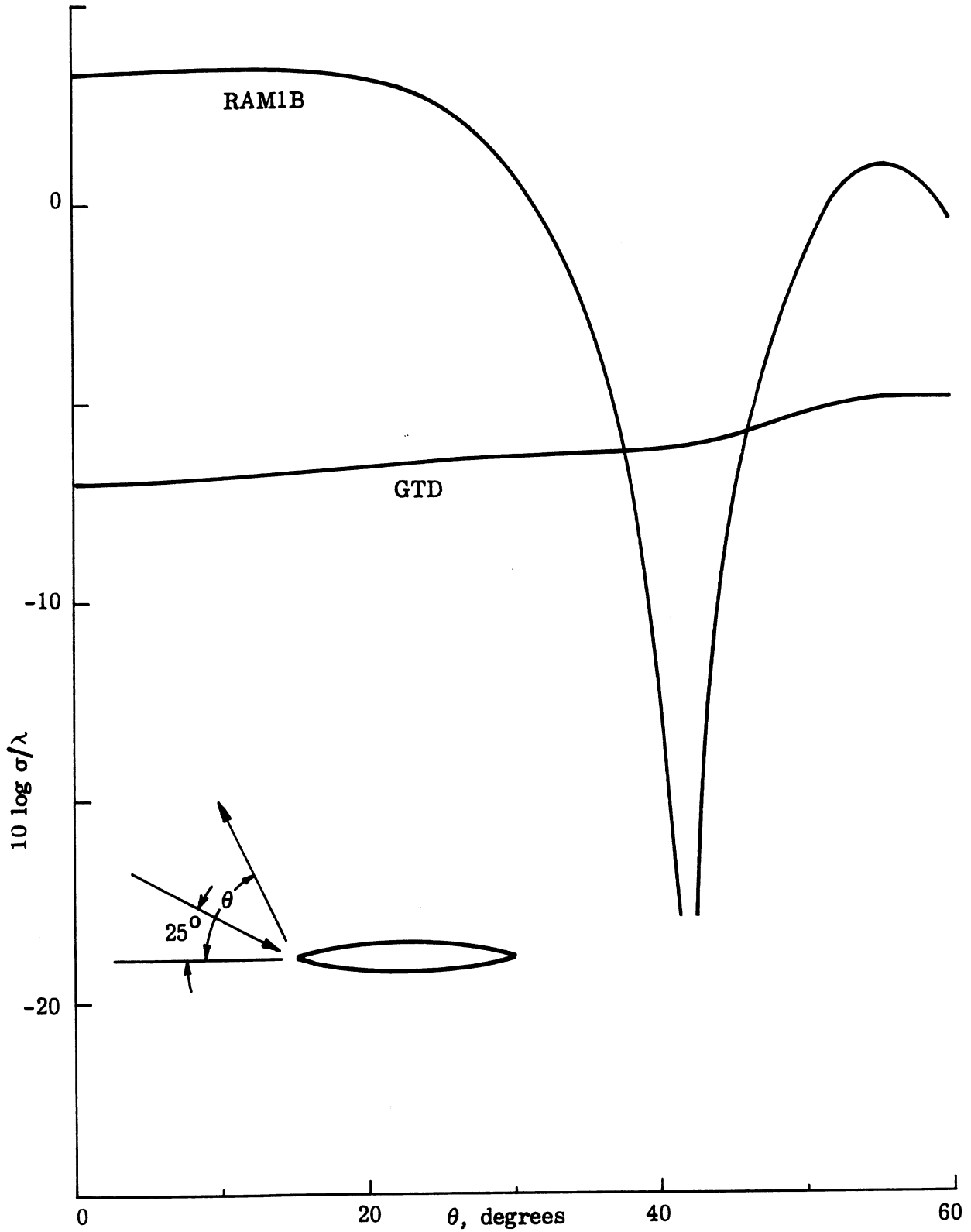


FIG. 3-2: Comparison of E-polarization bistatic scattering predictions for ogival cylinder.

A look at the surface current distribution in Fig. 3-3 shows why: the currents at the rear edge of the body are far too large and, although it is but a single point that carries such a current, the effects can be seen in the current distribution all along the body. There is also a spurious datum at the leading edge and the two combine to produce the large returns in the zero to 30-degree aspect region as well as the deep null at 42 degrees.

The output from RAM1B was clearly unacceptable, since not even the basic character of the true scattering of the metallic body was being reproduced. Earlier tests of the program on circular and elliptic cylinders for E-polarization had been satisfactory and since these were blunt bodies, our next move was to try rounding the ends of the cylinder as shown in Fig. 3-4. The rounding was accomplished by mating segments of small circular cylinders to the ogival cylinder such that the surfaces were tangent to each other at the joins. Four radii of curvature were tested, ranging from 0.02λ to 0.05λ but, due to a software problem that has not been isolated, we recovered scattering results only for the first three.

A total of 16 sampling points were allocated to the small cylinders at the ends (8 at each end) and the remaining 80 points were uniformly distributed over the broad upper and lower surfaces of the ogival cylinder itself. Since the perimeters of the small end caps grow smaller with decreasing radius, the 8 sampling points become more densely packed. The surface current distributions for all four radii were quite similar, except at the ends, and a typical plot is given in Fig. 3-5. By comparison with Fig. 3-3 (and accounting for differences in scale), it can be seen that the current at the rear of the body has been reduced, the current at the front has been increased, and the magnitude of the oscillations has been greatly diminished. Figure 3-6 shows how the peak intensities of the currents at front and rear edges behave with decreasing radius as predicted by RAM1B; the front edge current increases while the rear edge current decreases with smaller radius. Judging by

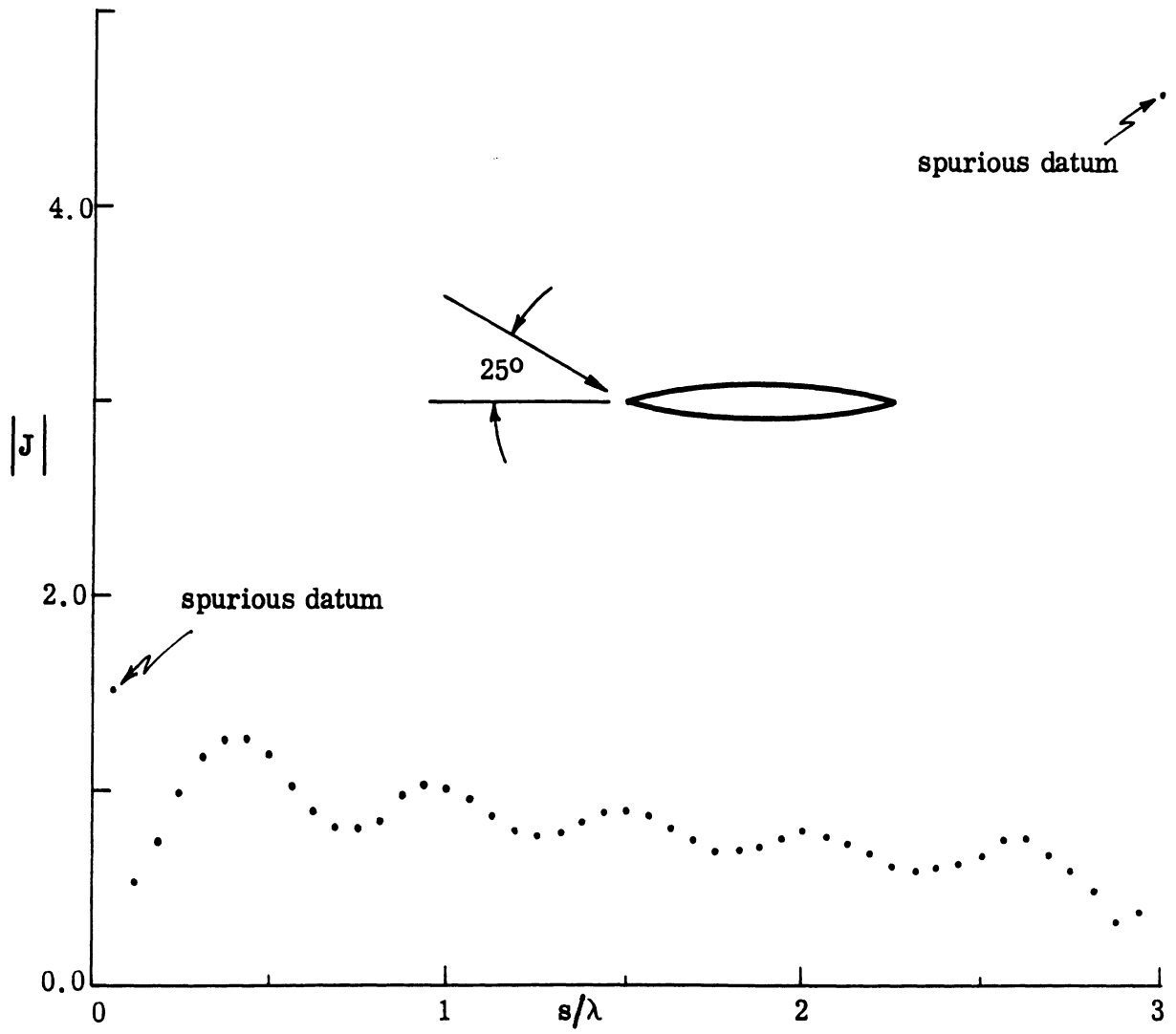


FIG. 3-3: The surface current distribution that produced the RAM1B scattering pattern of Fig. 3-2.

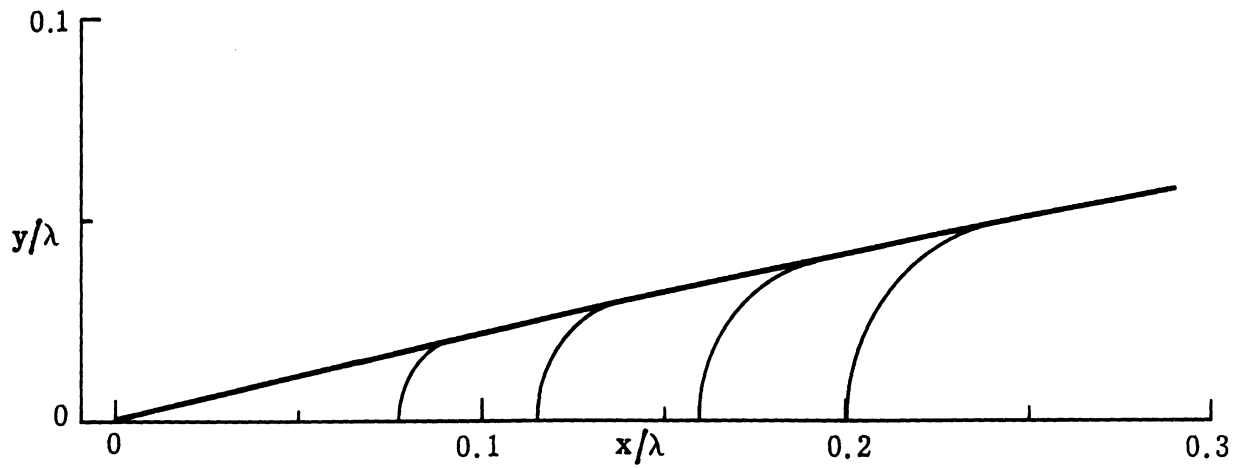


FIG. 3-4: Four radii of curvature were used to relieve the sharp edges of the ogival cylinder. This is a plot of the upper profile near one edge.

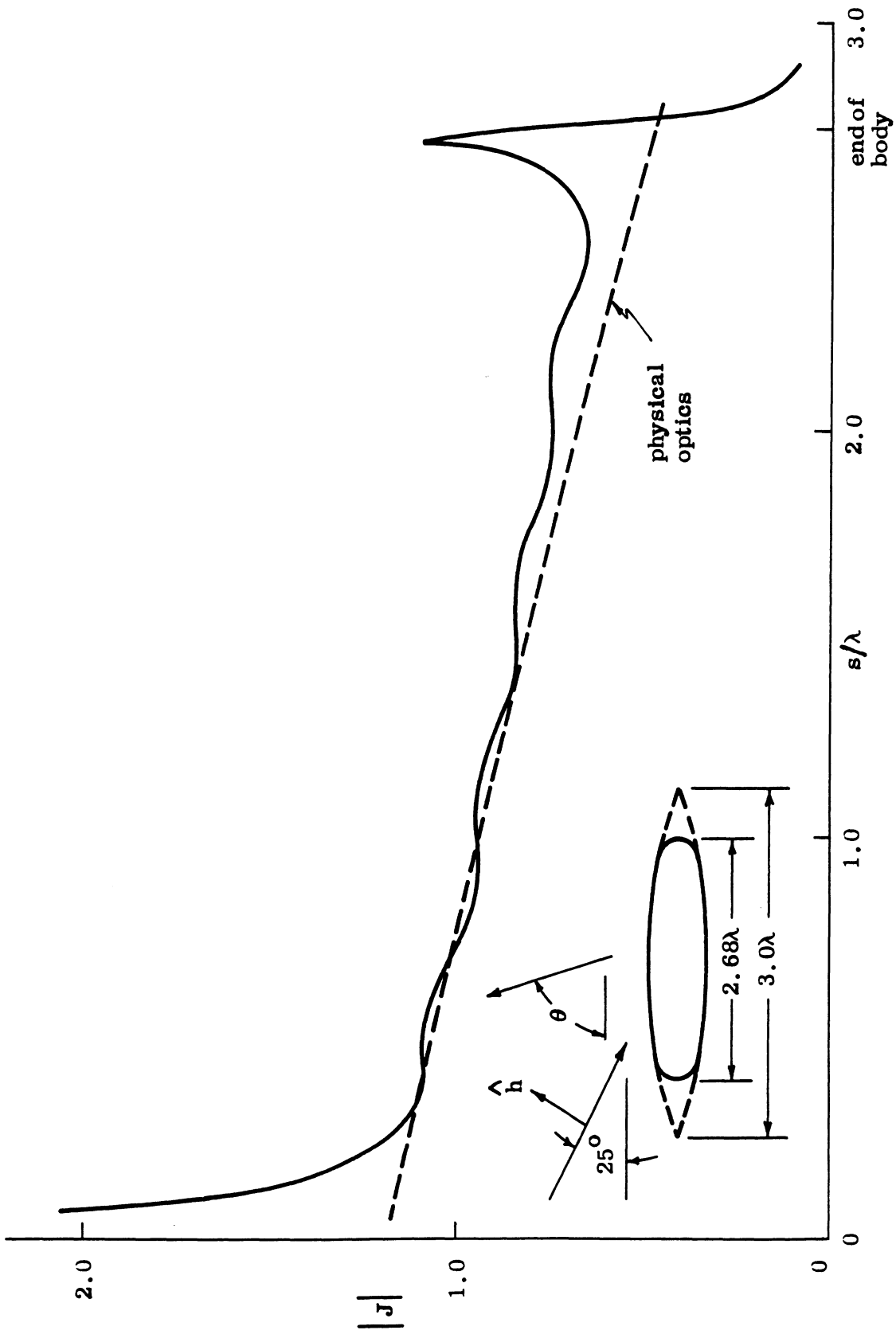


FIG. 3-5: Surface current distribution over blunted 25-degree ogival cylinder, edge radii of 0.04λ .

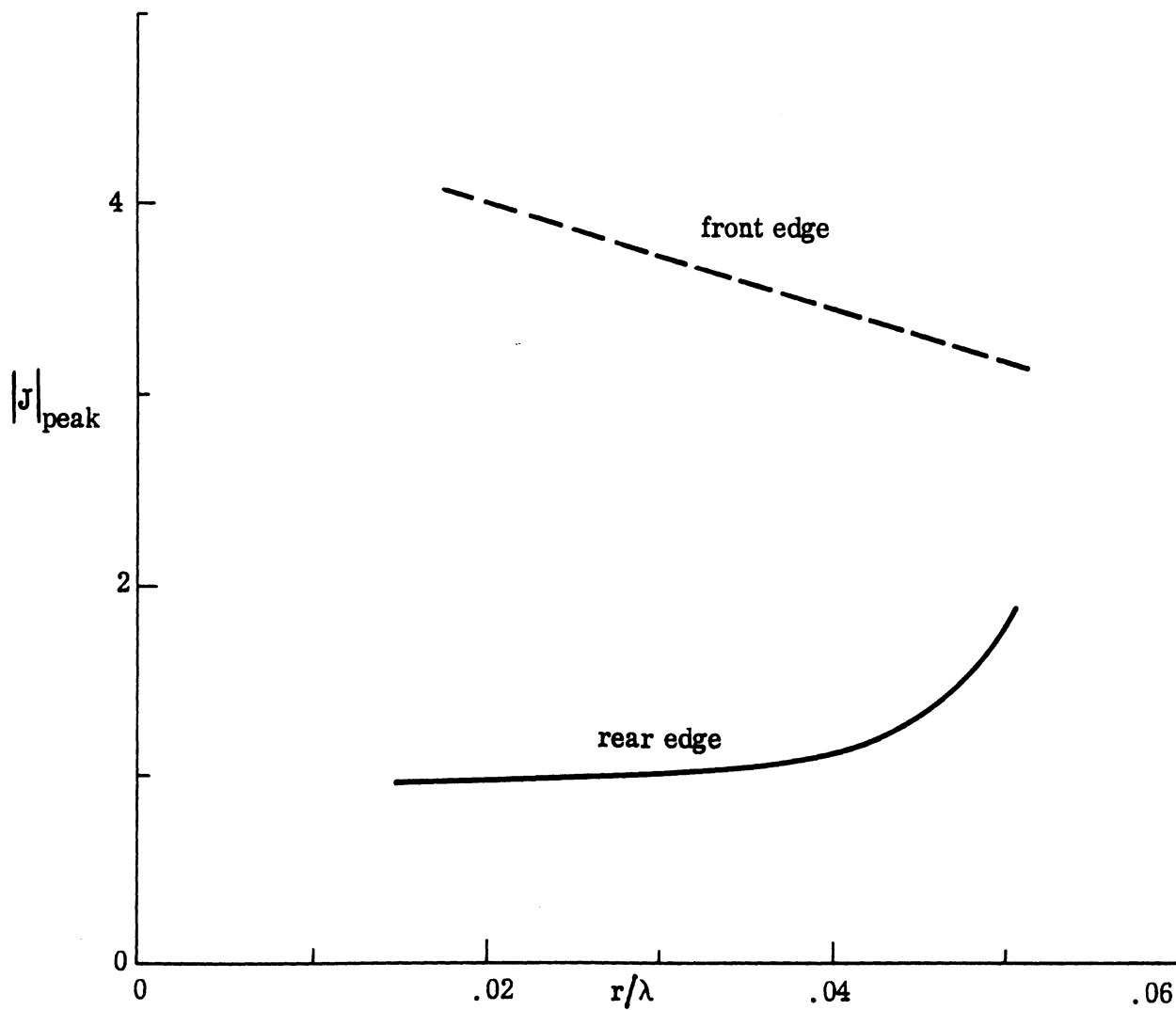


FIG. 3-6: Peak values of front and rear edge currents as functions of the edge radius for 25-degree angle of incidence.

the gentle rate of decrease of the rear edge current, we would guess that, at least as obtained from RAM1B, the current will never reach the physical optics value at the rear, no matter how small a radius is used.

A plot of the bistatic scattering for three radii of curvature is given in Fig. 3-7 and includes the results of GTD for comparison; clearly rounding is beneficial. The error in the scattered field strengths is now no worse than 4dB, a substantial improvement over the 10dB noted in Fig. 3-2 when RAM1B is used unwittingly for a sharp, unrounded edge. Yet Figs. 3-6 and 3-7 both show that better results are obtained for smaller radii of curvature at the edge, a curious fact, since the purpose of blunting the edge was to relieve a sharp edge. The mystery disappears, however, when we recall that the surface sampling rate increases with decreasing radius. Evidently it is the sampling rate and not necessarily the edge radius that improves the agreement and this suggested that perhaps a sharp edge might still be maintained, and thus the geometry preserved, if we could pack the sampling points densely in the vicinity of the edge.

We therefore devised another set of tests on the ogival cylinder in which the sharp edge was maintained but whose profile became progressively more densely sampled. This was accomplished by establishing three discrete segments over the ogival cylinder surface: a central one containing 64 sampling points (32 on upper and lower surfaces), and two end segments containing 16 points each (8 on upper and lower surfaces). The sampling rate in each region was uniform, but as the central region was gradually expanded, the 16 points at each end were progressively compressed into a smaller portion of the surface.

The influence of the sampling rate on the peak value of the current in the vicinity of the edges is shown in Fig. 3-8, in which the abscissa is the distance

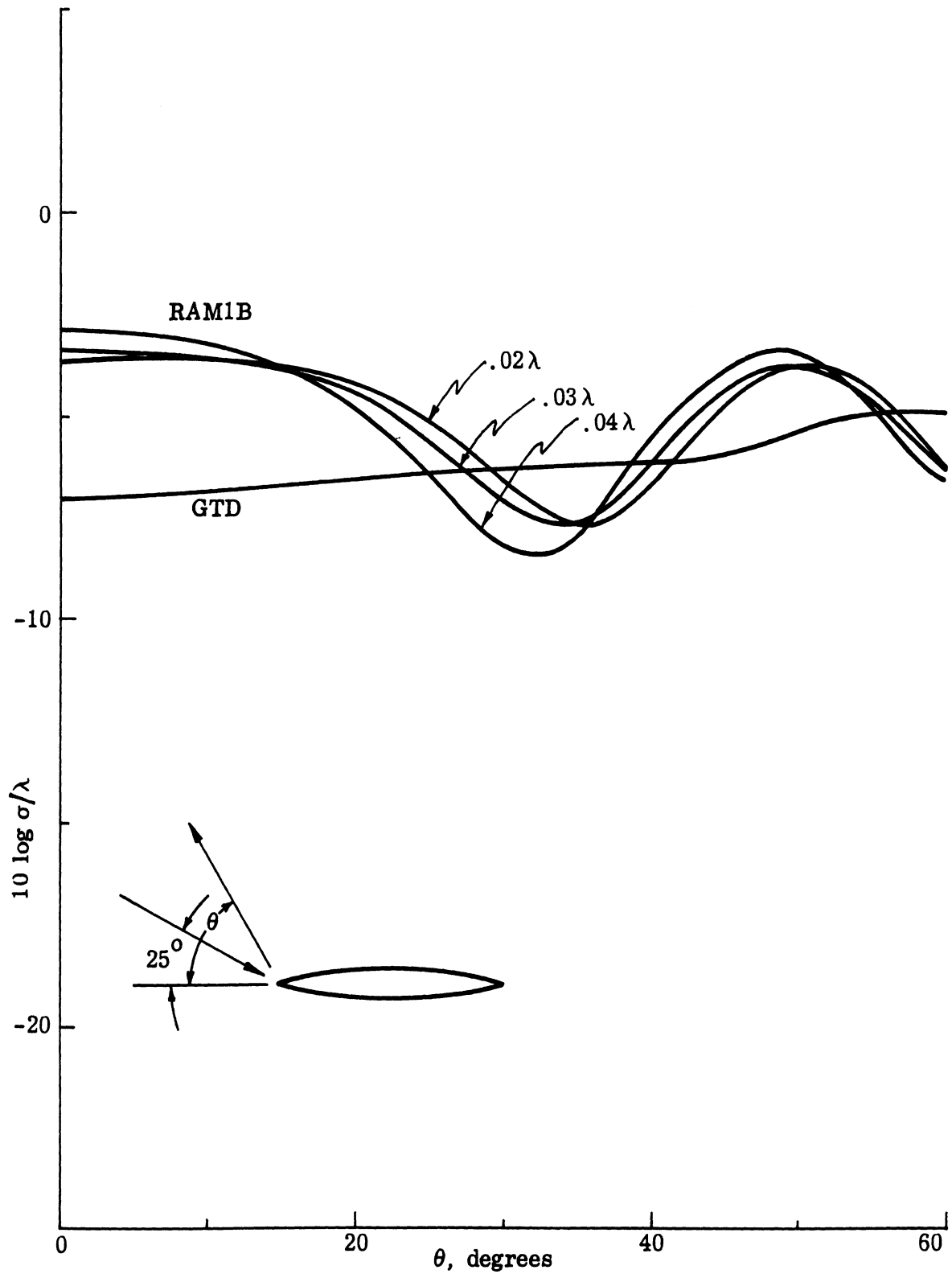


FIG. 3-7: Comparison of bistatic scattering for rounded edges with that given by GTD for a sharp edge.

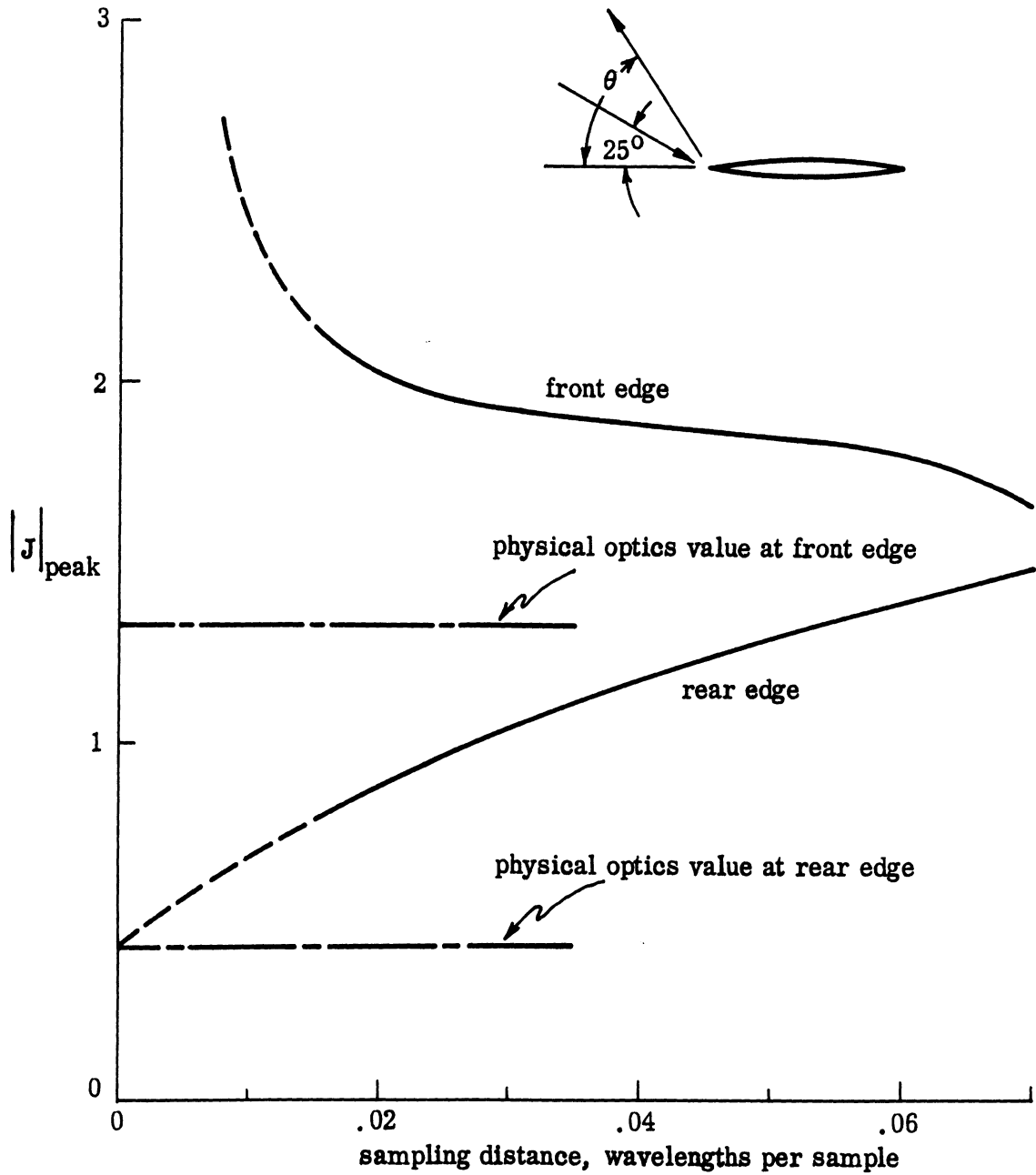


FIG. 3-8: Influence of sampling rate on peak edge currents.

between sample points in the vicinity of the edge. The peak value of the rear edge current decreases steadily as the sampling becomes more dense and, as suggested by the dashed line, an extrapolation of the behavior to the limit of zero sampling distance pegs the current at its physical optics value. This plot clearly shows that if we seek to get within, say, 10 percent of the physical optics value at the rear edge, the sampling distance must be of the order of 0.0015 wavelength, implying a packing density of 670 points per wavelength! The behavior of the front edge current is not so easy to predict, since the front edge currents theoretically rise to infinity.

Unfortunately, even the densest packing used in this sequence of tests was less than half that of the smallest radius used to blunt the ogival cylinder ends and the agreement in the bistatic scattering with GTD was poorer than the worst case depicted in Fig. 3-7. We concluded that a combination of small radius of curvature and dense sampling was the only way to improve the far field predictions of RAM1B any further and we subsequently devised another test.

We chose an edge radius of only 0.0131λ and placed 8 sampling points there, producing a surface sampling distance of 0.0045λ (i.e., sampling rate of 224 points per wavelength). In order to increase the sampling interval gradually from this tiny value to a much coarser one near the center of the ogival cylinder, each interval was made 50 percent longer than the previous one as the surface was sampled progressively farther away from the edge. When the interval grew as large as 0.095λ (about 10 samples per wavelength), it was then held fixed until the remainder of the cylinder had been covered.

The results of this sampling method are shown in Figure 3-9 along with the GTD standard for comparison. Note that the disagreement is no worse than 2.0dB, and is an improvement, though modest, over that produced by the rounding used to

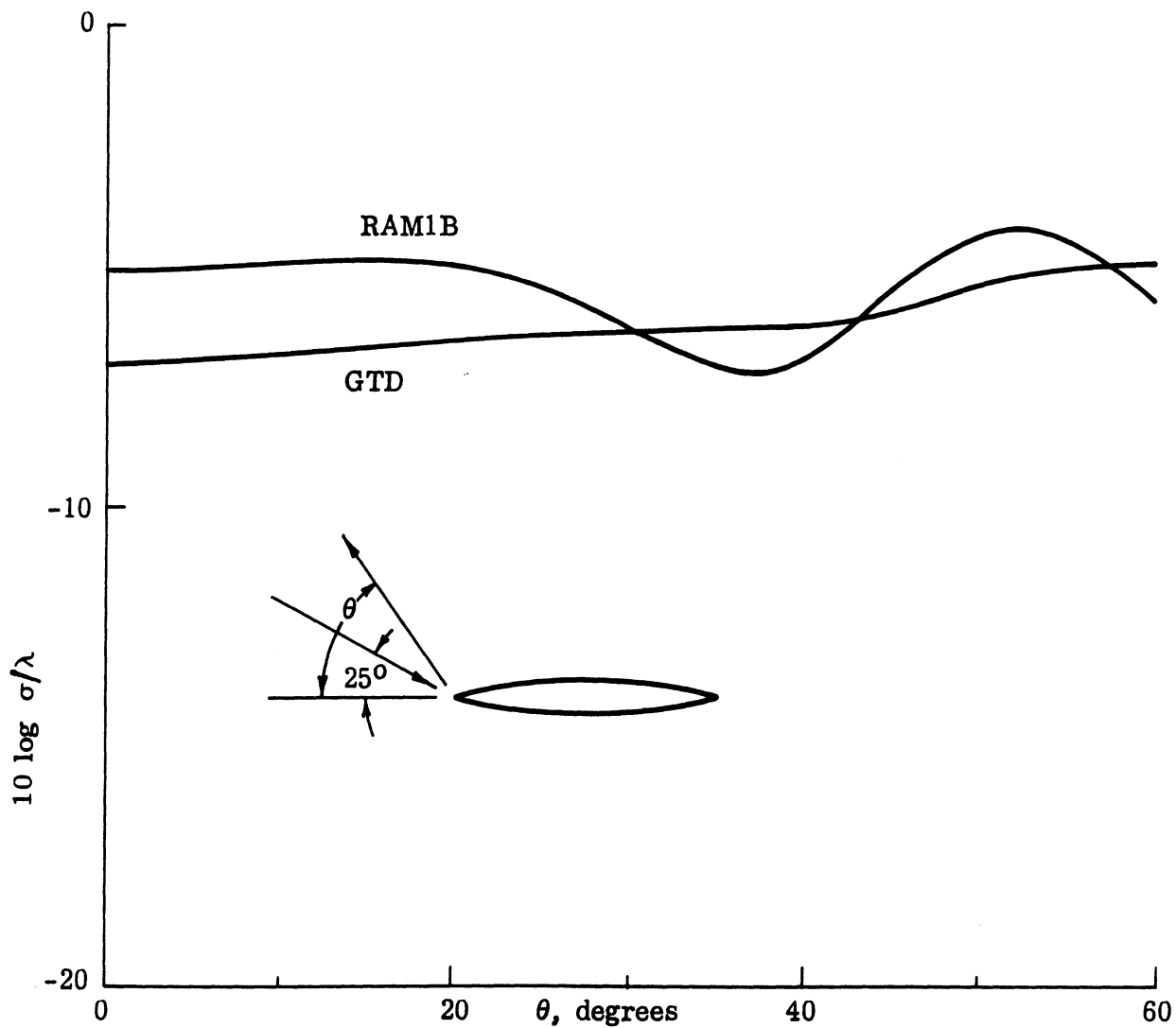


FIG. 3-9: Comparison of bistatic scattered field from ogival cylinder with dense sampling at the edges.

obtain the patterns in Fig. 3-7. Further testing is planned in which the rear edge will be loaded in an effort to suppress the rear edge currents. The purpose will be to try to obtain the correct 'bare body' scattering and the loading will not be for the purposes of cross section reduction. Since any passive rear edge surface impedance for E-polarization tends to convert the scattering to an H-type (rear edge) contribution, we may be forced to use impedances with negative real parts. Such loads are sources but, since it is the true scattering from metallic object that is being synthesized, the means by which this is done is not important.

3.3 Program RAMC

We received a source deck and sample output of program RAMC in October, 1972 but for the time being the program was set aside while we tried to get RAM1B working satisfactorily for edged structures. It became apparent in late November that it might require artificial treatment of the rear edge of the ogival cylinder in order to suppress the spurious currents generated there by RAM1B for E-polarization and that we ought to have on hand a back-up program in the event that RAM1B fell short of our expectations. In addition, RAMC promised to simulate a realistic situation more faithfully than RAM1B, in that the properties of a resistive sheet are specified, rather than the more nebulous surface impedance boundary condition. The program handles only E-polarization, but this is precisely the case that required attention.

RAMC had been designed for a specific application and had to be modified. In its original form, RAMC had but two options: it either generated the profiles of a conducting, circular cylindrical core surrounded by a concentric resistive sheet or it accepted profile coordinates, specified point-by-point by the user, of an arbitrary conducting core, also surrounded by a resistive sheet. Although the sheet resistance must be specified in both cases, RAMC assumed a constant value of resistance over the entire sheet.

These conditions were far too restrictive for our needs because we can conceive of the need to place isolated resistive segments at arbitrary positions in space near, but not necessarily in contact with, a conducting body. Furthermore, the properties of the sheet must certainly be variable with position along the sheet, and we set about to modify the program.

As was done for RAM1B, we provided for the construction of arbitrary profiles that are describable in terms of a finite collection of circular arcs and straight line segments. The user need only specify the coordinates of the endpoints of the segments along with the resistance variation required and the program sets up the geometrical profile. Unlike previous profile-generating routines, the modified program does not require that the user specify in advance the number of sampling points or the number of segments on the body; the program performs this book-keeping chore itself.

The modified program is called REST and a listing and short description of it are given in Appendix B. Initial tests of REST on the same body used for the sample run performed at AFAL showed that it duplicated the original program, which was encouraging. But when tested on other bodies, REST failed by a wide margin to reproduce either the known results for a metallic cylinder ($ka=5$) or the results obtained from RAM1B on a fat strip.

At first it appeared that the matrix inversion subroutine was at fault, since we could not get agreement with standard routines such as that found in IBM's Scientific Subroutine Package. We then "borrowed" the inversion subroutine ZVO8 from RAM1B, which had been previously demonstrated as workable, but the surface currents and far field scattering remained unacceptable. In the meantime, a copy of a similar program modified by Teledyne Ryan Aeronautical had been acquired in the event that REST would require too much time to debug.

Very recently, as a result of more probing of program REST, we discovered that subroutine HANK fails by progressively wider margins to compute the Hankel

functions necessary to construct the matrix elements. REST produced acceptable results for small cylinders but not larger ones, because, with single precision arithmetic (IBM's 32-bit word length), HANK is virtually useless for arguments greater than (about) 8.0. We rewrote the subroutine in double precision arithmetic for further testing on the IBM 360/67 (with 64-bit words) and the subroutine now works well for arguments as large as 35.0. A subsequent test on the CDC 6600 using the single precision version, implying 60-bit word lengths, showed good agreement with the IBM double precision program, but both programs fail for arguments greater than 35. This implies that bodies can have maximum dimensions no greater than (about) 5.5 wavelengths, at least if this version of HANK is employed. On the other hand, such a body would require at least 100 sampling points, which is near the capacity of the CDC 6600 without going to external storage. Thus HANK in its current form is deemed adequate for the task at hand.

IV. EXPERIMENTAL WORK

Throughout much of this contract we have relied on program RAM1B to provide basic information about the influence of surface impedance on both the surface and far scattered fields of non-specular scatterers. Because the program was a new tool, at least to us, we subjected it to several kinds of tests to determine its capabilities. As pointed out in Chapter III, one of these tests was a comparison of RAM1B's predictions against those of GTD and the results of the tests were that special techniques (e.g., variable surface sampling rates) are required in certain specific instances of geometry and illumination. Thus the utility of having a separate and independent means of checking the program cannot be over emphasized.

Although GTD served as a useful gauge for conducting bodies, there are far fewer cases in which a gauge exists for imperfectly conducting surfaces. An exact solution of the boundary value problem exists, but only for simple shapes such as the circular cylinder and the sphere and even then the coatings that are treatable must be uniform. For the specific cases of the ogival cylinder and the wedge-cylinder, no exact solutions are available for either the bare or uniformly coated bodies. Thus, for the want of any theoretical checks of program RAM1B for cases of absorber coated bodies, we turned to experiment. In addition to serving as a check on the program, we also expect that the experimental data will prove valuable in helping us to make the critical translation from the abstract concept of surface impedance to the more realistic specification of necessary material properties.

An ogival cylinder and a rectangular flat plate were constructed for use in the experiment and both the surface and backscattered fields for each were measured. These objects were bare at first and, after the data had been collected, they were coated with a magnetic absorber and the measurements repeated. The tangential component of the magnetic surface field was measured on the bare cylinder and both the tangential magnetic and electric surface fields were measured on the coated objects.

4.1 Experimental Models

Since much more data had been generated for the ogival cylinder than the wedge-cylinder by RAM1B, we chose this as the shape to be modeled in the laboratory. We settled on 3.0 GHz as a test frequency because this would translate the edge-to-edge cylinder width of 3.0λ used in the program to 11.7 inches, a distance comfortably covered by the nominal 12-inch size of the absorber sheets purchased from Emerson and Cuming, Inc. The ogival cylinder model was constructed with ribs and spars, much like wings of model airplanes. Four ribs were cut from a softwood board to the required ogival shape and a hole was drilled near each end. The ribs were then slipped onto a pair of birch dowels (the 'spars') and were spaced uniformly along the length of the dowels. Thin aluminum sheets were wrapped over the top and bottom sides of the framework and, because the sheets tended to spring apart where they met at the edge, metallized tape was used to hold them together there. The finished product was 35 inches long, 11.7 inches wide and 1.38 inches thick, as sketched in the upper diagram of Fig. 4-1.

This method of construction did not produce perfect knife edges but, as the lower diagram of Fig. 4-1 shows, the radius of curvature of the edge is small, being an estimated 0.02 inch, which is 0.005λ at 3.0 GHz. The magnetic material applied later was Emerson and Cuming Eccosorb SFT-2.5, nominally 0.09 inch thick, and extended slightly beyond the edge producing the overlap shown in the figure. The result of this overlap was to create a very narrow face of absorber running the length of the edge. Samples of the material were submitted to AFAL for measurement of electrical properties on its pulsed system and the nominal results at 3.0 GHz are, assuming $e^{i\omega t}$ time convention,

$$\begin{aligned}\epsilon_r &= 24 - i 3.0, \\ \mu_r &= 4.2 - i 3.2.\end{aligned}$$

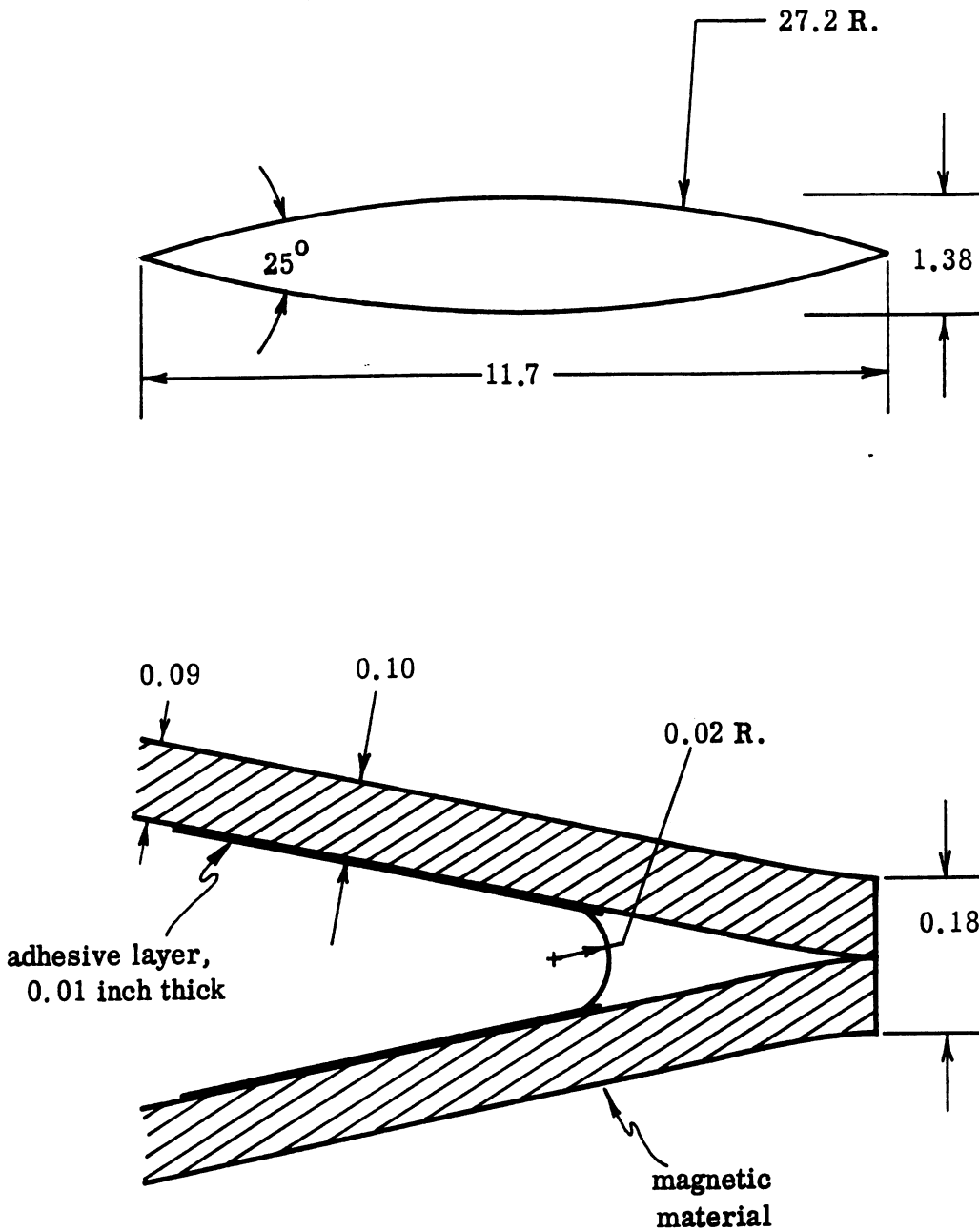


FIG. 4-1: Dimensions of the experimental ogival-cylinder are given in inches; the lower diagram shows a finite edge radius and the overlapping of the coating beyond the edge.

In addition to the ogival cylinder, we constructed a rectangular flat plate 12.1 by 11.06 inches (dictated by the size of stock available at the time) and mounted a layer of the SF material on one side of it. The absorber was not trimmed to the exact size of the plate but instead was permitted to project slightly beyond the edges to minimize edge diffraction.

4.2 Backscatter Measurements

The radar cross sections of the bare and coated models were measured in the Radiation Laboratory anechoic chamber at Willow Run Airport. A conventional CW cancellation method of measurement was used, in which the residual chamber reflections are tuned out in the absence of the scatterer. The cylinder measurements were performed in two steps (because of the necessity of sandwiching surface field measurements between separate measurements of the radar cross section), whereas the coated flat plate was measured but once. Since one side of the plate was bare, a single pattern served to establish the reflectivity of the coated surface.

The cylinder was measured at a range of 25 feet, which is slightly more than half the standard $2D^2/\lambda$ criterion recommended for most backscatter measurements. This was necessary because of sensitivity limitations but for the purposes for which the data would be acquired, the shortened range is not felt to be injurious.

Since the main scattering lobe from a body 9λ long is only 5.2 degrees wide (null-to-null) a misalignment of 0.9 degree can introduce a 3dB error. To serve as a check on the measurements made in the transverse plane perpendicular to the cylinder axis, we first took some preliminary patterns in a longitudinal plane normal to the large curved surface. These patterns are not presented but they did provide us with an absolute amplitude which the transverse patterns should attain when the broad surface is viewed at normal incidence.

The transverse plane patterns of the bare and coated ogival cylinder appear in Figs. 4-2 through 4-5 for both E- and H-polarizations. The broadside returns of the bare body patterns in Figs. 4-2 and 4-3 attain values of 34.8 and 36.3 $\text{dB}\lambda^2$ for E- and H-polarization respectively, the mean value being very close to the physical optics prediction of 35.36 $\text{dB}\lambda^2$. The E-polarized pattern is relatively flat in the edge-on region, consistent with the GTD prediction that the front edge is the sole contributor, while the H-polarized pattern exhibits a great deal of lobe structure, commonly attributed to traveling wave echoes. At precisely edge-on incidence the nulls of the H-polarized pattern fell off the chart paper, but by increasing the system gain we were able to record a small segment of the pattern; the apparent edge-on amplitude is $-2.5 \text{ dB}\lambda^2$. Since the rear edge is hidden from view at this aspect, GTD would properly include only the H-polarized front edge return which, when corrected by the three-dimensional to two-dimensional conversion formula given in Appendix C, would be $-3.90 \text{ dB}\lambda^2$. Thus, even for this very small return, experiment and GTD agree within 1.5 dB.

Because of the difficulties noted in Chapter III for E-polarization, program RAM1B was not used to generate an E-polarized pattern to compare with Fig. 4-2, but we did use it to obtain computed results for H-polarization, shown as the dashed line in Fig. 4-3. Aside from a consistent displacement in amplitude, the computed pattern replicates the measured one quite well. The program output is given in terms of $10 \log \sigma/\lambda$ for a true two-dimensional object and must therefore be corrected via the conversion factor $2(L/\lambda)^2$ (derived in Appendix C) in order to be compared with the three-dimensional object measured in Fig. 4-3. For the body dimensions and frequency used in the experiment, this constant works out to be 22.0 dB.

Since the cylinder was measured at about half the normal distance required of far field measurements, there is a distinct possibility that the foreshortening produced the amplitude disparity observable in the Figure, although it is hard to believe that this would produce an error as large as 2 dB. It is more likely that the cylinder axis was tilted slightly away from the vertical during the measurements, thus swinging the transverse plane response off the peak of the main lobe in the longitudinal plane. In addition to the differences in amplitude, there is a slight but distinct shift in the positions of lobes and nulls, which is characteristic of measurements made at less than the nominal far zone distance of $2L^2/\lambda$. In spite of these disparities, the correlation between the measured and computed patterns is a gratifying demonstration of the capability of the computer program. The far field predictions are based, of course, upon the currents induced on the body's surface by the incident wave, and we shall compare measured and predicted surface currents in a moment.

Coating the cylinder produces a substantial cross section reduction throughout most of the patterns, as evidence in Figures 4-4 and 4-5. At broadside the reduction amounts to 12.8 dB for H-polarization and 14.0 dB for E-polarization, both of which slightly exceed the nominal 15 dB quoted by the manufacturer for SFT-2.5 when used at 3.0 GHz. The edge-on reduction for E-polarization exceeds that of the broadside return while for H-polarization, due to the null in the bare body pattern at edge-on, there is a cross section enhancement that persists for 10 degrees either side of the plane of symmetry. Although this was unexpected—we anticipated better performance for H- than for E-polarization—we are gratified to find a net reduction in the edge-on region that is comparable with the specular cross section reduction.

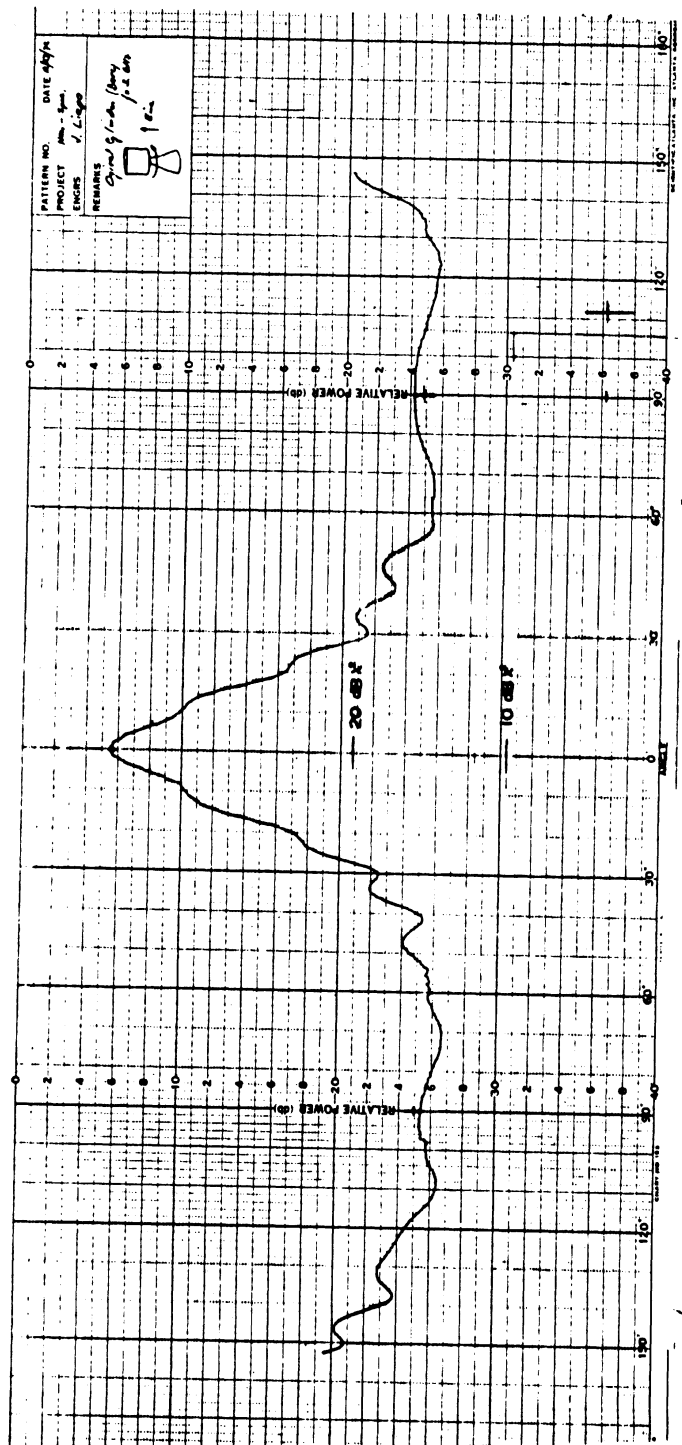


FIG. 4-2: Backscattering from bare ogival cylinder, E-polarization.

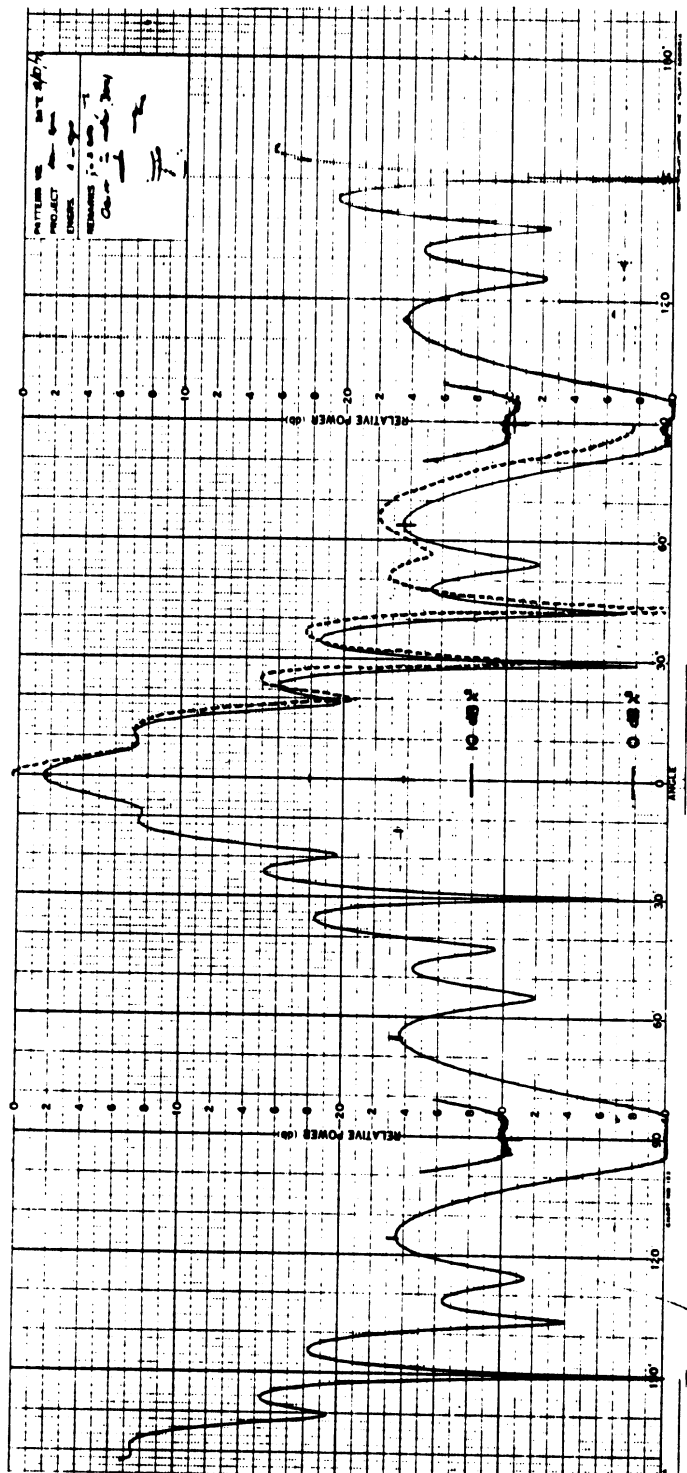


FIG. 4-3: Backscattering from bare ogival cylinder, H-polarization. The dashed trace was obtained using program RAM1B.

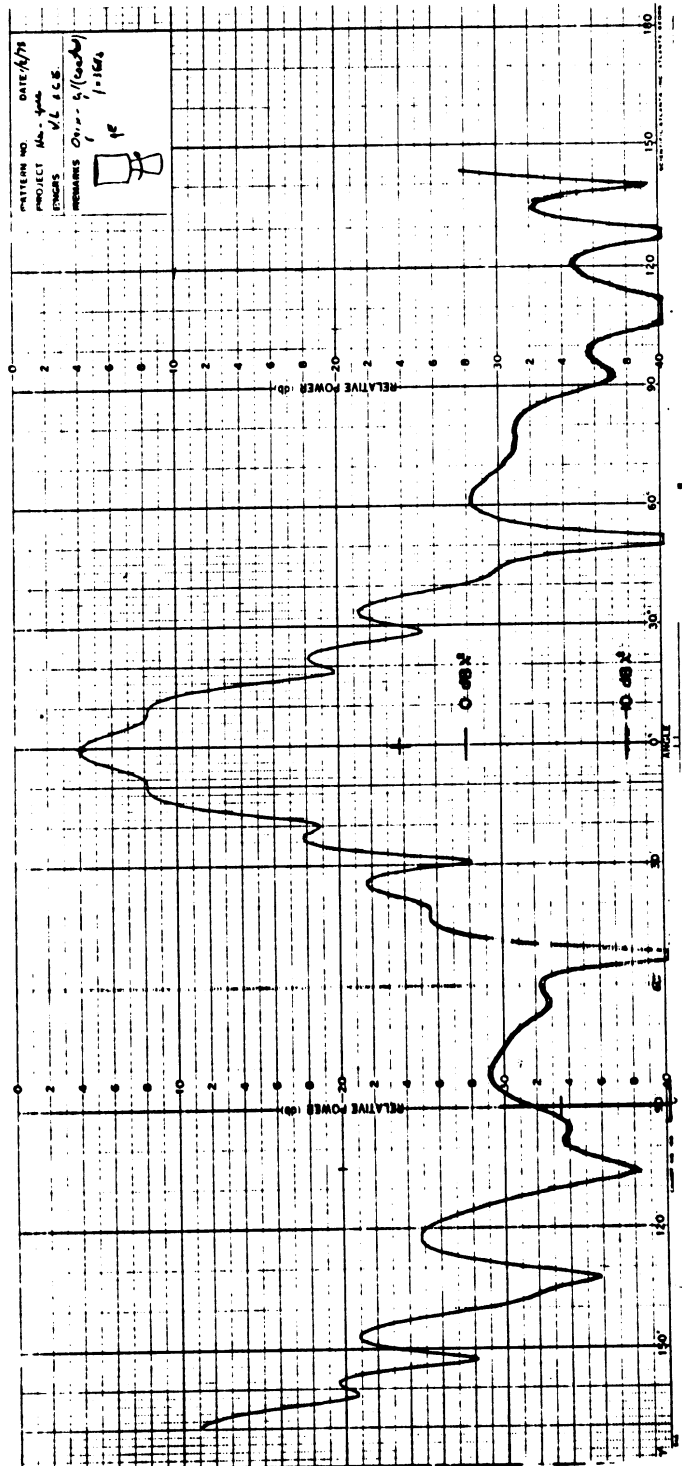


FIG. 4-4: Backscattering from coated ogival cylinder, E-polarization.

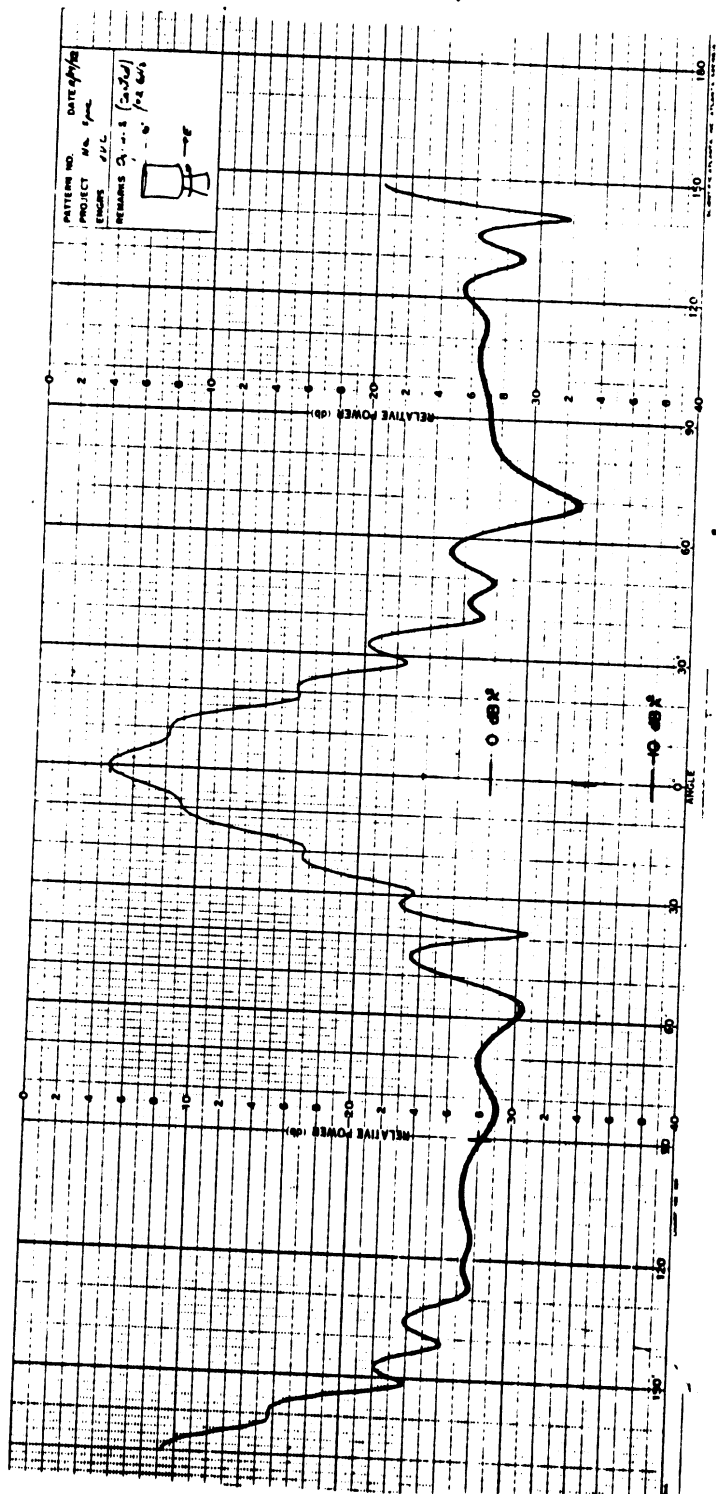


FIG. 4-5: Backscattering from coated ogival cylinder, H-polarization.

Because of its smaller size, the flat plate was much easier to measure than the ogival cylinder. The plate was rotated a full 360 degrees and the difference between the bare and coated normal incidence returns was 12.1dB, giving a voltage reflection coefficient of 0.249, a value slightly larger than measured for the ogival cylinder. The physical optics broadside echo from the conducting plate is $29.7\text{dB}\lambda^2$ while the measured value was $28.8\text{dB}\lambda^2$, 0.9dB smaller.

4.3 Surface Field Measurements

The fields induced on the surfaces of the two laboratory models were measured in a facility designed expressly for the purpose of near field probing (Knott, et al, 1965). The facility consists of a tapered anechoic chamber approximately 44 feet long, probe traversing machinery and RF signal generating and detection equipment. The tapered end of the chamber is the transmitting end and the source of illumination is typically a horn placed at the apex. The receiving end of the chamber is rectilinear, being about 11 by 12 by 10 feet in size, and centered above the volume normally occupied by the test object is a square hole in the ceiling 2 feet on a side. Mounted on the top side of the ceiling is the probe traversing machinery and projecting downward through the hole is a lightweight support structure that carries a slender probe into the test volume. The traversing equipment is driven by small dc motors that are controlled remotely by an operator from within the chamber or from an equipment room just outside the chamber.

A block diagram of the system is given in Fig. 4-6. The transmitting equipment consists of an rf source, typically a klystron, driving a TWT amplifier and stabilized in frequency by a phase-locking detector. The sensing and receiving equipment consists of small loop or dipole probes and a superheterodyne detector which displays the amplitude and phase of the received signal (Hewlett-Packard Network Analyzer, Model 8410). Since absolute phase depends on the characteristics of the probes used, the system indicates only relative phase which, as we shall see in a moment, must be calibrated in a separate measurement.

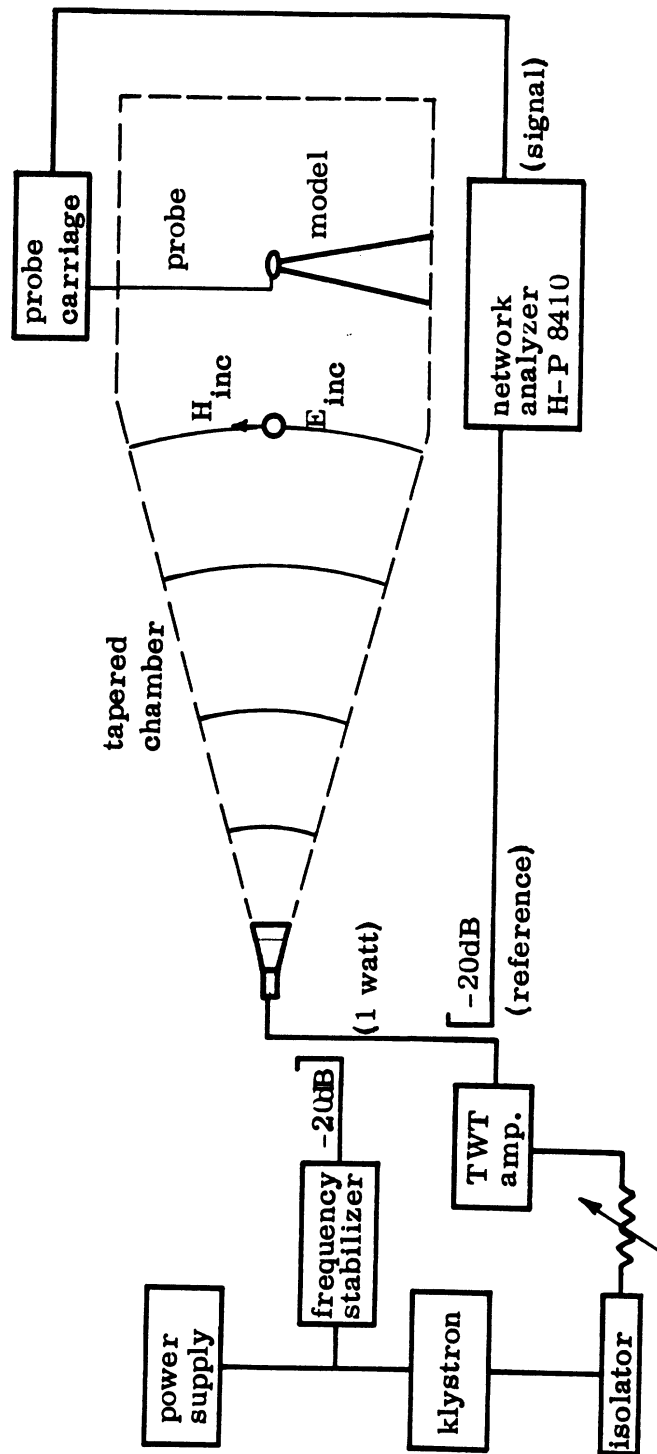


FIG. 4-6: Block diagram of equipment and facility used for surface field measurements.

Two magnetic loop probes and one balanced electric dipole were used to measure the surface fields. A single electric probe was sufficient because the electric field was always horizontally polarized (to minimize interactions with the probe lead) but depending on the relative orientation of the surface being probed, we needed magnetic probes that sensed either vertical or horizontal magnetic fields. Since the probe leads descend vertically into the chamber, a magnetic loop probe sampling the vertical component must have a right-angle bend near the loop in order to bring the loop into a horizontal plane. The form of this probe is much like that of the wire frame used to dye eggs at Easter time. A probe sensing the horizontal component of magnetic field has no such bend and its shape is similar to the frame of a tennis racket. The electric probe was a balanced dipole with each arm fed by a separate coaxial lead. The two signals were combined, with a line stretcher inserted in one lead for phase adjustment, in a hybrid tee and the net signal was then detected and displayed.

It is necessary to measure the tangential components of both the electric and magnetic surface fields in order to determine surface impedance, but since the characteristics of electric and magnetic probes are vastly different, both probes must be calibrated. Conceptually this can be done quite simply by exposing the probe to the incident field at some fixed point in space in the absence of the test obstacle, but in practice this can be difficult because the probe position is not easily measured in the absence of the test object. The residual chamber reflections are small enough that amplitude is sensibly independent of probe position and can therefore be easily determined, but absolute phase, being strongly position dependent, could only be calibrated for the (relatively) small flat plate. Since the plate was small and light, it could be carefully brought up to the probe without disturbing the probe position, and hence measurements with and without the plate in position were

obtained for calibration. But because the ogival cylinder was heavy and bulky, we could not install it in (nor indeed remove it from) the test volume without nudging the probe. Thus the phase data acquired for the cylinder include an undetermined (but constant) phase angle.

All surface field measurements of the ogival cylinder were carried out for incidence normal to the cylinder axis and 25 degrees out of the plane of symmetry passing through the leading and trailing edges. For H-polarized incidence, the cylinder was placed on one of its ends and then turned 25 degrees in azimuth away from the illuminating horn; for E-polarization it was placed horizontally atop a styrofoam column normal to the direction of incidence and tilted downward 25 degrees, simulating a negative angle of attack. Along a chord midway between the cylinder ends a scale was penciled on the surface so that a probe could be stationed at 1 cm intervals along a path from the leading to trailing edge.

The amplitude and phase of tangential magnetic field on the bare cylinder (i.e., the surface currents) are plotted in Fig. 4-7 for H-polarization. The H-polarized currents are small near the leading edge but rise to their physical optics value within a wavelength or so. The superposed oscillation due to reflections from the trailing edge has a period of about $\lambda/2$ and increases in amplitude toward the rear edge, thus confirming the notion that a rear edge reflection combines with a forward traveling wave to produce a standing wave pattern. Because of the built-in time convention of the detection equipment, the phase of the surface currents steadily decrease from front to trailing edge, implying a time convention $e^{i\omega t}$. The reader should be aware that the time convention used in all other chapters in this report is $e^{-i\omega t}$. The straight line plotted in Fig. 4-7 is the relative phase of the incident field alone and we note that the phase behavior of the surface field is virtually identical to that of the incident field. For comparison we have plotted the surface current amplitude predicted by program RAM1B as a dashed line; note that the agreement with experiment is quite good.

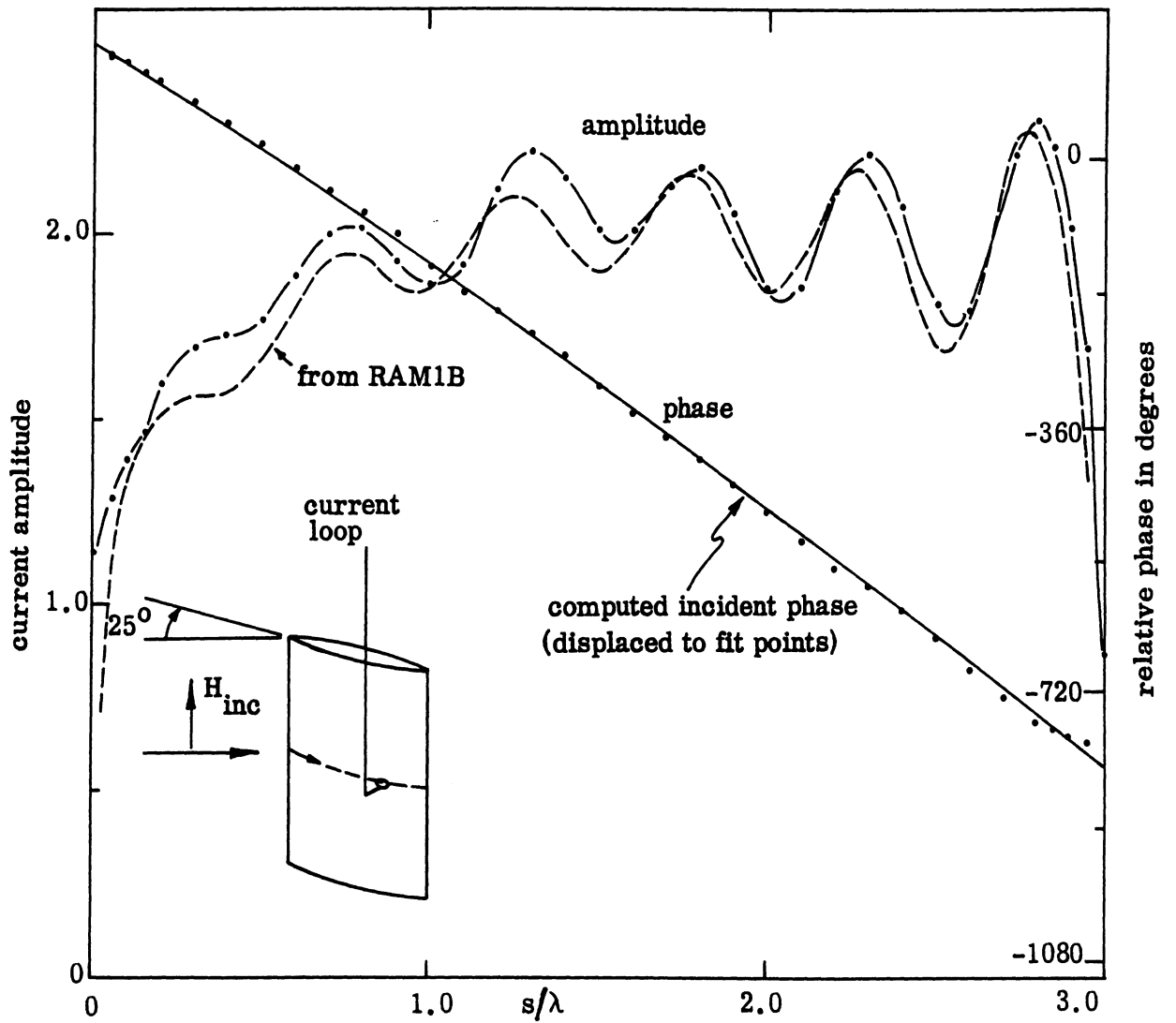


FIG. 4-7: Measured current and phase on bare ogival cylinder, H-polarization. The dashed line is the behavior predicted by program RAM1B.

E-polarized surface field measurements of the bare cylinder are summarized in Fig. 4-8. In contrast with H-polarization, the leading edge currents are large and at first decay rapidly with distance away from the edge, then at a more gentle rate. A slight peak occurs at the rear edge and the oscillations superposed on the mean behavior betray a reflection from somewhere, but their period (about $.7\lambda$) suggests a more complex interaction than occurs for H-polarization. Aside from a net displacement when compared with Fig. 4-7, the phase behavior is virtually identical and matches that of the incident field.

When the cylinder is coated, the electric as well as the magnetic surface field can be measured and the resulting amplitude and phase data are displayed separately in Figs. 4-9 and 4-10 for H-polarization. Because the application of absorber creates a new surface slightly longer than that of the uncoated cylinder, the new surface coordinates are not precisely aligned with those of Figs. 4-7 and 4-8. The amplitude of the tangential magnetic field (Fig. 4-9) is much lower than that of the bare object and the oscillations due to the rear edge reflection have virtually disappeared. Note, however, that the field increases toward the leading edge and in this respect resembles the behavior for the other (E-) polarization. This explains, in part, why the H-polarized backscattering described earlier increased over a range of aspect angles centered at edge-on after the absorbent coating had been applied to the cylinder and is also consistent with the notion that a surface impedance at an edge tends to convert E-polarization characteristics into H-polarized, and vice versa, as pointed out in our last report. The tangential electric field is stronger than the magnetic field and exhibits irregular fluctuations about its mean level, as shown in Fig. 4-10, but the phase is remarkably steady. We suspect that the total tangential field is changing very rapidly near the surface and, since the small but finite insulation on the exposed dipole arms prevents the probe from fully contacting the surface, errors may result.

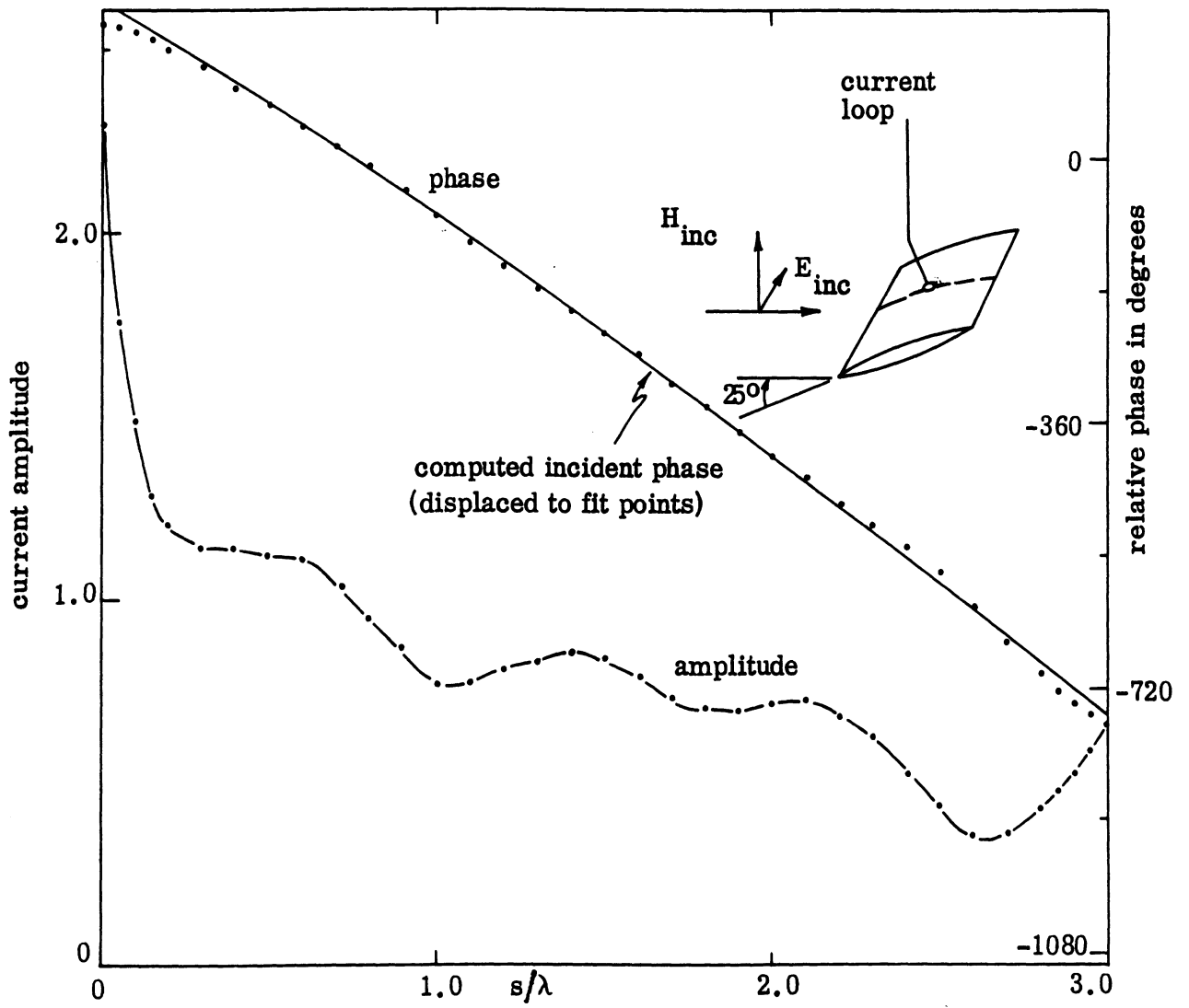


FIG. 4-8: Measured current and phase on the bare ogival cylinder, E-polarization.

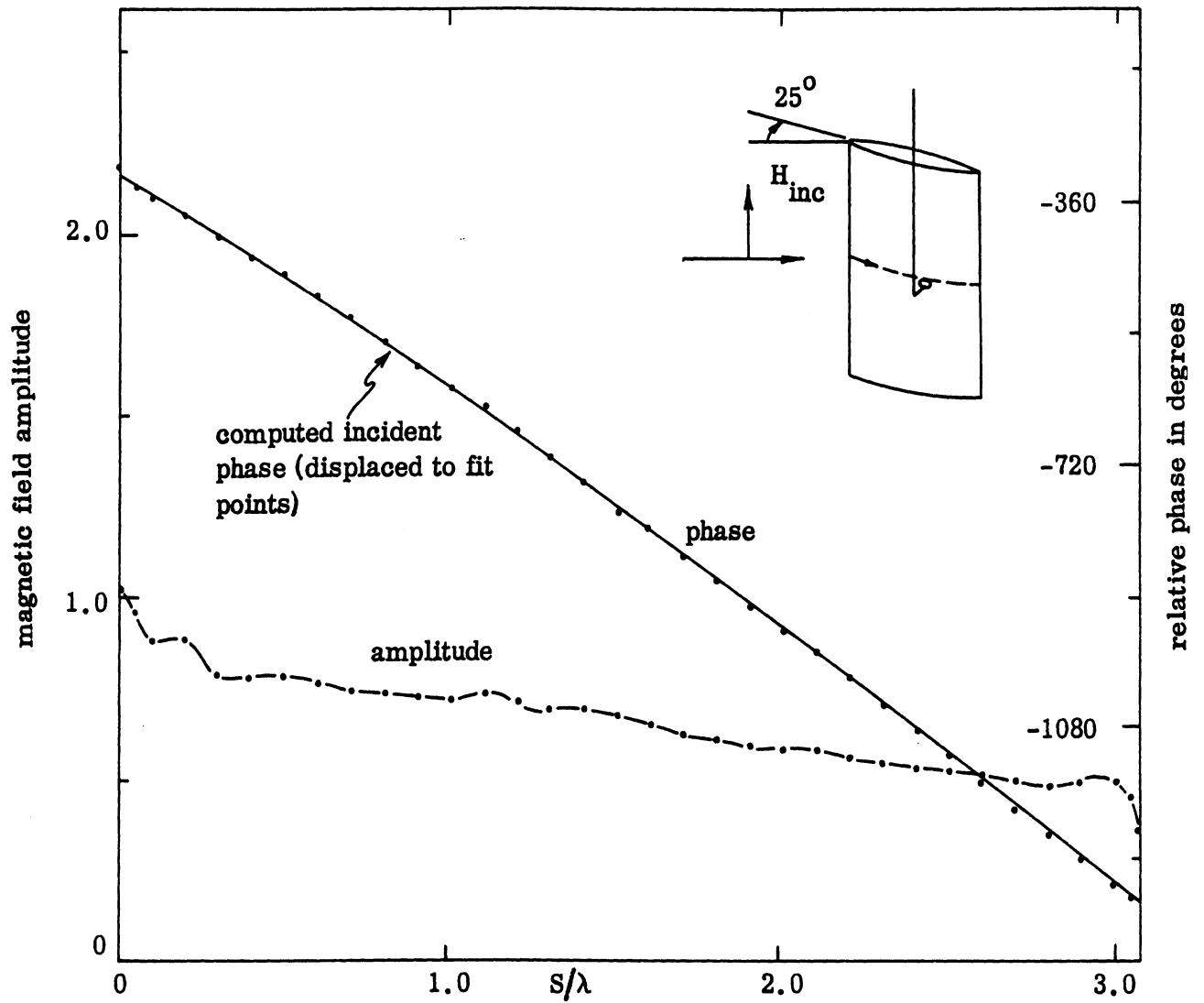


FIG. 4-9: Measured magnetic field and its phase on coated ogival cylinder, H-polarization.

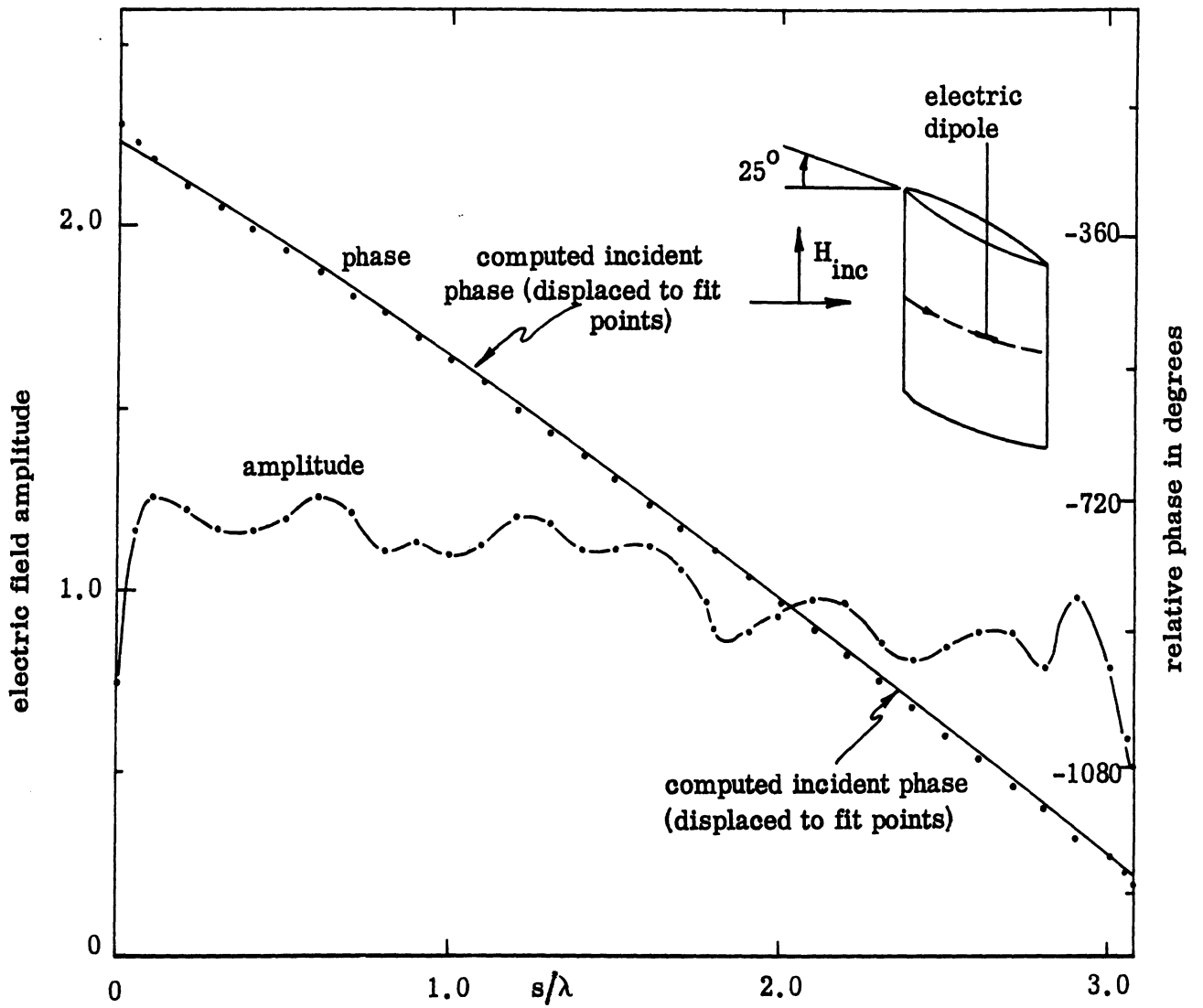


FIG. 4-10: Measured electric field and its phase on the coated ogival cylinder, H-polarization.

The surface field measurements for E-polarization are plotted in Figs. 4-11 and 4-12, again the amplitude and phase appearing separately. As with the H-polarized measurements, the application of the absorber coating tends to reverse the character of the currents near the edge. Note that for this polarization the magnetic field strength is not as uniform as for H-polarization and that the electric field intensity is somewhat lower. The phase data closely match that of the incident field, which has been characteristic of all the surface fields measured. These data, and those of Figs. 4-9 and 4-10, were used to estimate the variation of the surface impedance across the face of the cylinder and will be included in the discussion and analyses presented in Chapter V.

A final set of surface field data was collected for the coated flat plate, with the coated side presented normal to the direction of incidence. As mentioned a moment ago, we were able to install and remove the plate without disturbing the probe and this permitted us to calibrate the phase of the incident field as well as the amplitude. In order to obtain a realistic figure for the surface impedance, we completed horizontal and vertical scans across the face of the coated plate with both the electric and magnetic probes. The amplitude showed no more than a ± 0.25 dB excursion and the phase remained constant within ± 3 degrees for the magnetic field and ± 0.5 dB and ± 3 degrees for the electric field. A summary of the flat plate measurements is given in Table 4-1, and note that a normalized impedance of $1.495 \angle -43^\circ$ would be inferred from the data.

A voltage reflection coefficient can be deduced for the coated plate surface in terms of the measured surface impedance via the formula

$$\Gamma = (Z_s - 1) / (Z_s + 1) .$$

Using the value $Z_s = 1.0934 - i 1.0196 = 1.495 \angle -43^\circ$, we obtain a voltage reflection coefficient of $|\Gamma| = 0.4397$, implying a power reflection of -7.15 dB. This is

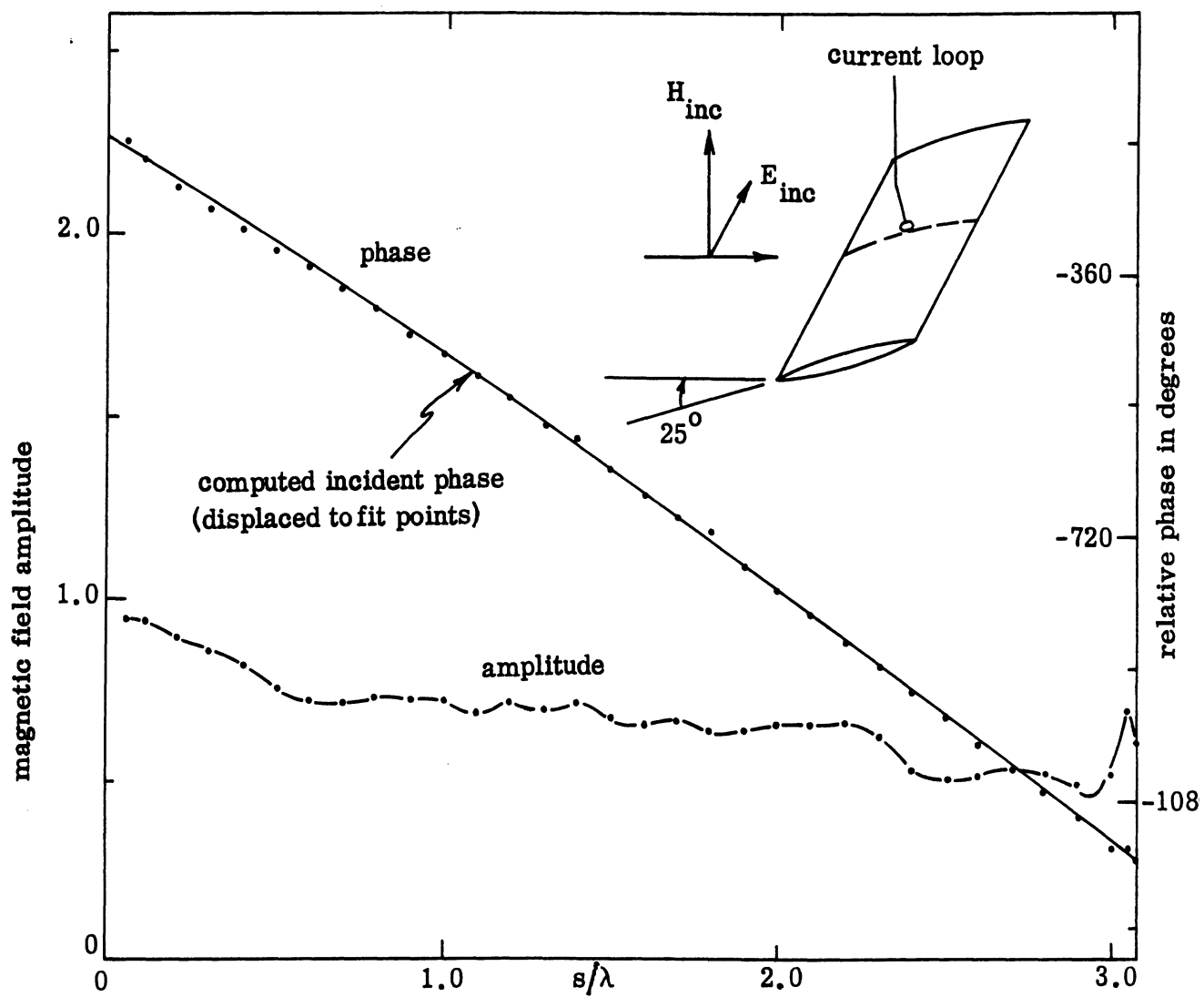


FIG. 4-11: Measured magnetic field and its phase on the coated ogival cylinder, E-polarization.

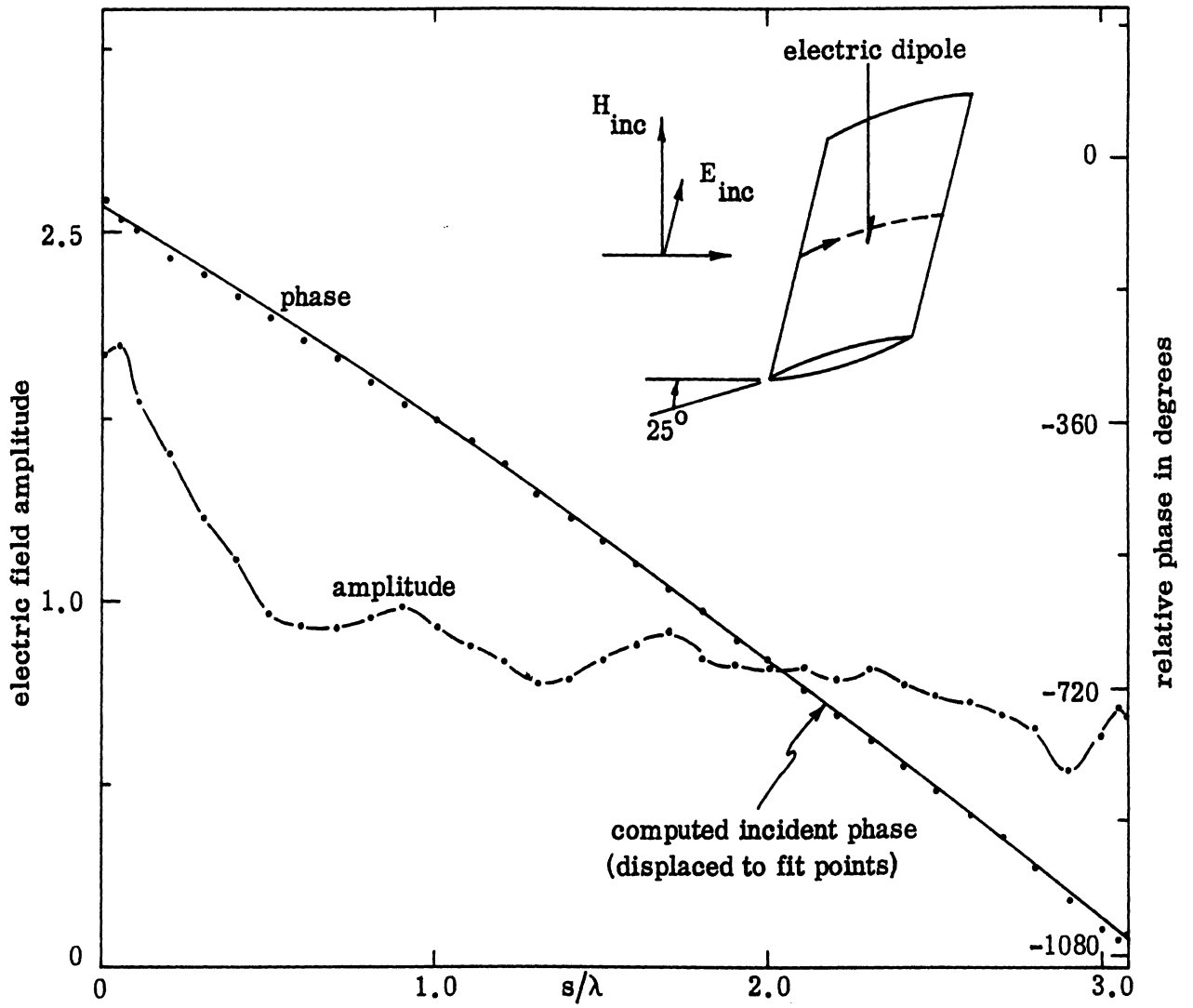


FIG. 4-12: Measured electric field and its phase on the coated ogival cylinder, E-polarization.

substantially higher than -12 to -14dB measured in the far field for the flat plate and ogival cylinder cross section reductions and the source of the discrepancy will be examined in the following chapter.

Field quantity	E / ϕ or $20 \log E / \phi$	H / ϕ or $20 \log H / \phi$
Free space probe response	-21.4 $\angle -34^\circ$	-36.5 $\angle -123^\circ$
Mean probe indication at plate surface	-17.45 $\angle -64^\circ$	-36.05 $\angle -110^\circ$
Normalized field strength	1.575 $\angle -30^\circ$	1.053 $\angle 13^\circ$

Table 4-1: Summary of flat plate measurements.

V. SURFACE IMPEDANCE STUDIES

One of the main objectives of the measurement program described in the preceding chapter was to determine the surface impedance which a homogeneous coating actually presents under circumstances of interest under this contract. As we pointed out in our previous report (Knott and Senior, 1973, Chapter III), it is theoretically impossible to relate this impedance to the electrical properties of the coating in a manner which is valid for all surfaces independently of the fields which are present. A simple relation (the so-called layer formula) does exist in the particular case of an infinite flat surface illuminated by a plane wave, but under more general circumstances it is expected that both the geometry and the surface field (which are themselves interconnected quantities) will affect the impedance which even a homogeneous layer presents. If we are to succeed in translating the "optimum" surface impedances deduced from the computer programs RAM1B, etc., into specifications of material constants, it is necessary to have some feeling for the magnitude of the above effect.

From the measurements of the tangential electric and magnetic fields on a single panel of the Emerson and Cuming material when backed by a metal and illuminated by a plane wave at normal incidence, the normalized surface impedance $\eta = Z_s/Z_0$ initially obtained was*

$$\eta = 1.495 e^{i43^\circ} \quad (5.1)$$

When the material was applied to the ogival cylinder, the surface impedances deduced from the measured surface field data are as shown in Fig. 5-1 and 5-2 for E- and H-polarizations respectively. Observe that in each case the phase is relative to a fixed but unknown value. Both the phase and amplitude curves have noticeable oscillations whose dominant period is compatible with the forward and backward waves constituting the surface field. As the front edge is approached, the impedance increases for E-polarization, but decreases for H-polarization. These changes are confined to a distance of $\lambda/2$ from the edge, and this is the region where edge effects are

* We have now reverted to the $e^{-i\omega t}$ time convention standard in our work.

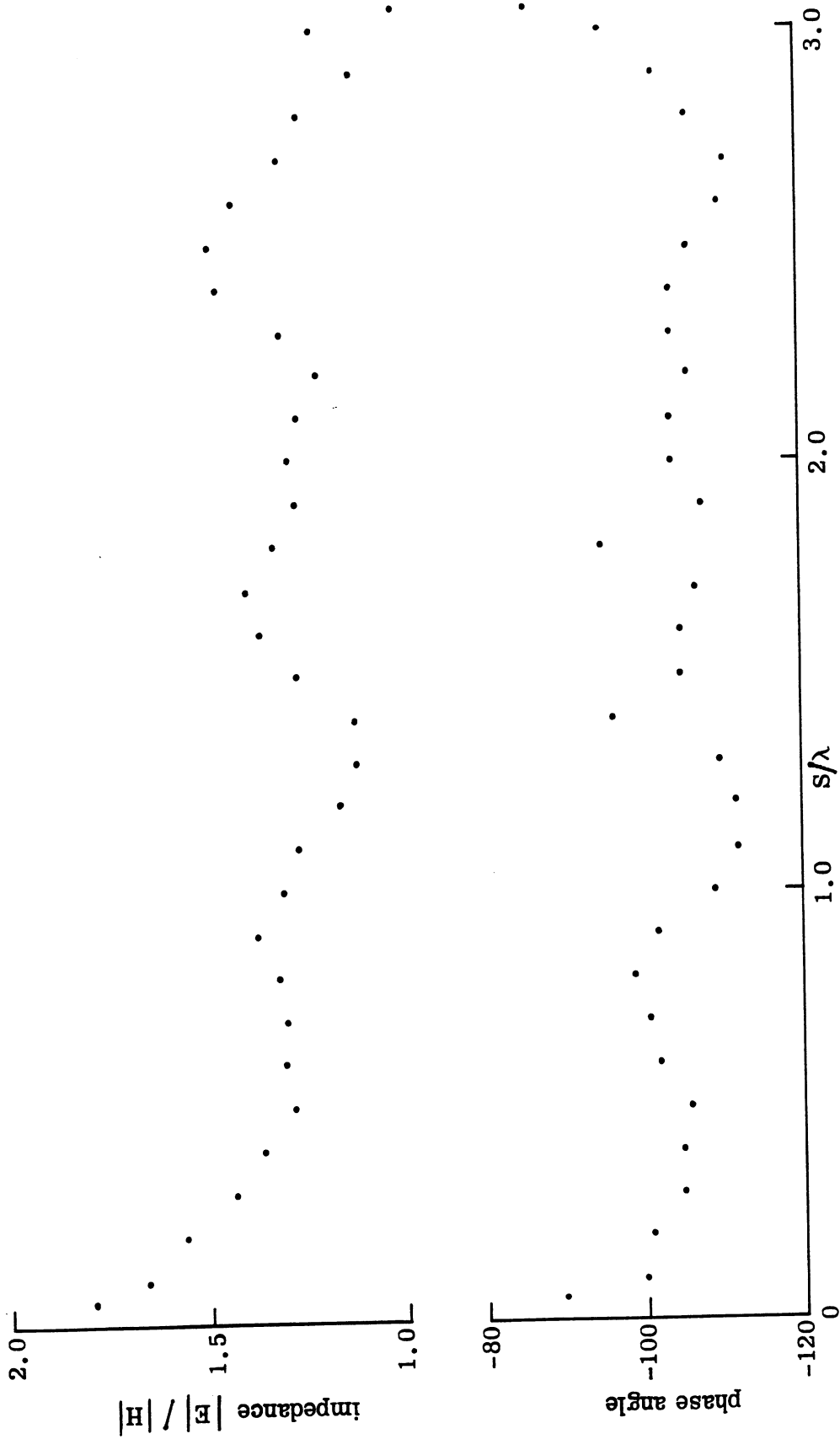


FIG. 5-1-1: Deduced amplitude and phase of surface impedance for E-polarization. The phase is relative to an arbitrary value ϕ'_0 .

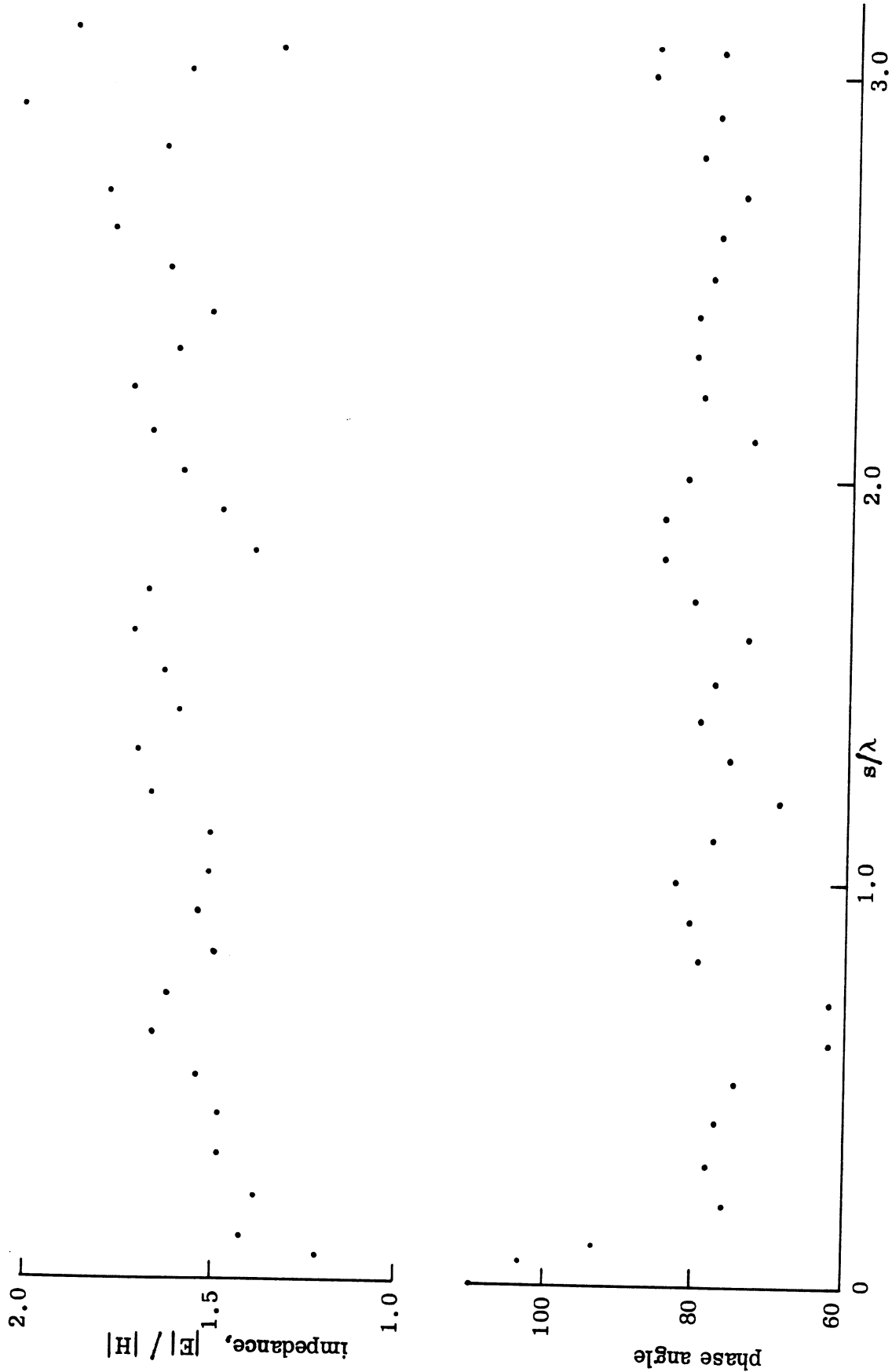


FIG.5-2: Deduced amplitude and phase of surface impedance for H-polarization. The phase is relative to an arbitrary value ϕ_0 .

dominant. The average values of $|\eta|$ over the entire surface are 1.33 for E-polarization and 1.61 for H-polarization, and the mean of these is almost identical to that deduced from the flat plate measurements. As judged by these measurements, we would now conclude that, with the possible exception of the end regions, the surface impedance on an ogival cylinder could be predicted to within about ± 20 percent using the flat plate (layer) value.

Unfortunately, all of these impedances are markedly different from that predicted by the theoretical layer formula when the electrical parameters of the Emerson and Cuming material are used. For a layer of thickness d backed by a perfect conductor and illuminated by a plane wave at an angle θ to the normal,

$$\eta = \sqrt{\mu/\epsilon} \left\{ 1 - \frac{\sin^2 \theta}{\mu\epsilon} \right\}^{\pm 1/2} \tanh \left\{ -ik_0 d(\mu\epsilon - \sin^2 \theta)^{1/2} \right\}$$

where ϵ and μ are the relative complex permittivity and permeability, respectively, and k_0 is the free space propagation constant. For the values of ϵ and μ given in Chapter IV with $k_0 d = 0.14363$ (0.09 in. thickness at 3.0 GHz), η changes by less than 0.5 percent in modulus and 0.7° in phase as θ varies from normal to glancing incidence. In particular, for $\theta = 0$,

$$\eta = 0.848 e^{i10.12^\circ} \quad (5.2)$$

which is quite different from the value measured using a single panel of the material. The power reflection coefficient deduced from eq. (5.2) is

$$\left| \frac{\eta - 1}{\eta + 1} \right|^2 = 0.01464 = -18.3 \text{ dB} \quad (5.3)$$

which is 5.3 dB below that which was found experimentally. The fact that the measured far field backscattering did not reveal the full theoretical reduction which the absorber is capable of is not surprising in view of the relatively small size of the absorber panel, the presence of the adhesive used to attach the absorber to its metal backing, and, last but not least, room reflections and other experimental errors. All of these effects would tend to underestimate the absorber performance.

The substantial discrepancy between the theoretical and measured values for the surface impedance is even more serious, however, and we shall return to this matter later in this chapter.

In addition to the infinite metallic plate coated with a uniform homogeneous layer, there is another geometry for which we can theoretically compute the impedance presented by a coating. This is the sphere. For plane wave incidence on a sphere of radius a coated with a layer of thickness d , the expressions for the surface impedances $\eta_{\theta}(\theta)$ and $\eta_{\phi}(\theta)$ in the electric and magnetic planes respectively are derived in Appendix A. A program has been written to compute these quantities as functions of θ from $\theta = 0$ (front) to $\theta = 180^{\circ}$ (back) in increments of 1° for any (complex) permittivity and permeability of the layer material. For a sphere having $k_0 a = 10.343$ and a layer whose relative permittivity and permeability are those of the Emerson and Cuming material, with an electrical thickness which approximates that used in the experiments, it is found that $\eta_{\theta}(\theta)$ and $\eta_{\phi}(\theta)$ are almost constant and virtually indistinguishable from their values for a planar layer. The maximum deviations are less than 1 percent in modulus and 1.3° in phase. A portion of the output for this case is included in Appendix A, and we may note that the computed reduction in the backscattering cross section is almost identical to that predicted by the power reflection coefficient (5.3) for the material.

The almost complete identity between the spherical and planar surface impedances is gratifying, albeit a little surprising in view of the completely different surface fields which the two structures can support. In an attempt to pinpoint the attributes of the layer material responsible for the agreement, a number of other cases have been run. Decreasing markedly the real and imaginary parts of the relative permittivity (to $2.0 + i0.03$) whilst leaving the other parameters substantially unchanged produces the surface impedance whose modulus is plotted as the upper curve in Fig. 5-3. There is now a marked variation as a function of θ . The period of the dominant oscillation is appropriate to waves which have proceeded around the sphere in space rather than in the layer. The "spikes" are believed real and are superimposed on a slowly varying mean. Over most of the sphere the departure from the slab impedance

$\epsilon_r = 2.0 + i1.03$
 $\mu_r = 4.4 + i3.25$

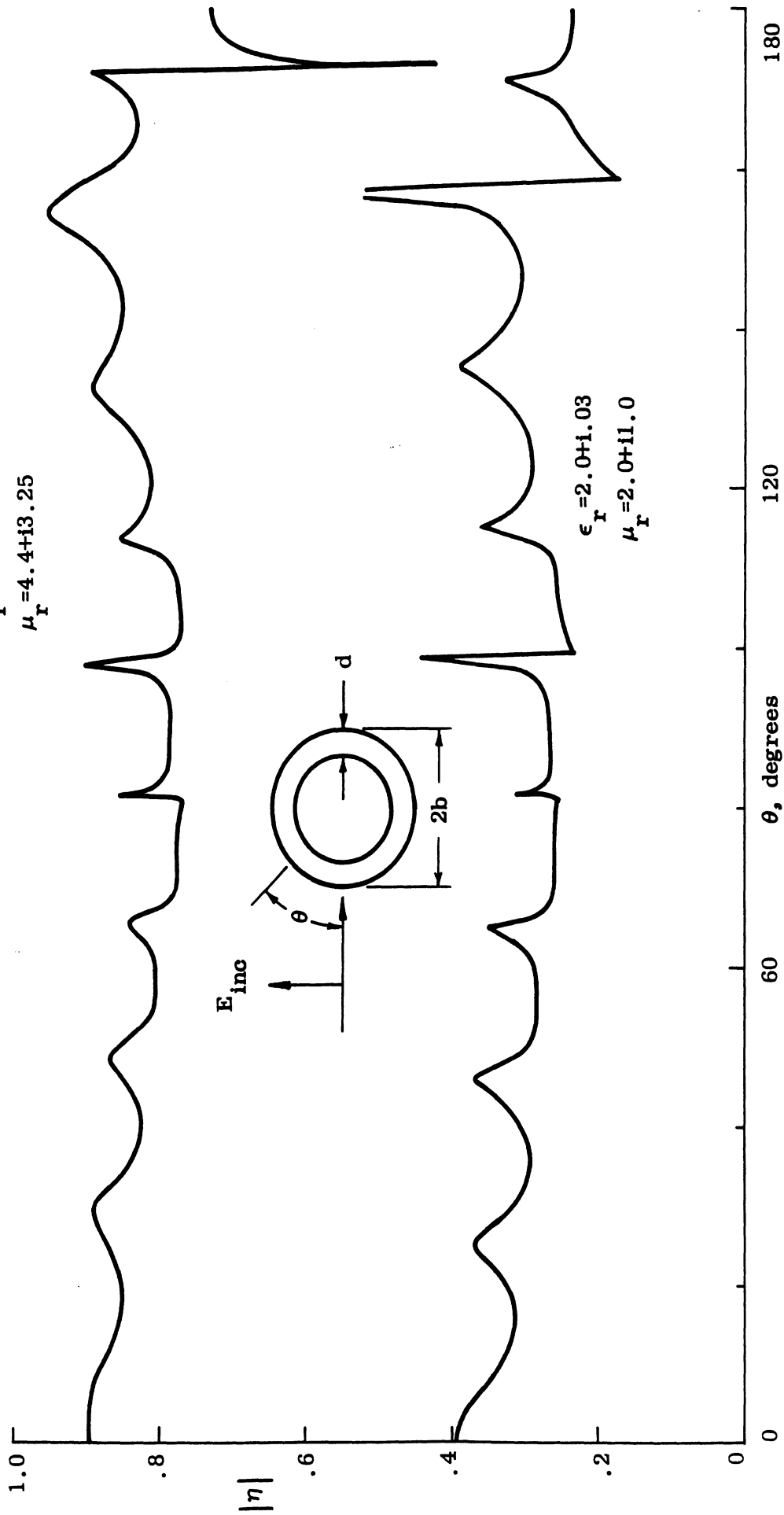


FIG. 5-3: Surface impedance of a coated sphere at a function of position for two types of coatings.

($\eta = 0.8768 e^{-i50.42^\circ}$) is less than 10 percent, with the agreement being closest at the front of the sphere, but considerable differences are evident in the vicinity of the focal point of the creeping waves at $\theta = 180^\circ$. The effect of reducing also the relative permeability (to $2.0 + i1.0$) is shown in the lower curve of Fig. 5-3. The spikes are still present, and the tendency of the impedance to fall below its slab value ($\eta = 0.3457 e^{-i62.51^\circ}$) is more apparent. For both of the coatings used in Fig. 5-3, the differences between η_θ and η_ϕ are insignificant. The cross section reductions which they provide are also rather poor: 6.0 and 3.1 dB, respectively.

It is our intention to explore further the connection between the actual and slab values of the surface impedance using this sphere model. However, from the theoretical results obtained so far, and from the experimental studies of the ogival cylinder and flat plate, it would appear that for a good absorber mounted on a surface of radius $\geq \lambda$ the surface impedance is closely approximated by its slab value. This conclusion is valid under circumstances where either creeping or traveling waves exist, and though it remains to be seen whether it also holds in the vicinity of edges, it would permit us to relate surface impedances to material constants using the simple case of the slab model.

We now return to the troubling discrepancy between the measured surface impedances on the ogival cylinder and plate and the theoretical value for the plate. In all the measurements, the absorber was attached to the plate with an adhesive whose relative permittivity and permeability are approximately $\epsilon = 4.0$, $\mu = 1.0$ and whose thickness is about 0.01 in. It seemed possible, though extremely unlikely, that this could affect the measured impedances. However, calculations using the theoretical (single) layer formula in which d was increased by 10 percent, and/or ϵ and μ reduced by the same amount produced only a small change in the surface impedance. The conclusion that this is not the source of the discrepancy is otherwise evident from the reasonable agreement between the measured and theoretical power reflection coefficients. It would therefore appear that the discrepancy is due to some error in the surface field measurements and a number of factors point to the electric

field in particular. Several tests have been performed to try to pinpoint the trouble, and these have included additional scans over the surface of the absorber coated plate, as well as measurements as a function of distance normal to the surface. The latter have revealed a variation with distance which is certainly not that expected for an infinite plate, but further tests are necessary to show whether the fault lies with the probe or with an inadequate size of plate.

VI. SUMMARY AND CONCLUSIONS

The mechanisms responsible for the non-specular scattering considered in this contract were traveling waves, creeping waves and edge diffraction. The first two occur primarily for H-polarization and the last for E-polarization, and although we must ultimately consider all three, limitations in time and software have confined the study to the first two. The major research tool used was a computer program that digitally solves the surface field integral equations for an impedance boundary condition, but additional information was also obtained from auxiliary theoretical and experimental work.

A pair of two-dimensional bodies were used to study the non-specular scattering, each intended to isolate a single mechanism for H-polarization. An ogival cylinder has sharp leading and trailing edges and the dominant source of return is the excitation of traveling waves which build up at the rear edge. The wedge cylinder formed by the mating of a circular cylinder with a wedge supports a creeping wave that skirts the rounded back of the body and emerges on the opposite side. The net returns from both objects tend to be contaminated by additional sources and although the additional source for the ogival cylinder (direct diffraction from the leading edge) is quite small, the additional sources for the wedge cylinder (join returns) are comparable in amplitude to the mechanism being studied.

By means of repeated "digital experiments" using the computer program, sufficient data were collected to establish design criteria for the variation in surface impedance for the two obstacles. In both cases, at least for H-polarization, we found that the surface impedance should taper from a small value near the leading edge to as high a value as is practicable at the source of scattering. The most consistently effective taper has been a linear one, probably because it places the greatest amount of loss on the surface with the least disturbance to the surface fields at the endpoints of the loaded region. Cross section reductions in excess of 13 dB have been achieved, but only by utilizing much of the available surface for the loading.

All attempts to reduce the amount of surface to be covered produced a loss in performance which, up to a certain degree, could be recovered if the impedance was increased to a high enough level at the source of scattering. However, this failed to be effective when the surface available for treatment became too short. There is strong evidence (in the form of far field scattering characteristics) to suggest that when the available surface is not extensive enough, thus requiring a rapid rise in impedance in order to attain the necessary high level, a new source of scattering is introduced. It is our belief that no single form of taper—i. e., linear, exponential, cubic, etc.—can overcome this difficulty for short loading distances. After all, when the loading is carried to the limit (zero distance) it becomes a mere cancellation scheme requiring heavily reactive impedance components effective only over narrow frequency bands.

Midway through the research effort we encountered difficulties with the computer programs for E-polarization and this is the reason no results have been reported for this polarization. Using the same technique that had been consistently and successfully exploited for H-polarization, we produced erroneous surface field distributions as well as far field scattering patterns. We discovered, however, that the results could be improved by concentrating the sampling points densely near the edges. Subsequent explorations have produced a combination of slightly rounded edges (i. e., small radii of curvature) and dense packing that comes within 2 dB of predicting what is felt to be the correct far field scattering. A more accurate and less cumbersome procedure was desired, of course, but lack of time and funds did not allow a more thorough study of the fundamental problem to be undertaken.

The experimental program undertaken in the contract was at once useful and disappointing—useful because the data confirmed our previous contention that GTD is a reliable theoretical tool for predicting the scattering from conducting edges and disappointing because we could not determine the surface impedance as accurately as we had hoped possible. The difficulties seem to hinge on the uncertainties of measuring the tangential electric field near an imperfectly conducting surface and it may be that an electric field probe does not respond to the desired field quantity or that it distorts the field being probed.

In summary, our findings are that surface impedances can be found which suppress H-polarized non-specular scattering, but that such methods require a half-wavelength or so of surface to be effective. Future work will be devoted to synthesizing these favorable impedance variations with physically realizable materials. We cannot yet prescribe favorable E-polarization treatments for leading edges, and obviously any future work must first determine what form they shall have before addressing the synthesis problem using actual coating systems. It must be remembered that the computer program relies upon an impedance boundary condition, an abstraction that does not account for material properties. If possible, a program based on the specification of electrical characteristics should be created which could then bear more directly on the problem at hand.

Appendix A: The Surface Impedance of a Coated Sphere

Consider a perfectly conducting sphere of radius a coated with a uniform layer of thickness $d = b - a$ and illuminated by a plane electromagnetic wave. The layer is composed of a homogeneous isotropic material whose complex constitutive parameters are ϵ_2 and μ_2 and if the incident plane wave is polarized in the \hat{x} direction and propagating in the $-\hat{z}$ direction, we can write

$$\underline{E}^i = \hat{x} e^{-ik_0 z}, \quad \underline{H}^i = -Y_0 \hat{y} e^{-ik_0 z} \quad (\text{A.1})$$

where $Y_0 = 1/Z_0$ is the intrinsic admittance of free space. Mks units are employed and a time factor $e^{-i\omega t}$ suppressed.

In terms of spherical vector wave functions, the incident field (A.1) is

$$\underline{E}^i = \sum_{n=1}^{\infty} (-i)^n \frac{2n+1}{n(n+1)} \left(M_{\text{oin}}^{(1)} + i N_{\text{ein}}^{(1)} \right)$$

$$\underline{H}^i = -i Y_0 \sum_{n=1}^{\infty} (-i)^n \frac{2n+1}{n(n+1)} \left(N_{\text{oin}}^{(1)} + i M_{\text{ein}}^{(1)} \right)$$

with

$$\frac{M_{\text{ein}}^{(1)}}{e_{\text{in}}} = \frac{\psi_n(kr)}{kr} \frac{P_n^{(1)}(\cos\theta)}{\sin\theta} \frac{\sin\phi}{\cos\phi} \hat{\theta} - \frac{\psi_n(kr)}{kr} \frac{\partial}{\partial\theta} P_n^{(1)}(\cos\theta) \frac{\cos\phi}{\sin\phi} \hat{\phi}$$

$$\frac{N_{\text{ein}}^{(1)}}{e_{\text{in}}} = n(n+1) \frac{\psi_n(kr)}{(kr)^2} \frac{\partial}{\partial\theta} P_n^{(1)}(\cos\theta) \frac{\cos\phi}{\sin\phi} \hat{r}$$

$$+ \frac{\psi'_n(kr)}{kr} \frac{\partial}{\partial\theta} P_n^{(1)}(\cos\theta) \frac{\cos\phi}{\sin\phi} \hat{\theta} + \frac{\psi'_n(kr)}{kr} \frac{P_n^{(1)}(\cos\theta)}{\sin\theta} \frac{\sin\phi}{\cos\phi} \hat{\phi}$$

(Stratton, 1941; p.416), where

$$\psi_n(z) = z j_n'(z) = \sqrt{\frac{\pi z}{2}} J_{n+1/2}'(z)$$

is the modified spherical Bessel function and the prime denotes differentiation with respect to the entire argument. The associated Legendre function $P_n^{(1)}(\cos\theta)$ is defined as in Stratton.

Outside the sphere, i.e. for $r \geq a + d = b$, the scattered field can be written as

$$\underline{E}^S = - \sum_{n=1}^{\infty} (-i)^n \frac{2n+1}{n(n+1)} \left\{ A_n M_{oin}^{(3)} + i B_n N_{ein}^{(3)} \right\},$$

$$\underline{H}^S = i Y_0 \sum_{n=1}^{\infty} (-i)^n \frac{2n+1}{n(n+1)} \left\{ A_n N_{oin}^{(3)} + i B_n M_{ein}^{(3)} \right\},$$

where the vector wave functions of the third kind differ from those of the first in having $\psi_n(kr)$ replaced by the modified spherical Hankel function $\xi_n(kr)$:

$$\xi_n(z) \equiv z h_n^{(1)}(z) = \sqrt{\frac{\pi z}{2}} H_{n+1/2}^{(1)}(z).$$

Application of the boundary conditions at $r = a, b$ then yields

$$A_n = \frac{\psi_n(k_o b) + \Gamma_n^{(1)} \psi_n'(k_o b)}{\xi_n(k_o b) + \Gamma_n^{(1)} \xi_n'(k_o b)}$$

$$B_n = \frac{\psi_n'(k_o b) - \Gamma_n^{(2)} \psi_n(k_o b)}{\xi_n'(k_o b) - \Gamma_n^{(2)} \xi_n(k_o b)} \quad (A.2)$$

with

$$\Gamma_n^{(1)} = -\frac{Z_2}{Z_0} \cdot \frac{P_3}{P_4}, \quad \Gamma_n^{(2)} = \frac{Z_2}{Z_0} \cdot \frac{P_2}{P_1} \quad (\text{A.3})$$

where

$$\begin{aligned} P_1 &= \psi'_n(k_2 a) \xi_n(k_2 b) - \xi'_n(k_2 a) \psi_n(k_2 b) \\ P_2 &= \psi'_n(k_2 a) \xi'_n(k_2 b) - \xi'_n(k_2 a) \psi'_n(k_2 b) \\ P_3 &= \psi_n(k_2 a) \xi_n(k_2 b) - \xi_n(k_2 a) \psi_n(k_2 b) \\ P_4 &= \psi_n(k_2 a) \xi'_n(k_2 b) - \xi_n(k_2 a) \psi'_n(k_2 b) \end{aligned} \quad (\text{A.4})$$

in which

$$Z_2 = \sqrt{\frac{\mu_2}{\epsilon_2}}, \quad k_2 = \omega \sqrt{\mu_2 \epsilon_2}$$

(Senior and Desjardins, 1972). As pointed out in this reference, $i\Gamma_n^{(1)}$ and $i\Gamma_n^{(2)}$ are the effective surface impedances of the n th magnetic and electric modes respectively. In other words, if we had considered the problem of a sphere of radius b at whose surface the boundary condition

$$\underline{E} - (\underline{E} \cdot \hat{n}) \hat{n} = \eta Z_0 \hat{n} \wedge \underline{H} \quad (\text{A.5})$$

is imposed where \hat{n} is a unit normal in the outwards (radial) direction, the coefficients A_n and B_n specifying the scattered field would have been the same as the above with

$$\Gamma_n^{(1)} = \Gamma_n^{(2)} = -i\eta. \quad (\text{A.6})$$

At the outer surface $r = b$, the tangential components of the total (incident plus scattered) field are

$$\begin{aligned}
E_{\theta} &= - \sum_{n=1}^{\infty} (-i)^n \frac{2n+1}{n(n+1)} \left[\left(A_n \xi_n(k_o b) - \psi_n(k_o b) \right) \frac{P_n^{(1)}(\cos \theta)}{\sin \theta} \right. \\
&\quad \left. + i \left(B_n \xi'_n(k_o b) - \psi'_n(k_o b) \right) \frac{\partial}{\partial \theta} P_n^{(1)}(\cos \theta) \right] \frac{\cos \theta}{k_o b} \\
E_{\phi} &= \sum_{n=1}^{\infty} (-i)^n \frac{2n+1}{n(n+1)} \left[\left(A_n \xi_n(k_o b) - \psi_n(k_o b) \right) \frac{\partial}{\partial \theta} P_n^{(1)}(\cos \theta) \right. \\
&\quad \left. + i \left(B_n \xi'_n(k_o b) - \psi'_n(k_o b) \right) \frac{P_n^{(1)}(\cos \theta)}{\sin \theta} \right] \frac{\sin \theta}{k_o b} \\
H_{\theta} &= i Y_o \sum_{n=1}^{\infty} (-i)^n \frac{2n+1}{n(n+1)} \left[\left(A_n \xi'_n(k_o b) - \psi'_n(k_o b) \right) \frac{\partial}{\partial \theta} P_n^{(1)}(\cos \theta) \right. \\
&\quad \left. - i \left(B_n \xi_n(k_o b) - \psi_n(k_o b) \right) \frac{P_n^{(1)}(\cos \theta)}{\sin \theta} \right] \frac{\sin \theta}{k_o b} \\
H_{\phi} &= i Y_o \sum_{n=1}^{\infty} (-i)^n \frac{2n+1}{n(n+1)} \left[\left(A_n \xi'_n(k_o b) - \psi'_n(k_o b) \right) \frac{P_n^{(1)}(\cos \theta)}{\sin \theta} \right. \\
&\quad \left. - i \left(B_n \xi_n(k_o b) - \psi_n(k_o b) \right) \frac{\partial}{\partial \theta} P_n^{(1)}(\cos \theta) \right] \frac{\cos \theta}{k_o b} .
\end{aligned}$$

But

$$A_n \xi_n(k_o b) - \psi_n(k_o b) = \frac{\Gamma_n^{(1)} \{ \psi'_n \xi_n - \psi_n \xi'_n \}}{\xi_n + \Gamma_n^{(1)} \xi'_n}$$

and since

$$j_n h_n^{(1)'} - j_n' h_n^{(1)} = \frac{i}{(k_o b)^2}$$

(Bowman et al, 1969; p.59) it follows that

$$\psi_n' \xi_n - \psi_n \xi_n' = -i \quad .$$

Hence

$$A_n \xi_n(k_o b) - \psi_n(k_o b) = -i \frac{\Gamma_n^{(1)}}{\xi_n(k_o b) + \Gamma_n^{(1)} \xi_n'(k_o b)}$$

and similarly

$$B_n \xi_n'(k_o b) - \psi_n'(k_o b) = -i \frac{\Gamma_n^{(2)}}{\xi_n'(k_o b) - \Gamma_n^{(2)} \xi_n(k_o b)}$$

$$A_n \xi_n'(k_o b) - \psi_n'(k_o b) = \frac{i}{\xi_n(k_o b) + \Gamma_n^{(1)} \xi_n'(k_o b)}$$

$$B_n \xi_n(k_o b) - \psi_n(k_o b) = \frac{-i}{\psi_n'(k_o b) - \Gamma_n^{(2)} \xi_n(k_o b)} \quad .$$

The tangential components of the surface field are therefore

$$E_\theta = - \sum_{n=1}^{\infty} (-i)^{n+1} \frac{2n+1}{n(n+1)} \left[\frac{\Gamma_n^{(1)}}{\xi_n + \Gamma_n^{(1)} \xi_n'} \frac{P_n^{(1)}(\cos\theta)}{\sin\theta} + i \frac{\Gamma_n^{(2)}}{\xi_n' - \Gamma_n^{(2)} \xi_n} \frac{\partial}{\partial\theta} P_n^{(1)}(\cos) \right] \cdot \frac{\cos\phi}{k_o b} \quad (A.7)$$

$$E_{\phi} = \sum_{n=1}^{\infty} (-i)^{n+1} \frac{2n+1}{n(n+1)} \left[\frac{\Gamma_n^{(1)}}{\xi + \Gamma_n^{(1)} \xi'} \frac{\partial}{\partial \theta} P_n^{(1)}(\cos \theta) + i \frac{\Gamma_n^{(2)}}{\xi' - \Gamma_n^{(2)} \xi} \frac{P_n^{(1)}(\cos \theta)}{\sin \theta} \right] \cdot \frac{\sin \phi}{k_o b} \quad (\text{A.8})$$

$$H_{\theta} = -i Y_o \sum_{n=1}^{\infty} (-i)^{n+1} \frac{2n+1}{n(n+1)} \left[\frac{1}{\xi + \Gamma_n^{(1)} \xi'} \frac{\partial}{\partial \theta} P_n^{(1)}(\cos \theta) + i \frac{1}{\xi' - \Gamma_n^{(2)} \xi} \frac{P_n^{(1)}(\cos \theta)}{\sin \theta} \right] \cdot \frac{\sin \phi}{k_o b} \quad (\text{A.9})$$

$$H_{\phi} = -i Y_o \sum_{n=1}^{\infty} (-i)^{n+1} \frac{2n+1}{n(n+1)} \left[\frac{1}{\xi + \Gamma_n^{(1)} \xi'} \frac{P_n^{(1)}(\cos \theta)}{\sin \theta} + i \frac{1}{\xi' - \Gamma_n^{(2)} \xi} \frac{\partial}{\partial \theta} P_n^{(1)}(\cos \theta) \right] \cdot \frac{\cos \phi}{k_o b} \quad (\text{A.10})$$

and if we now define the equivalent surface impedances η_{θ} and η_{ϕ} such that (locally)

$$E_{\theta} = -\eta_{\theta} Z_o H_{\phi}, \quad E_{\phi} = \eta_{\phi} Z_o H_{\theta} \quad (\text{A.11})$$

then

$$\eta_{\theta}(\theta) = i \frac{\sum_{n=1}^{\infty} (-i)^{n+1} \frac{2n+1}{n(n+1)} \left[\frac{\Gamma_n^{(1)}}{\xi + \Gamma_n^{(1)} \xi'} \frac{P_n^{(1)}(\cos \theta)}{\sin \theta} + i \frac{\Gamma_n^{(2)}}{\xi' - \Gamma_n^{(2)} \xi} \frac{\partial}{\partial \theta} P_n^{(1)}(\cos \theta) \right]}{\sum_{n=1}^{\infty} (-i)^{n+1} \frac{2n+1}{n(n+1)} \left[\frac{1}{\xi + \Gamma_n^{(1)} \xi'} \frac{P_n^{(1)}(\cos \theta)}{\sin \theta} + i \frac{1}{\xi' - \Gamma_n^{(2)} \xi} \frac{\partial}{\partial \theta} P_n^{(1)}(\cos \theta) \right]} \quad (\text{A.12})$$

$$\eta_{\phi}(\theta) = i \frac{\sum_{n=1}^{\infty} (-i)^{n+1} \frac{2n+1}{n(n+1)} \left[\frac{\Gamma_n^{(1)}}{\xi + \Gamma_n^{(1)} \xi'} \frac{\partial}{\partial \theta} P_n^{(1)}(\cos \theta) + i \frac{\Gamma_n^{(2)}}{\xi' - \Gamma_n^{(2)} \xi} \frac{P_n^{(1)}(\cos \theta)}{\sin \theta} \right]}{\sum_{n=1}^{\infty} (-i)^{n+1} \frac{2n+1}{n(n+1)} \left[\frac{1}{\xi + \Gamma_n^{(1)} \xi'} \frac{\partial}{\partial \theta} P_n^{(1)}(\cos \theta) + i \frac{1}{\xi' - \Gamma_n^{(2)} \xi} \frac{P_n^{(1)}(\cos \theta)}{\sin \theta} \right]} \quad (\text{A.13})$$

Observe that the expressions for η_{θ} and η_{ϕ} differ only in having $\frac{P_n^{(1)}(\cos \theta)}{\sin \theta}$

and $\frac{\partial}{\partial \theta} P_n^{(1)}(\cos \theta)$ interchanged, and under such conditions (if any) that

$$\Gamma_n^{(1)} = \Gamma_n^{(2)} = \text{constant} = \Lambda$$

(say) independently of n ,

$$\eta_{\theta}(\theta) = \eta_{\phi}(\theta) = i \Lambda \quad (\text{A.14})$$

independent of θ . This is the only situation in which the effect of the uniform coating can be fully simulated using a constant impedance boundary condition, and η_{θ} and η_{ϕ} are then the surface impedance η introduced earlier.

In an attempt to realize this situation and, at the same time, obtain an expression for the constant impedance η , consider those modes for which

$$|k_2 a| \gg n(n+1). \quad (\text{A.15})$$

As shown by Senior and Desjardins (1972), we then have

$$P_1 \sim -i \left\{ \cos k_2 d + \frac{n(n+1)d/a}{2 k_2 b} \sin k_2 d \right\} \quad (\text{A.16})$$

with similar expressions for P_2 , P_3 and P_4 . These are valid regardless of the layer thickness, but if $d \ll a$ the second term in (A.14) can be neglected in comparison with the first ^{*} yielding

$$P_1 \sim -i \cos k_2 d .$$

Similarly,

$$P_2 , P_3 \sim i \sin k_2 d$$

$$P_4 \sim i \cos k_2 d$$

from which we have

$$\Gamma_n^{(1)} , \Gamma_n^{(2)} \sim - \frac{Z_2}{Z_0} \tan k_2 d .$$

The modal impedances are now independent of the mode number and identical to the surface impedance of a planar layer viewed at normal incidence, viz

$$\eta = -i \frac{Z_2}{Z_0} \tan k_2 d . \quad (\text{A.17})$$

It is evident that the condition (A.15) is a key one. If it is satisfied even for the highest mode necessary in the representation of the surface fields, the modal impedances will be equal, and the resulting net impedances η_θ and η_ϕ will be independent of position and identical to the layer impedance (A.17). Unfortunately, (A.15) is a very restrictive condition. For a metal sphere with $k_0 a = 10$ it is known (Ducmanis and Liepa, 1965) that at least 20 modes are necessary to accurately determine the surface fields. It is almost inconceivable that fewer modes will suffice when the sphere is coated, but if we assume that

*An exception occurs if $k_2 d$ is an odd multiple of $\pi/2$, but this is possible only if k_2 is purely real.

20 modes are still adequate, the condition (A.15) implies

$$|k_2 a| \gg 420$$

$$\text{i. e. } \left| \frac{\epsilon \mu}{\epsilon_0 \mu_0} \right| \gg 1764 . \quad (\text{A.18})$$

Thus, the layer material must have an enormous dielectric constant or considerable loss or both, and it is difficult to imagine a material other than a pseudo-metal for which the condition (A.18) is fulfilled. Note that the condition is not significantly changed if $k_0 a$ is small, e.g. $k_0 a = 1$.

For values of ϵ and μ more typical of lossy (absorbing) coatings, it seems inevitable that η_θ and η_ϕ will be functions of θ and it is now of interest to see how they differ from the planar layer approximation. To this end, a program has been written to compute $\eta_\theta(\theta)$ and $\eta_\phi(\theta)$ from eqs. (A.12) and (A.13) for different combinations of parameters. The crux of the problem is the computation of $\Gamma_n^{(1)}$ and $\Gamma_n^{(2)}$ and this requires us to find P_1, \dots, P_4 . If the coating were a pure dielectric, it is well known (see, for example, Rheinstejn, 1964) that the fields are very sensitive to the parameters involved, and for a given material and layer thickness, a change in a/λ of as little as 10^{-6} can produce a large change in the scattered field. In this case, extreme accuracy in the computation of $\Gamma_n^{(1)}$ and $\Gamma_n^{(2)}$ would be required. It is not expected that such sensitivity will occur with lossy coatings since the absorption will attenuate any waves traveling in the layer.

The program is relatively straightforward. The Bessel functions of either real or complex argument are calculated using a backwards recursion scheme developed at the Radiation Laboratory, while the Neumann and Legendre functions are found using forward schemes. Double precision (IBM) arithmetic

is used throughout to avoid undue error build-ups in the forward recursion schemes and to ensure adequate accuracy in the surface impedance values.

The input parameters are n_{\max} (the number of modes included), k_0 , b , d , μ_2/μ_0 (complex) and ϵ_2/ϵ_0 (complex). For reasons of economy we have usually chosen $n_{\max} \leq 50$ which, for the type of coatings of interest, restricts us to core radii less than (about) 2λ . The surface impedances $\eta_\theta(\theta)$ and $\eta_\phi(\theta)$ are computed at intervals of 1° , $0 \leq \theta \leq 180^\circ$, and their values are printed out in real and imaginary parts, modulus and phase. For comparison, the impedance (eq. A.17) of a planar layer of the material is also computed. In the far field

$$\underline{E}^S(0) = \frac{e^{ikr}}{kr} S(0) \hat{x}$$

(backscattering), where

$$S(0) = i \sum_{n=1}^{\infty} (-1)^n \left(n + \frac{1}{2}\right) (A_n - B_n) \quad (\text{A.19})$$

and

$$\underline{E}^S(\pi) = \frac{e^{ikr}}{kr} S(\pi) \hat{x}$$

(forward scattering), where

$$S(\pi) = i \sum_{n=1}^{\infty} \left(n + \frac{1}{2}\right) (A_n + B_n). \quad (\text{A.20})$$

In terms of the far field amplitude S , the normalized scattering cross section, $\sigma/(\pi a^2)$, is

$$\frac{\sigma}{\pi a^2} = \left(\frac{2}{k_0 a}\right)^2 |S|^2 . \quad (\text{A.21})$$

The quantities $S(0)$ and $S(\pi)$ are computed (real and imaginary parts and phase) along with the corresponding normalized cross sections $\sigma(0)/\pi a^2$ and $\sigma(\pi)/\pi a^2$.

Additional (optional) outputs consist of the quantities $\Gamma_n^{(1)}$ and $\Gamma_n^{(2)}$, and A_n and B_n . The former are of interest in showing how the modal impedances vary from mode to mode while the latter serve to check that an adequate number of modes have been included. A typical output is as follows.

layer	GAMMA-1	GAMMA-2	GAMMA-3
1	0.7668130 00	0.76694700 00	-0.76250630 00
2	0.76699300 00	0.76705300 00	-0.76263370 00
3	0.76700900 00	0.76715970 00	-0.76272650 00
4	0.76703100 00	0.76721430 00	-0.76278200 00
5	0.76705100 00	0.76727000 00	-0.76284300 00
6	0.76707800 00	0.76733760 00	-0.76291720 00
7	0.76712620 00	0.76741650 00	-0.76300900 00
8	0.76718330 00	0.76750790 00	-0.76312090 00
9	0.76725600 00	0.76761420 00	-0.76325710 00
10	0.76734060 00	0.76773900 00	-0.76342230 00
11	0.76744170 00	0.76788600 00	-0.76362400 00
12	0.76756600 00	0.76805900 00	-0.76386350 00
13	0.76771500 00	0.76826300 00	-0.76414900 00
14	0.76789000 00	0.76850300 00	-0.76449100 00
15	0.76809500 00	0.76878400 00	-0.76489300 00
16	0.76833000 00	0.76911200 00	-0.76536700 00
17	0.76859500 00	0.76949300 00	-0.76592500 00
18	0.76889000 00	0.76993200 00	-0.76657800 00
19	0.76921500 00	0.77043500 00	-0.76733700 00
20	0.76957000 00	0.77099900 00	-0.76821400 00
21	0.76995500 00	0.77163000 00	-0.76922000 00
22	0.77037000 00	0.77233500 00	-0.77036400 00
23	0.77081500 00	0.77311900 00	-0.77164900 00
24	0.77129000 00	0.77398700 00	-0.77307700 00
25	0.77179500 00	0.77494500 00	-0.77465300 00

THE THICKNESS OF THE SURFACE LAYER IS 0.77003920 00 0.79011360 00 19.9850166EFS

SC(1) IS	0.111614850 01	-0.114220140 -01
S(P1) IS	-0.106697120 02	0.660085070 02
SIGMA(P1)/H IS	0.0652925	PHI IS -0.5958703 050EFS
SIGMA(P1)/H IS	162.87014703	PHI IS 50.0075432 050EFS
Surface WITH LAYER		
0.364260 00	0.152320 -01	0.600910 00 -0.189710 -01
0.596350 00	-0.510630 -01	0.415620 00 -0.598510 -01
0.433880 00	0.954100 -01	0.531110 00 -0.542630 -01
0.693230 00	-0.217310 00	0.592130 00 -0.916260 -01
0.703660 00	0.643240 -01	0.606250 00 -0.133920 -01
0.392760 00	0.752700 -01	0.590270 00 -0.957450 -01
0.660700 00	-0.160120 00	0.503260 00 -0.147140 -01
0.679710 00	0.504510 -01	0.577420 00 -0.107310 00
0.626160 00	0.152530 00	0.440330 00 -0.161560 00
0.304040 00	0.252910 00	0.232130 00 -0.130760 00
0.103790 00	0.169170 00	0.161510 00 -0.509330 -01
0.952790 -01	0.668830 -01	0.562050 -01 -0.116700 -01
0.291550 -01	0.180160 -01	0.137340 -01 -0.797630 -02
0.668230 -02	0.241620 -02	0.392030 -02 -0.596600 -02
0.110760 -02	0.226600 -03	0.232530 -03 -0.320130 -02
0.175300 -03	0.126680 -04	0.942510 -04 -0.417000 -04
0.206030 -04	-0.715820 -04	0.072810 -05 -0.502640 -04
0.210000 -04	-0.270070 -06	0.571330 -06 -0.430630 -06
0.187600 -06	-0.397300 -07	0.551200 -07 -0.632610 -07

Appendix B: Program REST

Program REST is a modification of program RAMC, the latter supplied us by AFAL in 1972. REST solves the E-polarization integral equation for a two-dimensional metallic obstacle whose surface may or may not be shielded by thin resistive sheets. REST constructs the profiles of both the body and the sheets, if any, by generating surface sampling points along circular arcs or straight line segments whose endpoints are specified by the user on input. An option is available by which the user may construct completely arbitrary profiles by feeding in sampling coordinates point-by-point. Metallic and resistive surface elements are distinguished from one another only by means of the specific value of resistance associated with each. In the original RAMC, the program indexed through resistive elements first, then metallic elements, but program REST indexes through the elements in the order they were created or specified, regardless of their metallic or resistive nature.

The program consists of a MAIN program plus four subroutines named GEOM, ZVO8, HANK and ZFUN. MAIN reads control information from the input stream, sums surface currents to obtain far field scattering and indexes through the desired angles of incidence and scattering. If necessary (via the option control parameter IOPT), MAIN calls GEOM to set up the profiles of both the metallic body and the resistive sheets; GEOM also participates in input/output operations, if called. In order to generate the matrix elements required of the integral equation solution, MAIN calls HANK to supply the necessary Hankel functions of order zero. After all matrix elements have been created, MAIN calls ZVO8 to invert the matrix; if more than one angle of incidence is required, new values of incident field are computed, and the inverted matrix is then used to compute the new surface current distribution.

GEOM will compute a resistance variation along resistive sheets according to either of two mathematical formulae, depending on the value of the control parameter IMP. If the user needs other than the two built-in functions, a third option permits him to supply his own prescription in a subroutine ZFUN. If required, GEOM calls ZFUN but in the listing below, ZFUN is a dummy subroutine necessary only for the compilation of the program.

RAMC was used to compute surface and far fields of a small conducting circular cylinder surrounded by a concentric resistive sheet and these data were supplied as a sample test of the program run on the CDC 6600 machine at WPAFB. When the modified version REST was run on the IBM 360/67 at The University of Michigan, the original results of RAMC were duplicated, but when REST was tested on a metallic large cylinder ($ka=5$) in the absence of any resistive sheet, the results were grossly in error. A subsequent study suggested that the original inversion subroutine supplied with RAMC was not performing properly, but further closer examination showed that the Hankel functions were grossly wrong for arguments greater than (about) 8.0.

Thus the matrix inversion subroutine ZVO8 was borrowed from RAM1B and subroutine HANK was completely rewritten. We now obtain satisfactory results, but only by using double precision arithmetic in HANK. However, because the CDC computers are based upon a 48-bit word, whereas IBM uses 32-bit single precision and 64-bit double precision words, the single precision version of HANK shown below should be satisfactory on CDC systems.

The input format required by REST is as follows:

Card 1	FORMAT (18A4)	Title card, 72 EBCDIC characters
Card 2	FORMAT (2I5, F10.5)	IOPT, M, WAVE
	IOPT = 0	body coordinates read in
	IOPT \neq 0	body coordinates generated internally
	M	total number of cells
	WAVE	wavelength

Card 3	FORMAT (2I5, 3F10.5)	NINC, NBIT, DPH, DBIT, PHO
	NINC	number of incident directions
	NBIT	number of bistatic directions
	DPH	incident direction increment
	DBIT	bistatic direction increment
	PHO	initial incidence angle

The following cards are used if IOPT \neq 0 (requires N+1 cards):

Card 4	FORMAT (2I5, 5F10.4, 3I4)	N, IMP, XA, YA, XB, YB, ANG, IZA, IZB, IZEX,
	N	number of cells in the segment
	IMP<0	impedance given by user-supplied subroutine
	IMP=0	ZS(I)=ZA+ZB*S(I)**ZEX
	IMP>0	ZS(I)=ZA+ZB*EXP(-ZEX*S(I))
	XA, YA, XB, YB	segment endpoints
	ANG	angle subtended by segment
	IZA, IZB	integer resistivity constants
	IZEX	integer constant 10 times the desired ZEX

Card 5	FORMAT (I5)	integer zero in column 5; shuts off input reading of segment parameters
--------	-------------	---

The following cards are used if IOPT=0 (requires LL+1cards):

Card 4	FORMAT (2I5, 5F10.5)	(LUMP(I, J), J=1, 2), X(I), Y(I), S(I), DSQ(I), ZS(I)
	LUMP (I, 1)	cell ID number
	LUMP (I, 2)	segment ID number
	X(I), Y(I)	cell coordinates
	S(I)	distance along segment
	DSQ(I)	cell length
	ZS(I)	resistivity of cell

Card 5	FORMAT (I5)	LL
	LL	the number of segments in the profile

A listing of program REST is given on pages 92 to 99 .

```

C   PROGRAM REST---CONDUCTING CYLINDER + RESISTIVE SHEETS
      DIMENSION A(100,101),PHI(100),PINC(100),ID(18),LUMP(100,2)
      DIMENSION X(100),Y(100),S(100),DSQ(100),ZS(100)
      COMPLEX A,PHI,PINC,SUM,DEL
      DATA RED/0.01745329/
10  READ (5,100) ID
      READ (5,200) IDPT,M,WAVE
      READ (5,200) NINC,NBIT,DPH,DBIT,PH0
      XK=6.283185/WAVE
      WRITE (6,150) ID
      IF (IDPT.EQ.0) GO TO 15
      WRITE (6,300)
      CALL GF0M(LUMP,X,Y,S,DSQ,ZS,M,LL)
      GO TO 25
15  DO 20 I=1,M
      READ (5,200) (LUMP(I,J),J=1,2),X(I),Y(I),S(I),DSQ(I),ZS(I)
20  DSQ(I)=DSQ(I)/WAVE
      READ (5,200) LL
25  WRITE (6,400) LL,M,NINC,NBIT,WAVE
      WRITE (6,150) ID
      WRITE (6,500)
      DO 30 I=1,M
      IF (IDPT.NE.0) DSQ(I)=DSQ(I)/WAVE
30  WRITE (6,200) (LUMP(I,J),J=1,2),X(I),Y(I),S(I),DSQ(I),ZS(I)
      DO 90 K=1,NINC
      PH=PH0-(K-1)*DPH
      IF (K.GT.1) GO TO 45
      DO 40 I=1,M
      DO 40 J=1,M
      IF (I.NE.J) GO TO 35
      A(I,J)=DSQ(J)*CMPLX(1.570796,0.7219456+ALOG(DSQ(J)))
      IF (ZS(J).NE.0.0) A(I,J)=1.0+A(I,J)/ZS(J)
      GO TO 40
35  RPQ=XK*SQRT((X(I)-X(J))**2+(Y(I)-Y(J))**2)
      CALL HANK(RPQ,0,BJ,H)
      A(I,J)=1.570796*DSQ(J)*CMPLX(BJ,H)
      IF (ZS(J).NE.0.0) A(I,J)=A(I,J)/ZS(J)
40  CONTINUE
45  THE=RED*PH
      DO 50 I=1,M
      HOLD=-XK*(X(I)*COS(THE)+Y(I)*SIN(THE))
50  PINC(I)=CMPLX(COS(HOLD),SIN(HOLD))
      CALL ZV08(A,M,PINC,PHI,K)
      WRITE (6,600) PH
      DO 70 I=1,M
      AMP=CABS(PHI(I))
      IF (REAL(PHI(I)).NE.0.0) GO TO 55
      PHASE=90.0*AIMAG(PHI(I))/AMP
      GO TO 60
55  PHASE=57.29578*ATAN2(AIMAG(PHI(I)),REAL(PHI(I)))
60  FAMP=CABS(PINC(I))
      IF (REAL(PINC(I)).NE.0.0) GO TO 65
      FASE=90.0*AIMAG(PINC(I))/FAMP
      GO TO 70
65  FASE=57.29578*ATAN2(AIMAG(PINC(I)),REAL(PINC(I)))
70  WRITE (6,700) (LUMP(I,J),J=1,2),AMP,PHASE,FAMP,FASE
      WRITE (6,800) PH
      DO 80 I=1,NBIT
      THE=180.0-(I-1)*DBIT
      TETA=RED*THE

```

```

SUM=CMPLX(0.0,0.0)
DO 75 J=1,M
RS=-(X(J)*COS(TETA)+Y(J)*SIN(TETA))*XK
DEL=PHI(J)*DSO(J)*CMPLX(COS(RS),SIN(RS))
IF (ZS(J).NE.0.0) DEL=DEL/ZS(J)
75 SUM=SUM+DEL
SCAT=20.0*ALOG10(CABS(SUM))+9.943
80 WRITE (6,900) THE,SCAT
90 CONTINUE
GO TO 10
100 FORMAT (18A4)
150 FORMAT (1H1,18A4)
200 FORMAT (2I5,5F10.5)
300 FORMAT (10H0SEG NUM,11X,24HENDPOINTS OF THE SEGMENT,11X,
&35HSEGMENT PARAMETERS THE CONSTANTS/11H NUM CELLS,6X,2HXA,8X,
&2HYA,8X,2HXB,8X,2HYB,6X,36HANGLE RADIUS LENGTH IZA IZB ZEX/)
400 FORMAT (/39X,14HKEY PARAMETERS//24X,23HNUMBER OF SEGMENTS USED,
&I21//24X,34HTOTAL NUMBER OF POINTS ON THE BODY,I10//24X,
&35HNUMBER OF INCIDENT FIELD DIRECTIONS,I9//24X,10HNUMBER OF ,
&19HBISTATIC DIRECTIONS,I15//24X,10HWAVELENGTH,F34.5)
500 FORMAT (11H0 I SEG,3X,4HX(I),6X,4HY(I),6X,4HS(I),6X,6HDSO(I),
&4X,5HZS(I)/)
600 FORMAT (1H1,25X,20HCURRENT DISTRIBUTION/18X,18HFOR INCIDENT FIELD,
&11H DIRECTION=,F7.2//22X,20HCURRENT DISTRIBUTION,5X,8HINCIDENT,
&6H FIELD/11X,7HI SEG,7X,3HAMP,6X,5HPHASE,8X,3HAMP,6X,5HPHASE/)
700 FORMAT (I12,I5,2(F13.5,F9.1))
800 FORMAT (1H1,19X,33HBISTATIC SCATTERING CROSS SECTION/18X,
&29HFOR INCIDENT FIELD DIRECTION=,F7.2//24X,
&24HTHETA 10*LOG(SIGMA*K0)/)
900 FORMAT (16X,2F13.2)
END

```



```

SUBROUTINE GEOM(LUMP,X,Y,S,DSQ,ZS,M,LL)
DIMENSION LUMP(100,2),X(100),Y(100),S(100),DSQ(100),ZS(100)
DATA REF /0.01745329/
I=0
L=0
10 READ (5,200) N,IMP,XA,YA,XB,YB,ANG,IZA,I7B,I7FX
ZΛ=0.00265252*IZA
ZB=0.00265252*I7B
ZFX=0.1*I7FX
IF (N.EQ.0) GO TO 75
ROT=SQRT((XB-XA)**2+(YB-YA)**2)
TREF=XB-XA
TRAY=YB-YA
IF (ANG.EQ.0.0) GO TO 20
TETA=0.5*REF*ANG
IF (ANG.EQ.180.0) GO TO 15
TREF=TREF+(YB-YA)/TAN(TETA)
TRAY=TRAY-(XB-XA)/TAN(TETA)
15 RADIUS=0.5*ROT/SIN(TETA)
ARC=2.0*RADIUS*TETA
ALF=TETA/N
DIDDLE=2.0*RADIUS*ALF
GO TO 25
20 RADIUS=999.999
ARC=ROT
DIDDLE=ROT/N
25 LIM=2*N-1
LAST=2
IF (YA.EQ.0.0.AND.YB.EQ.0.0.AND.ANG.EQ.0.0) LAST=1
DO 70 JIM=1, LAST
L=L+1
DO 60 J=1, LIM, 2
I=I+1
LUMP(I,1)=I
LUMP(I,2)=L
IF (I.EQ.100) WRITE (6,400)
IF (JIM.EQ.2) GO TO 55
IF (ANG.EQ.0.0) GO TO 30
SINA=SIN(J*ALF)
COSA=1.0-COS(J*ALF)
GO TO 35
30 SINA=0.0
COSA=FLOAT(J)/N
35 X(I)=XA+0.5*(TREF*COSA-TRAY*SINA)
Y(I)=YA+0.5*(TREF*SINA+TRAY*COSA)
S(I)=0.5*J*DIDDLE
IF (IMP) 40,45,50
40 CALL ZFUN(ZA,ZB,ZEX,S(I),ZS(I))
GO TO 60
45 ZS(I)=ZΛ+ZB*S(I)**ZFX
GO TO 60
50 ZS(I)=ZΛ+ZB*EXP(-ZEX*S(I))
GO TO 60
55 K=I-N
X(I)=X(K)
S(I)=S(K)
ZS(I)=ZS(K)
Y(I)=-Y(K)
60 DSQ(I)=DIDDLE
IF (2-JIM) 65,65,70

```

```
65  YA=-YA
    YB=-YB
70  WRITE (6,300) L,N,XA,YA,XB,YB,ANG,RADIUS,ARC,IZA,IZB,IZEX
    GO TO 10
75  M=I
    LL=L
200 FORMAT (2I5,5F10.5,3I4)
300 FORMAT (I3,I6,3X,4F10.5,F8.2,F8.3,F8.4,2I5,F6.1)
400 FORMAT (36HWARNING: WE'VE GENERATED 100 POINTS/)
    RETURN
    END
```

```

SUBROUTINE ZVOR (A,N,X,Y,IAT)
DIMENSION A(100,101),X(100),Y(100),L(100),M(100)
COMPLEX A,D, BIGA, HOLD,Y,X
INTEGER L,M
IF(IAT-1) 200,200,300
200 CONTINUE
D=CMPLX(1.0,0.0)
DO 80 K=1,N
L(K)=K
M(K)=K
BIGA=A(K,K)
DO 20 J=K,N
DO 20 I=K,N
10 IF (C ABS(BIGA)-C ABS(A(I,J))) 15,20,20
15 BIGA=A(I,J)
L(K)=I
M(K)=J
20 CONTINUE
J= L(K)
IF (J-K) 35,35,25
25 DO 30 I=1,N
HOLD=-A(K,I)
A(K,I)=A(J,I)
30 A(J,I)=HOLD
35 I=M(K)
IF (I-K) 45,45,38
38 DO 40 J=1,N
HOLD=-A(J,K)
A(J,K)=A(J,I)
40 A(J,I)=HOLD
45 IF (C ABS(BIGA)) 48,46,48
46 D=CMPLX(0.0,0.0)
RETURN
48 DO 55 I=1,N
IF (I-K) 50,55,50
50 A(I,K)=A(I,K)/(-BIGA)
55 CONTINUE
C REDUCE MATRIX
DO 65 I=1,N
DO 65 J=1,N
IF (I-K) 60,65,60
60 IF (J-K) 62,65,62
62 A(I,J)=A(I,K)*A(K,J) +A(I,J)
65 CONTINUE
C DIVIDE ROW BY PIVOT
DO 75 J=1,N
IF (J-K) 70,75,70
70 A(K,J)=A(K,J)/BIGA
75 CONTINUE
C PRODUCT OF PIVOTS
D=D*BIGA
A(K,K)=(1.000,0.000) /BIGA
80 CONTINUE
RN=N
DMAG=C ABS(D)*(2.**RN)
K=N
100 K=K-1
IF (K) 150,150,105
105 I=L(K)
IF (I-K) 120,120,108

```

```

108 DO 110 J=1,N
      HOLD=A(J,K)
      A(J,K)=-A(J,I)
110 A(J,I)=HOLD
120 J=M(K)
      IF (J-K) 100,100,125
125 DO 130 I=1,N
      HOLD=A(K,I)
      A(K,I)=-A(J,I)
130 A(J,I)=HOLD
      GO TO 100
150 CONTINUE
300 CONTINUE
      DO 210 I=1,N
      Y(I)=CMPLX(0.0,0.0)
      DO 210 J=1,N
210 Y(I)=A(I,J)*X(J)+Y(I)
      RETURN
      END

```

```

SUBROUTINE HANK(X,N,BJ,BY)
REAL NEW
IF (X.LE.0.0) GO TO 30
Z=0.25*X*X
SR=1.0
SI=0.0
H=SR
OLD=SR
K=1
10 NEW=-Z*OLD/FL0AT(K*K)
DEN=H*NEW
SR=SR+NEW
SI=SI+DEN
IF (ABS(DEN).LT.0.00001) GO TO 20
IF (K.GT.60) GO TO 20
K=K+1
H=H+1.0/FL0AT(K)
OLD=NEW
GO TO 10
20 BJ=SR
BY=0.6366198*(BJ*(0.5772157+ALOG(0.5*X))-SI)
RETURN
30 K=0
RETURN
END

```

```
SUBROUTINE ZFUN(ZA,ZB,ZEX,S,ZS)  
ZS=ZA+ZB+ZEX  
RETURN  
END
```

271 LINES P

Appendix C: Relation Between Two- and Three-dimensional Cross Sections

The relation between the scattering amplitudes of two- and three-dimensional bodies can be derived by assuming that the three-dimensional body is a finite segment, of length L , of the two-dimensional one. If the two-dimensional body is illuminated in a plane perpendicular to the generators with (say) an E-polarized plane wave, the far scattered field is

$$\underline{E}^s(\phi, \phi_0) \sim \sqrt{\frac{2}{\pi k \rho}} e^{ik\rho - i\pi/4} \underline{P}(\phi, \phi_0) ,$$

where \underline{P} is the two-dimensional far field amplitude, ϕ and ϕ_0 are polar angles giving the directions of scattered and incident field propagation, and ρ is the radial distance between the body and the far field point of observation. The scattering cross section per unit length $\sigma_2(\phi, \phi_0)$ is defined as

$$\sigma_2 = \lim_{\rho \rightarrow \infty} 2 \pi \rho \left| \frac{\underline{E}^s}{\underline{E}^i} \right|^2 ,$$

where \underline{E}^i is the incident field, implying

$$\sigma_2 = \frac{2\lambda}{\pi} \left| \underline{P} \right|^2 . \tag{C.1}$$

For a three-dimensional body

$$\underline{E}^s(\phi, \phi_0) \sim \frac{e^{ikr}}{r} \underline{S}(\phi, \phi_0) ,$$

where \underline{S} is the three-dimensional far field amplitude and the scattering cross section $\sigma_3(\phi, \phi_0)$ is defined as

$$\sigma_3 = \lim_{r \rightarrow \infty} 4\pi r^2 \left| \frac{\underline{E}^s}{\underline{E}^i} \right|^2,$$

implying

$$\sigma_3 = \frac{\lambda^2}{\pi} |\underline{S}|^2. \quad (C.2)$$

Now suppose that the three-dimensional body is a segment of the two-dimensional one, and that illumination is still in a plane perpendicular to the generators. Assume further that the point of observation remains in this plane and that the currents supported by the three-dimensional body are identical to those supported by the two-dimensional body.

The far scattered field is the sum of the surface currents,

$$\underline{E}^s = A \iint \underline{J}(\underline{r}') \frac{e^{ikR}}{R} ds' \quad (C.3)$$

where A is a constant and $R = |\underline{r} - \underline{r}'|$ is the distance between a surface point and the far field observation point. If the body is finite so that \underline{r} can be taken much greater than any and all body dimensions, then

$$\underline{E}^s \sim A \frac{e^{ikr}}{r} \iint \underline{J}(\underline{r}') e^{-ik\hat{r} \cdot \underline{r}'} ds',$$

implying

$$\underline{S} = kA \iint \underline{J}(\underline{r}') e^{-ik\hat{r} \cdot \underline{r}'} ds'.$$

Now if \underline{J} is independent of the axial variable z , the z -integration may be carried out immediately, whence

$$\underline{S} = kAL \int \underline{J}(\underline{\rho}') e^{-ik\hat{r} \cdot \underline{\rho}'} d\rho' \quad . \quad (C.4)$$

On the other hand, the z -integration can be carried out in equation (C.3), giving

$$\underline{E}^S = i\pi A \int \underline{J}(\underline{\rho}') H_0^{(1)}(k|\underline{r} - \underline{\rho}'|) d\rho' \sim i\pi A e^{ikr - i\pi/4} \sqrt{\frac{2}{\pi kr}} \underline{J}(\underline{\rho}') e^{-ik\hat{r} \cdot \underline{\rho}'} d\rho'.$$

Therefore

$$\underline{P} = i\pi A \int \underline{J}(\underline{\rho}') e^{-ik\hat{r} \cdot \underline{\rho}'} d\rho' \quad (C.5)$$

and a comparison of eqs. (C.4) and (C.5) shows that

$$\underline{S} = \frac{kL}{i\pi} \underline{P} \quad .$$

Thus the relation between two- and three-dimensional radar cross sections is

$$\sigma_3 = 2L^2 \sigma_2 / \lambda$$

or

$$\frac{\sigma_3}{\lambda^2} = 2 \left(\frac{L}{\lambda} \right)^2 \frac{\sigma_2}{\lambda} \quad . \quad (C.6)$$

REFERENCES

- Bowman, J. J. , T. B. A. Senior and P. L. E. Uslenghi (Eds.), Electromagnetic and Acoustic Scattering by Simple Shapes, North-Holland Publishing Company, Amsterdam (1969).
- Ducmanis, J. A. and V. V. Liepa, "Surface Field Components for a Perfectly Conducting Sphere", University of Michigan Radiation Laboratory Report No. 5548-3-T (1965).
- Knott, E. F. and T. B. A. Senior, "Non-Specular Radar Cross Section Study", Air Force Avionics Laboratory Technical Report AFAL-TR-73-2; University of Michigan Radiation Laboratory Report No. 011062-1-T (1973).
- Knott, E. F. , "Design and Operation of a Surface Field Measurement Facility", University of Michigan Radiation Laboratory Report 7030-7-T (1967).
- Rheinstein, J. , "Scattering of EM Waves from Dielectric Coated Conducting Spheres", IEEE Trans. AP-12 (1964), 334-340.
- Senior, T. B. A. and G. A. Desjardins, "Minimal Thickness Coatings", University of Michigan Radiation Laboratory Report No. 013630-11-T (1972).
- Stratton, J. A. , Electromagnetic Theory, McGraw-Hill Book Co. , Inc. , New York (1941).

DOCUMENT CONTROL DATA - R & D

(Security classification of title, body of abstract and indexing annotation must be entered when the overall report is classified)

1. ORIGINATING ACTIVITY (Corporate author) The University of Michigan Radiation Laboratory 2216 Space Research Bldg., North Campus Ann Arbor, Michigan 48105		2a. REPORT SECURITY CLASSIFICATION UNCLASSIFIED	
		2b. GROUP NA	
3. REPORT TITLE NON-SPECULAR RADAR CROSS SECTION STUDY			
4. DESCRIPTIVE NOTES (Type of report and inclusive dates) Technical Report, Scientific, Final			
5. AUTHOR(S) (First name, middle initial, last name) Eugene F. Knott, Valdis V. Liepa and Thomas B. A. Senior			
6. REPORT DATE February 1973	7a. TOTAL NO. OF PAGES 103	7b. NO. OF REFS 7	
8a. CONTRACT OR GRANT NO. F33615-72-C-1439	9a. ORIGINATOR'S REPORT NUMBER(S) 011062-1-F		
b. PROJECT NO. 7633	9b. OTHER REPORT NO(S) (Any other numbers that may be assigned this report) AFAL-TR-73-70		
c.			
d.			
10. DISTRIBUTION STATEMENT Distribution limited to U. S. Government Agencies only; Test and Evaluation Data; April 1973. Other requests for this document must be referred to AFAL/WRP.			
11. SUPPLEMENTARY NOTES		12. SPONSORING MILITARY ACTIVITY Air Force Avionics Laboratory Air Force Systems Command Wright-Patterson Air Force Base, Ohio	
13. ABSTRACT The research described in this document is directed toward the reduction of non-specular radar cross sections and the optimization of specific surface impedance treatments for shapes characterized by such scattering. The optimization is carried out by means of a computer program which digitally solves the surface field integral equations for an impedance boundary condition. The original program was furnished by the Air Force Avionics Laboratory and was later modified by the Radiation Laboratory in order to meet the specific requirements of the task. Salient results of the investigation show that maximum performance is obtained with maximum surface coverage and that performance is generally traded off for less extensive surface treatment. An impedance variation that increases linearly with increasing distance toward the rear of a body is preferable to any other, provided the rate of change at the commencement and termination of the loading is not too great. Because of the dual nature of the integral equations for E- and H-polarizations, the impedance in the vicinity of the edge itself is critical, since a favorable result for one polarization can be detrimental for the other. Because the specification of a desirable surface impedance variation does not necessarily lead directly to the specification of material properties, other studies were carried out to provide more information. A theoretical study of a coated sphere showed that if the coating meets certain specifications, the surface impedance can be predicted by means of a simple layer formula. Actual measurements of both surface fields and far scattered fields were performed and although some variance was noted, the data tend to confirm the dual nature of the E- and H-polarized integral equations.			

14.	KEY WORDS	LINK A		LINK B		LINK C	
		ROLE	WT	ROLE	WT	ROLE	WT
	GTD Edge diffraction Surface currents Surface impedance Surface sampling						

ORDER

GAMMA-1

GAMMA-2

1	0.2690180 00	-0.74240360 00	0.76934700 00	-0.74250630 00
2	0.7693320 00	-0.74243340 00	0.76937870 00	-0.74243370 00
3	0.7693940 00	-0.7424970 00	0.76950140 00	-0.74232450 00
4	0.7695010 00	-0.7425900 00	0.76914530 00	-0.74217820 00
5	0.76901760 00	-0.74354160 00	0.76970060 00	-0.74193430 00
6	0.7670080 00	-0.74333760 00	0.76916750 00	-0.74177210 00
7	0.76626420 00	-0.74439600 00	0.76754650 00	-0.74151080 00
8	0.76518330 00	-0.74431940 00	0.76683790 00	-0.74120950 00
9	0.76396560 00	-0.74550060 00	0.76604220 00	-0.74086710 00
10	0.76261060 00	-0.74514200 00	0.76515990 00	-0.74048230 00
11	0.76131780 00	-0.74689400 00	0.76413180 00	-0.74005400 00
12	0.75948640 00	-0.74750510 00	0.76313840 00	-0.73958050 00
13	0.75771580 00	-0.74840270 00	0.76200060 00	-0.73906040 00
14	0.75580530 00	-0.74926140 00	0.76077220 00	-0.73849190 00
15	0.75376430 00	-0.75016880 00	0.75947520 00	-0.73787330 00
16	0.75156130 00	-0.75112200 00	0.75803950 00	-0.73720260 00
17	0.74927750 00	-0.75211930 00	0.75662340 00	-0.73647780 00
18	0.74675040 00	-0.75315470 00	0.75507840 00	-0.73569670 00
19	0.74412380 00	-0.75423780 00	0.75345550 00	-0.73485730 00
20	0.74136520 00	-0.75533440 00	0.75175620 00	-0.73395710 00
21	0.73844580 00	-0.75644700 00	0.74998220 00	-0.73299380 00
22	0.73540110 00	-0.75763340 00	0.74813530 00	-0.73196490 00
23	0.73220040 00	-0.75881800 00	0.74621720 00	-0.73086780 00
24	0.72889370 00	-0.76002050 00	0.74423010 00	-0.72970000 00
25	0.72553600 00	-0.76123680 00	0.74217610 00	-0.72845990 00

THE IMPEDANCE OF THE SURFACE LAYER IS 0.27003520 00 0.79011960 00

S(D) IS 0.11614650 01

SIGMA(O)/N IS 0.0452035 , PHI IS -0.5958703 DEGREES

SIGMA(O)/N IS 152.2014753 , PHI IS 39.0078402 DEGREES

SIGMA(O)/N IS 152.2014753 , PHI IS 39.0078402 DEGREES

SIGMA(O)/N IS 152.2014753 , PHI IS 39.0078402 DEGREES

0.364240 00	0.152330-01	0.630010 00	-0.180610-01
0.596350 00	-0.510680-01	0.431560 00	0.585510-01
0.433880 00	0.954100-01	0.531110 00	-0.243630-01
0.483320 00	-0.117310 00	0.552190 00	0.816260-01
0.603460 00	0.644240-01	0.606250 00	0.133940-01
0.392640 00	0.752700-01	0.500370 00	-0.957450-01
0.460780 00	-0.140130 00	0.503360 00	-0.147140-01
0.673710 00	-0.504510-01	0.567420 00	0.107310 00
0.624340 00	0.152530 00	0.440930 00	0.141560 00
0.304040 00	0.352830 00	0.321300 00	0.130760 00
0.123320 00	0.368170 00	0.161510 00	0.509930-01
0.852320-01	0.668930-01	0.563050-01	0.116680-01
0.281550-01	0.160140-01	0.136840-01	-0.787830-03
0.668220-02	0.741670-02	0.393090-02	-0.850690-03
0.117640-02	0.236300-03	0.623250-03	-0.330130-03
0.173300-03	0.124440-04	0.843510-04	-0.417000-04
0.204000-04	-0.713920-04	0.072310-05	-0.532540-05
0.210320-05	-0.270070-06	0.671790-06	-0.640430-06
0.147400-06	-0.397400-07	0.651280-07	-0.632410-07

0.145940-07	-0.424470-08	0.1600480-08	-0.553780-08
0.102270-08	-0.342600-08	0.457470-08	-0.457470-08
0.639180-10	-0.272940-10	0.285250-10	-0.210420-10
0.250570-11	-0.176700-11	0.160020-11	-0.100130-11
0.184040-12	-0.102470-12	0.235940-12	-0.104800-12
0.840000-14	-0.600450-14	0.337610-14	-0.404750-14

19.985DEGREES

